RUN-AROUND MEMBRANE ENERGY EXCHANGER PROTOTYPE 4

DESIGN AND LABORATORY TESTING

A Thesis Submitted to the College of

Graduate Studies and Research

In Partial Fulfillment of the Requirements

For the Degree of Master of Science In the

Department of Mechanical Engineering

University of Saskatchewan

Saskatoon

By

DAVID ANTOINE BERIAULT

Permission to Use

In presenting this thesis in partial fulfillment of the requirements for a Postgraduate degree from the University of Saskatchewan, I agree that the Libraries of this University may make it freely available for inspection. I further agree that permission for copying of this thesis in any manner, in whole or in part, for scholarly purposes may be granted by the professor or professors who supervised my thesis work or, in their absence, by the Head of the Department or the Dean of the College in which my thesis work was done. It is understood that any copying or publication or use of this thesis or parts thereof for financial gain shall not be allowed without my written permission. It is also understood that due recognition shall be given to me and to the University of Saskatchewan in any scholarly use which may be made of any material in my thesis.

Requests for permission to copy or to make other use of material in this thesis in whole or part should be addressed to:

Head of the Department of Mechanical Engineering

University of Saskatchewan

Saskatoon, Saskatchewan, S7N 5A9

ABSTRACT

To maintain building air quality, fresh outdoor air is supplied to the space and stale indoor air is exhausted. By using an energy recovery system, heat and moisture can be transferred between the supply and exhaust airstreams to reduce the energy used to condition the supply air. The twin-tower enthalpy loop utilizes a liquid desiccant to transfer both heat and moisture between non-adjacent ducts in an open loop configuration. One problem with the open loop configuration is that the desiccant can become entrained in the airstreams and deposited on downstream mechanical equipment causing corrosion. The run-around membrane energy exchanger (RAMEE) is a novel design that utilizes a membrane to enclose the desiccant and prevent it from transferring to the air stream.

The membrane used in the previous RAMEE prototypes, Propore™, was discontinued. Therefore, replacement membrane alternatives were obtained and evaluated based on the vapour diffusion resistance (VDR), liquid penetration pressure (LPP), modulus of elasticity (E), and price. The VDR measurements were made using the Permatran-W® model 101k by Mocon and the LPP and modulus measurements were obtained using the bulge test apparatus. The AY Tech ePTFE laminate membrane was selected to replace Propore™. The measured VDR, LPP and modulus for the Ay Tech. membrane were 97±11 s/m, >82 kPa, and 387±32 MPa respectively, exceeding/meeting the values measured for Propore™ (158±18 s/m, >82 kPa, and 17±2 Mpa respectively).

RAMEE prototype 4 was constructed with a cross-counter flow configuration using the AY Tech membrane. Using the energy exchanger test facility, the effectiveness of prototype 4 was determined by measuring/controlling the supply and exhaust airstream temperatures, relative humidities, and flow rates. An electronic flow meter and an

electronically actuated flow control valve with a proportional controller were used to obtain the desired desiccant flow rate. Airstream temperatures were measured along the length of the exchangers and a drop then rise in temperature was observed when the latent transfer dominated the total energy transfer.

The highest total effectiveness values measured for prototype 4, at AHRI test conditions, were 52±16% and 47±7% for a net transfer unit (NTU) of 12.3 and a NTU of 5.0 respectively. The effectiveness trends obtained for prototype 4 fell between that observed for prototype 2 (Erb, 2007) and prototype 3 (Mahmud, 2009) due to the flow conditions of the prototypes. Furthermore, the effectiveness values measured for prototype 4 agreed well with a numerical model (Hemingson, 2005) for all desiccant flow rates after adding coiling coils to remove the heat gained by the desiccant from the pumps.

ACKNOWLEDGMENTS

The completion of this thesis and my masters program in general would not have been possible without the help and support of many people. Firstly, to my supervisors Dr. Carey Simonson and Bob Besant I am eternally grateful for your patience and understanding regarding the challenges I faced completing this program. Furthermore, to Dr. Simonson, Mr. Besant, Dr. Gazi Mahmud I am very appreciative for the wealth of knowledge made available to me by you and for all the technical but also interpersonal skills you have imparted. Furthermore, thanks to the student research team but in particular Howard Hemingson, Blake Erb, and Khazir Mahmud for all their help. It has been a pleasure working with all of you and I wish you all the best in your future endeavours.

A special thanks to my committee members Dr. David Torvi and Dr. Daniel Chen for their comments and suggestions which improved the quality of my work and thesis. I would also like to acknowledge the University of Saskatchewan, Department of Mechanical Engineering for their continued financial support throughout my masters program. Also, there are many University employees which assisted me in different ways. Thanks to the machine shop for all their help with the parts and materials for my project. Furthermore, thanks to Dave Deutscher, Rick Retzlaff, and Chris James for their assistance in instrumentation, controls, and data acquisition. Lastly, thanks to Venmar CES for the opportunity to work on a practical and challenging real world problem.

DEDICATION

This thesis is dedicated to my father Antoine Beriault, my step-mother Kelly Beriault, my brother Michael Beriault, sister Dawn Halbgewachs and late mother Leanne Cantin. Thank-you all for your continued love and support.

TABLE OF CONTENTS

LIST OF TABLES

LIST OF FIGURES

NOMENCLATURE

Acronyms

AATCC	American Association of Textile Chemists and Colorists
AHRI	Air-conditioning Heating and Refrigerating Institute
ANSI	American National Standards Institute
ASME	American Society of Mechanical Engineers
ASHRAE	American Society of Heating, Refrigerating and Air-Conditioning Engineers
ASTM	American Society for Testing and Materials
DMPC	Dynamic Moisture Permeation Cell
ePTFE	Expanded Polytetrafluoroethylene
EI	Exhaust Inlet
HDPE	High Density Polyethylene
HVAC	Heating, Ventilation and Air-Conditioning
HPLC	High Purity Low Concentration (water)
ISO	International Organization for Standardization
LAMEE	Liquid-to-Air Membrane Energy Exchanger
LPP	Liquid Penetration Pressure
LVDT	Linearly Variable Displacement Transducer
NSERC	Natural Science and Engineering Research Council
NTU	Number of Transfer Units
PP	Polypropylene
PTC	Performance Test Code
PID	Proportional, Integral, and Derivative (Controller)

RAMEE	Run-Around Membrane Energy Exchanger
RH	Relative Humidity
RAMEETA	Run-Around Membrane Energy Exchanger Test Apparatus
SCCM	Standard Cubic Centimetres per Minute
SI	Supply Inlet
TM	Trademark
US	United States (of America)
VDR	Vapour Diffusion Resistance
WVP	Water Vapour Permeability
WVTR	Water Vapour Transmission Rate

English Symbols

a	radius of the bulge test cell [28.5±0.1 mm]
A	area [m^2]
$\%A$	percent of the total area
B	bias error in a measurement
C	number of constants in the calibration curve (2 for linear)
C_{AIR}	heat capacity rate of the air [W/K]
C_{AVG}	average heat capacity rate [W/K]
C_d	orifice plate discharge coefficient [Approx. 0.61]
C_{DES}	heat capacity rate of the desiccant [W/K],
C_{in}	inlet heat capacity rate [W/K]
Cn,sol	desiccant water solution concentration [kg_{DES}/kg_W]
C_{out}	outlet heat capacity rate [W/K]

$(c_P)_A$	specific heat of the air [J/kgK]
$(c_P)_D$	specific heat of the desiccant [J/kgK]
Cr*	ratio of the desiccant to air heat capacity rates
C_{SALT}	salt concentration of the desiccant [wt%],
$(c_2)_{CAL}$	calibration outlet nitrogen vapour concentration [kg/m^3]
Cx	constant X used to calculated the air vapour pressure
d	ratio orifice diameter to the pipe diameter
D_1	pipe diameter [0.0508±0.0001 m]
D_2	orifice plate diameter [0.038 m ± 0.0001 m]
E	modulus of elasticity [MPa]
h	membrane deflections [mm]
H	enthalpy [J/kg]
k_m	water vapour permeability [kg/(ms)]
$\dot{m}$	mass flow rate [kg/s]
$\dot{m}_{avg}$	average mass flow rate [kg/s]
$\dot{m}_D$	desiccant mass flow rate [kg/s]
$\dot{m}_i$	inlet mass flow rate [kg/s]
$\dot{m}_o$	outlet mass flow rate [kg/s]
$\dot{m}''$	water vapour transmission rate (WVTR) per unit area of membrane [kg/m^{2}s]
$\dot{m}''_{CAL}$	calibration WVTR per unit area [g/m^{2}day]
$\dot{m}''_M$	theoretical membrane WVTR per unit area [g/m^{2}day]

$\dot{m}''_{TOT}$	total WVTR per unit area [g/m^{2}day]
M_W	molecular weight of water [18.02 kg/kmol]
N	number of measurements or samples tested
P	pressure [Pa]
P_{atm}	atmospheric pressure [101.3kPa]
P_{BF}	best fit precision uncertainty in the calibrated measurement
P_V	partial pressure of water vapour in air or nitrogen [Pa]
$P_{V,SAT}$	saturation partial pressure or water vapor in air or nitrogen [Pa]
q	air flow rate [m^3/s]
Q	volume flow rate of nitrogen at the test temperature [m^3/s]
Q_S	volume flow rate of nitrogen at the standard temp. (0°C) [m^3/s]
R	universal gas constant [8314 J/(K kmol)]
Rbl_1	boundary layer resistance for area 1 [s/m]
Rbl_2	boundary layer resistance for area 2 [s/m]
R_{CAL}	calibration vapour diffusion resistance [s/m]
R_M	membrane vapour diffusion resistance [s/m]
Rm_O	observed membrane vapour diffusion resistance [s/m]
R_T	total vapour diffusion resistance [s/m]
S	precision error in a measurement
SEE	standard error of estimate introduced by using a best fit
t	t-student distribution value at N-1 degrees of freedom

T	temperature [K]
T_{DES}	temperature of the desiccant [°C]
U_X	uncertainty in quantity X
U_{95}	95% confidence interval measurement uncertainty
V_f	velocity of the airstream at the inlet (face) of the exchangers
$\dot{V}_N$	standard volume flow rate of nitrogen [cm^3/day]
W	humidity ratio of air [g_W/kg_{DA}]
$y_{BF,K}$	value obtained using the best fit equation at the calibration point k
$y_{RS,K}$	reference standard measurement at calibration point k

Greek Symbols

ΔC_a	vapour concentration difference between the reservoir and the nitrogen stream at the inlet of the test cell [kg/m^3]
ΔC_b	vapour concentration difference between the reservoir and the nitrogen stream at the outlet of the test cell [kg/m^3]
$\Delta\overline{C}$	log mean concentration gradient of vapour across a membrane [kg/m^3].
ΔP	pressure drop measured across the orifice [in. H_2O]
$\Delta\dot{m}''$	difference between the inlet and outlet mass flow rate [kg/s]
Δz	membrane thickness [m]
$\Delta\varepsilon_l$	difference in the latent effectiveness on the supply and exhaust sides of the exchanger
$\Delta\varepsilon_s$	difference in the sensible effectiveness on the supply and exhaust sides of the heat exchanger
$\Delta\varepsilon_t$	difference in the total effectiveness on the supply and exhaust sides of the exchanger

ε_{avg}	average of the supply and exhaust effectiveness values
ε_S	supply air-stream effectiveness value
ε_E	exhaust air-stream effectiveness value
ε_θ	θ component of the membrane strains [mm/mm]
ρ	density [kg/m^3]
ρ_{DA}	density of dry air [kg/m^3]
ρ_S	standard nitrogen density [$1.2922 \times 10^{-3} g/cm^3$]
σ	tensile stress induced on the membrane in the θ-r plane [Pa]

CHAPTER 1

INTRODUCTION

To reduce occupant illnesses known as “sick building syndrome” and “building-related illness” (ASHRAE, 2005) and caused by poor indoor air quality, it is necessary to supply building occupants with fresh outdoor air and exhaust the stale and/or contaminated indoor air. However, typically the conditions (temperature and relative humidity) of the outdoor air are such that supplying them directly to the space would be detrimental to the comfort, productivity, and satisfaction of the occupants. Therefore, it is necessary to alter the conditions of the outdoor air prior to supplying it to the space.

During summer conditions, the outdoor air is often too hot and humid to supply directly to the space so it must be cooled and dehumidified. Similarly, during winter conditions the outdoor air is often too cold and dry and must be heated and humidified prior to being supplied to the space. Heating, cooling, humidifying, and dehumidifying (all referred to as conditioning) the outdoor supply air requires the use of energy. The purpose of a recovery system is to reduce the auxiliary energy required to condition the fresh outdoor air supplied to the space. Therefore, the addition of a heat/energy recovery system can reduce building energy consumption.

1.1 Heat and Energy Recovery Systems

Heat/energy recovery systems reduce building energy consumption by passing the indoor air, which is exhausted from the space (exhaust air), and the outdoor air, which is being supplied to the space (supply air), through a heat/energy recovery system. After

passing through the recovery system, the conditions of the supply air are brought closer to the desired conditions, reducing the amount of heat and/or moisture to be added or removed from the air. Heat exchangers can only transfer sensible heat between the supply and exhaust air streams. Sensible transfer is driven by the temperature difference (potential) between the air streams. Energy exchangers are capable of both sensible heat transfer and latent transfers. The latent heat transfer is proportional to the vapour pressure gradient between the air streams. Combining the sensible and latent transfers yields the total energy transfer driven by the enthalpy difference between the air streams. Four types of heat/energy recovery systems are presented in Figure 1.1. The differences between these systems and the previous research pertaining to them are presented in the sections to follow.

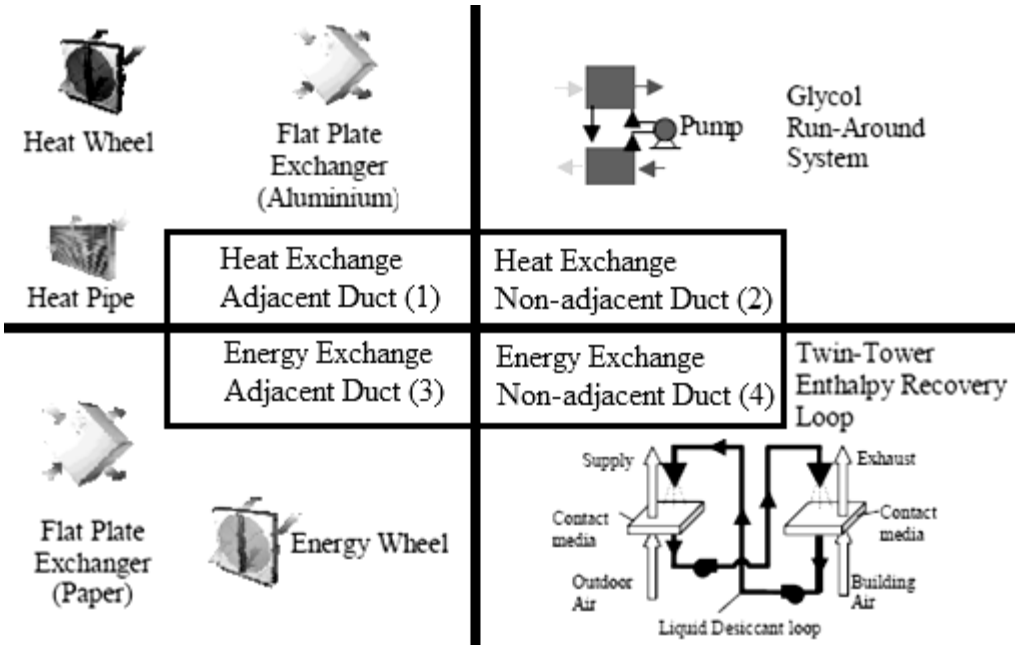

Figure 1.1. The four major types of recovery systems currently used to reduce building ventilation air conditioning costs with quadrants 1 and 3 being systems that require adjacent ducts and quadrants 3 and 4 being systems which have both latent and sensible heat transfer capabilities (Larson, 2006).

1.1.1 Recovery Systems Performance

An important parameter used to quantify the performance of an energy recovery system is effectiveness. The three types of effectiveness are sensible, latent, and total. for heat exchangers, effectiveness is the ratio of the heat that is recovered divided by the total transfer potential. The sensible effectiveness is dependent on temperature differences, the latent effectiveness is dependent on moisture differences, and the total effectiveness is dependent on enthalpy differences. If the supply and exhaust mass flow rates are equal, the supply effectiveness is calculated using equation (1.1) and the exhaust effectiveness is calculated using equation (1.2) (ASHRAE Std. 84, 1991). If there are no heat gains or losses, and the system is operating at steady state, the supply effectiveness should equal the exhaust effectiveness. Note: the subscripts in and out of equations (1.1) and (1.2) refer to the inlets and outlets of the air streams respectively.

$$\varepsilon_S = \frac{\left(X_{in,S} - X_{Out,S}\right)}{\left(X_{in,S} - X_{in,E}\right)} \tag{1.1}$$

$$\varepsilon_E = \frac{\left(X_{in,E} - X_{Out,E}\right)}{\left(X_{in,S} - X_{in,E}\right)} \tag{1.2}$$

where, ε_S = the supply air-stream effectiveness of interest,

ε_E = the exhaust air-stream effectiveness of interest,

X = T, temperature for sensible effectiveness [K],

= W, humidity ratio for latent effectiveness [kg_W/kg_{DA}],

= h, enthalpy for total effectiveness [J/kg].

1.1.2 Air-to-air Heat Recovery Systems

Air-to-air recovery systems include heat wheels, heat pipes, and flat plate heat exchangers (shown in quadrant 1, Figure 1.1). These systems are relatively inexpensive to

construct and operate and are used extensively in industry. Due to the extensive use of these systems in HVAC industry, much is known about their operation and a certification standard (AHRI 1060, 2005) has been developed, by the HVAC equipment manufacturers, for measuring the effectiveness. Many numerical models have been developed to accurately predict the effectiveness, outlet conditions, and other parameters of these recovery systems and in the sections to follow a select few of these models are discussed.

Heat wheels are constructed of non-porous corrugated materials or a packed bed of aggregate material, such as aluminum or stainless steel, capable of storing only thermal energy (sensible). The wheel rotates between the air-streams warming in one and cooling in the other thus transferring heat. Wu et al. (2006) numerically modeled a heat wheel system with attention to the temperature distributions in the air-streams and wheel metal matrix. The findings of the model were used to determine the optimal rotation speed. Skiepko and Shah (2004) compared a model similar to that developed by Wu et al. (2006) to experimental measurements of a 1.5 m (5 ft.) diameter heat wheel installed in a field application. The field exchanger effectiveness was found to agree, within experimental uncertainty, with that predicted by the numerical model.

Unlike heat wheels, heat pipe exchangers do not have any mechanical motion between the ducts. Heat pipe exchangers are constructed of many self contained pipes filled with a refrigerant. By natural convection the refrigerant circulates within these pipes transferring heat between the air streams. By virtue of this construction, these exchangers create large spatial temperature distributions within the air-streams. Johnson et al (1998) conducted in-situ testing of a heat pipe exchanger to determine the effectiveness of the

system. An emphasis of this work was quantifying the uncertainty in the measurements caused by the spatial temperature distributions.

Although air-to-air heat recovery systems are typically inexpensive, reliable, and capable of high sensible heat recovery, they also have their shortcomings. These systems require adjacent exhaust and supply ducts and only have sensible heat transfer capabilities, limiting their total energy recovery capacity. Thus, systems that do not require adjacent duct geometry and that are capable of transferring both sensible and latent heat transfer would be ideal for retrofitting applications with non-adjacent ducting.

1.1.3 Run-around Heat Recovery Systems

Run-around heat recovery systems were developed to address the need for heat recovery in applications with non-adjacent supply and exhaust ducts (see quadrant 2, Figure 1.1). These systems are known as run-around liquid-to-air heat exchangers. One exchanger is placed in the exhaust air stream and another is placed in the supply air stream and they are coupled with a working fluid (typically aqueous glycol). The working fluid passes through one of the air-to-liquid exchanger coils gaining heat from that air-stream. The working fluid is then passed through the other air-to-liquid exchanger coil, rejecting heat to that air-stream. By repeating this loop heat from one air-stream is transferred to the other.

Johnson et al (1998) created a numerical model of a field run-around heat exchanger system with multiple coils in multiple ducts. The model calculated the system life cycle cost and determined critical design parameters. In addition, measurements of the multi-coil run-around system were made in the field confirming parameters predicted using the model. Run-around glycol systems have been utilized in retrofitting applications

with non-adjacent duct geometries, but they are limited to sensible energy transfer and do not capitalize on the latent energy recovery potential.

1.1.4 Air-to-air Energy Recovery Systems

Modifications to the construction of heat wheels were made to add latent heat transfer to the wheels' capabilities. These modifications included adding a desiccant coating to the corrugated metal cores capable of storing moisture. Another modification was to replace the aggregate metal cores with silica beads (a porous solid desiccant with high surface area capable of storing moisture). The result of these modifications was the enthalpy or energy wheel (shown in quadrant 3, Figure 1.1) which is capable of transferring both sensible and latent heat.

A silica bead core energy wheel was experimentally tested by Neti and Wolfe (2000). The focus of their work was to determine the effectiveness as a function of the rotating speed. Neti and Wolfe (2000) compared the experimental results to analytical results and found agreement only at certain operating conditions. Nia et al. (2006) numerically modeled an energy wheel similar to that investigated by Neti and Wolfe's (2000). Nia et al. (2006) developed correlations used to calculate the air outlet temperatures and relative humidities and obtained good agreement with published experimental results. Simonson et al. (1999) modeled and experimentally tested a desiccant coater energy wheel to determine effectiveness. They made recommendations regarding the experimental methods used to determine the effectiveness with reasonable uncertainties. Energy wheel exchangers demonstrate good energy recovery capabilities and are a relatively simple and inexpensive method for recovering both heat and moisture in buildings with adjacent supply and exhaust ducts.

Similar to energy wheels, flat plate energy exchangers (shown in quadrant 3, Figure 1.1) were the result of modifications to flat plate heat exchangers. The latent heat transfer capability was accomplished by replacing the non-porous metal plate air-stream separators of flat plate heat exchangers. The metal plate air-stream separators were replaced with vapour permeable membranes. These membranes have micron-sized tubes or pores which allow water vapour molecules to transfer from one air-stream to the other while maintaining flow separation.

A porous membrane flat plate energy exchanger was numerically modeled by Zhang and Jiang (1999) to predict the operating characteristics. The outlet conditions, predicted using their model, were confirmed experimentally. The energy wheel and flat plate energy exchangers showed increased energy recovery capabilities to the heat wheels and flat plate heat exchangers. However, air-to-air energy recovery systems cannot be used in applications with non-adjacent supply and exhaust ducts. Therefore, a run-around energy recovery system with both heat and moisture transfer capabilities was desired.

1.1.5 Run-around Energy Recovery Systems

The run-around energy recovery system (shown in quadrant 4, Figure 1.1) has one liquid-to-air energy exchanger in the supply duct and another in the exhaust duct. The energy exchangers are coupled using a working fluid capable of transferring heat and moisture between remotely located ducts. The twin tower enthalpy recovery loop is an example of a run-around energy recovery system with the added capabilities of fully conditioning the supply air to the desired conditions. The loop uses a liquid desiccant (salt solution) circulated between two tower exchangers one in each air-stream. The desiccant drips down through a packing material while air flows up through this packing material creating an open system configuration where the desiccant is in direct contact with the air

streams. Unfortunately, the open system configuration allows entrainment of the desiccant into the air-stream. Downstream from the tower exchanger the desiccant is deposited on mechanical equipment causing excessive corrosion.

The run-around membrane energy exchanger (RAMEE) system is a "closed system" similar to the twin tower enthalpy recovery loop. In the RAMEE the liquid desiccant is separated from direct contact with the air-streams using a porous membrane (similar to Gore-tex®). The porous membrane eliminates the potential for entrainment of the liquid desiccant into the air-streams. The pores of the membrane allow the three Angstrom water vapour molecules to pass through but, due to the surface tension of the liquid desiccant, retaining the liquid desiccant, provided the pressure does not exceed the break-through pressure for the membrane. The development of the RAMEE system is the focus of the NSERC/Venmar CES Collaborative Research and Development Project and the work presented in this thesis is a small piece of this undertaking.

1.2 The Run-Around Membrane Energy Exchanger

At the turn of the millennium Dr. Simonson and Prof. Besant began work with Venmar CES Inc. on developing a RAMEE for retrofitting applications. While researching this technology a patent filed in 2003, owned by Dave Thompson, for an "enthalpy pump" was discovered. The enthalpy pump was similar enough to the RAMEE to warrant the purchase of the patent by Venmar CES Inc. in 2006. A basic schematic the enthalpy pump is shown in Figure 1.2.

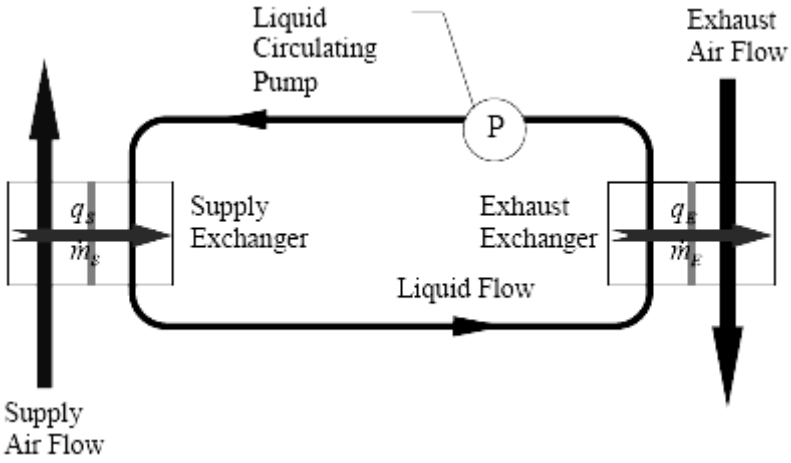

Figure 1.2. Schematic of the enthalpy pump patented by Dave Thompson (Fan, 2005).

Similar to the twin tower enthalpy exchanger system, the RAMEE system uses two energy exchangers, one in the supply duct and the other in the exhaust duct. Each exchanger is a liquid-to-air membrane energy exchanger (LAMEE) coupled together using a liquid desiccant (salt solution) as the working fluid. Therefore, to better understand the operation of the RAMEE, an understanding of liquid desiccants is required.

1.2.1 Liquid Desiccants

As with the twin tower enthalpy loop, the RAMEE utilizes a liquid desiccant (salt solution) as the working fluid. The liquid desiccant has the ability to alter the moisture content of air depending on the temperature and salt concentration of the desiccant and humidity ratio of the air. If the humidity ratio of the air is greater than the equilibrium humidity ratio of the desiccant (which changes with temperature and concentration as shown in Figure 1.3), the desiccant will dry the air. Similarly, if the humidity ratio of the air is lower than the equilibrium humidity ratio of the desiccant, the desiccant will humidify the air. Figure 1.3 is the psychrometric chart with lines of constant salt ($MgCl_2$) concentrations superimposed which indicate the equilibrium conditions for air in contact

with a $MgCl_2$ salt solution at the specified concentrations. Note that the lines of constant salt concentration are nearly parallel to the lines of constant relative humidity.

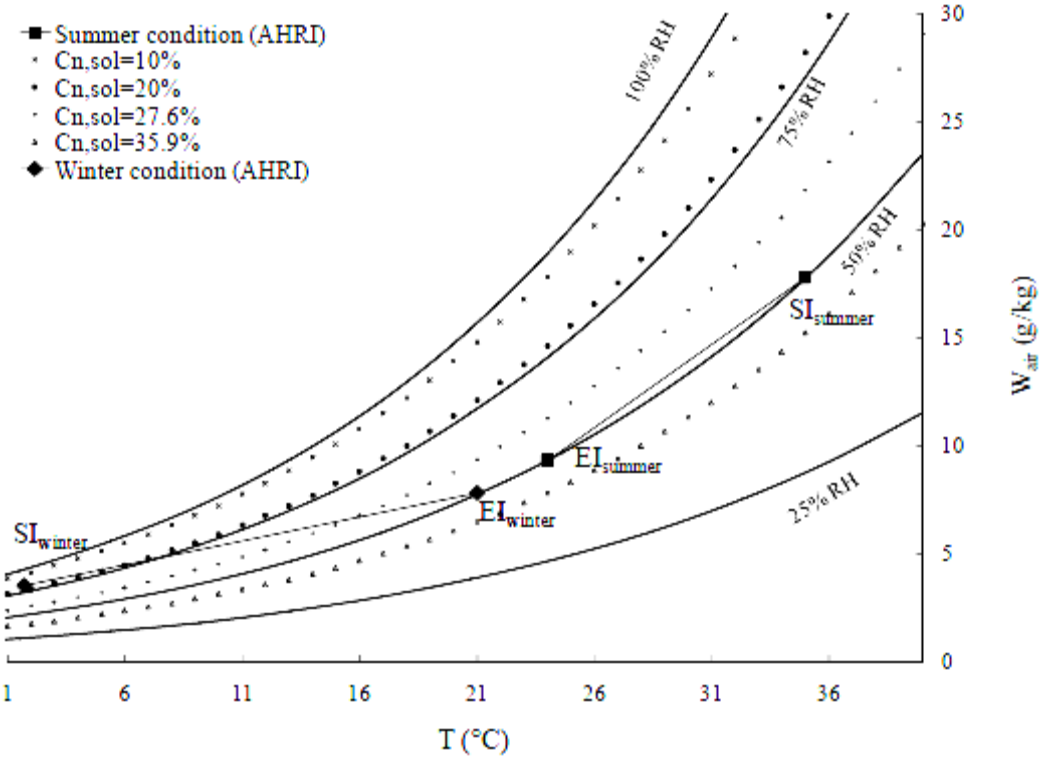

Figure 1.3. Equilibrium conditions for air in contact with $MgCl_2$ solutions with different salt concentrations superimposed on the psychrometric chart (Mahmud, 2009). Also shown are the standard (AHRI 1060, 2005) summer and winter supply inlet (SI) and exhaust inlet (EI) conditions.

1.2.2 RAMEE Numerical Model and Prototype 1

The initial goals of the research initiative were to evaluate the feasibility of the RAMEE system and make design changes to improve performance. The end goal of the research initiative is to produce a competitive run-around energy recovery system for non-adjacent duct retrofitting applications. Fan (2005) created a numerical model capable of predicting the temperature and water vapour distributions in cross flow LAMEE as shown in Figure 1.4. Fan's results showed promise in the use of the RAMEE system as a means

of energy recovery but predicted modest effectiveness' due to the flow configuration and size of exchanger simulated.

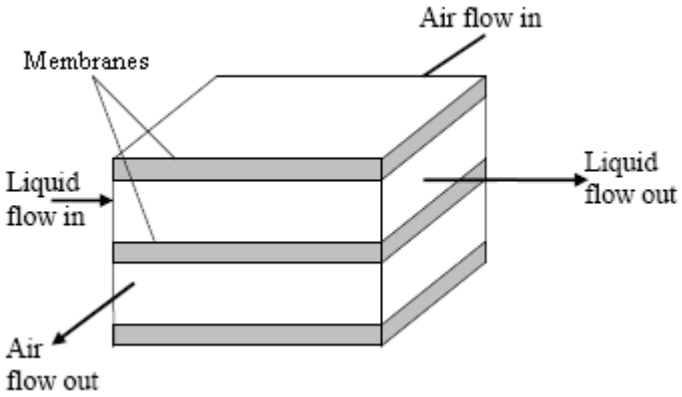

Figure 1.4. A portion of the LAMEE modeled by Fan to predict the RAMEE performance characteristics and investigate exchanger geometry (Fan, 2005).

The first RAMEE prototype designed and build at the university is shown in Figure 1.5 (Fan, 2005). This prototype used a cross-flow configuration with Japanese Tyvek® as the porous membrane separating the desiccant from direct contact with the air-stream. However, upon testing, several problems with the exchangers' design and construction became evident.

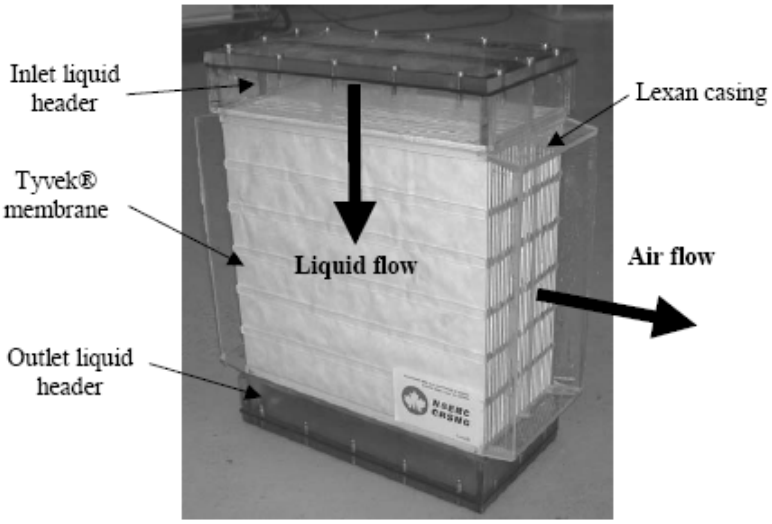

Figure 1.5. Photograph of RAMEE Prototype 1 built and tested by Hemingson (2005) (Larson, 2006). The exchangers were constructed directly adjacent as shown with a spacer in the headers.

One major problem observed with Prototype 1 was that the liquid desiccant would leak through the Tyvek® into the air streams. Another problem, encountered operating at higher pressures, was that the Tyvek® liquid channels deflected into the air-stream, contacting adjacent panels, reducing the transfer area, and reducing the effectiveness. During testing, the operating pressure was limited to reduce these problems, which introduced new complications. For example, operating at reduced pressures limited the desiccant flow rate and may have caused flow distribution problems.

Based on the complications with RAMEE Prototype 1, a membrane that would note leak at low pressures was needed and more attention to the membrane mechanical properties was required. Larson (2006) sourced a membrane called Propore™ produced by 3M™ Company based on the material cost, liquid penetration pressure, modulus of elasticity, and vapour diffusion resistance. The new membrane had a much higher liquid penetration pressure but a relatively low modulus of elasticity. To overcome the low elasticity of the Propore™ membrane, Larson recommended the addition of a metal screen to provide mechanical support on the air side of the membrane. The screen would reduce large bulk deflections of the membrane into the air streams but local deflections into the screen voids would still occur at the designed operating pressure.

1.2.3 RAMEE Prototype 2

Larson's recommendations were implemented into the design of the RAMEE prototype 2, constructed and tested by Erb (2007). A section view of the panels in prototype 2 is shown in Figure 1.6. Each exchanger in prototype 2 had ten panels in a cross flow configuration. The major differences between prototype 2 and prototype 1 was the addition of the outer screen, the use of Propore™ instead of Tyvek®, and the physical dimensions of the exchangers.

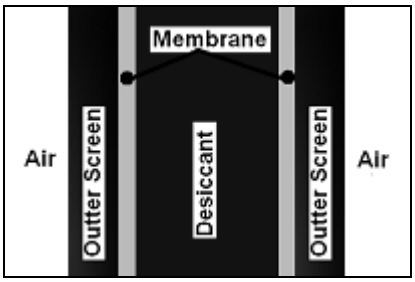

Figure 1.6. Section view of a single panel used to construct RAMEE Prototype 2. The desiccant flows between the membranes, the outer screen provides support to the membranes, and the air-stream flows on the outside of the outer screen.

Prototype 2 overcame the pressurization issues of Prototype 1, but it presented new challenges. Prototype 2 had a plastic inner screen material between the membranes in the desiccant flow channel. The intent of the inner screen was to ensure a uniform flow through the entire length of the panels and to allow the desiccant to enter and exit each panel without introducing an excessive flow restriction. However, the inner screen did restrict the desiccant flow into the panels, possibly introducing flow mal-distributions problems. To overcome the flow distribution problem, the system was operated at high pressures and the desiccant flow direction was reversed so that the flow direction would be from the bottom to the top of the exchangers. Erb (2007) also recommended the construction of an apparatus capable of pressurizing the individual panels. With this apparatus, sources of leakage (such as around the perimeter of the envelopes) could be identified and fixed prior to installing them into the exchangers.

The effectiveness observed for prototype 2 was significantly lower than that predicted by Fan (2005). Erb (2007) postulated that the flow mal-distribution caused a reduction in the experimentally observed effectiveness. However, Ahmadi (2008) and Erb (2009) were able to attain good agreement between the experimental effectiveness

values and the numerical model effectiveness values by accounting for the time delay for the system to reach steady state and heat gains/losses with the surroundings.

1.2.4 RAMEE Prototype 3 and Prototype 4

To increase the effectiveness of the RAMEE Prototype 2 a counter-flow configuration was considered. However, building a purely counter-flow RAMEE seemed impractical, so a "cross-counter flow" configuration was used in the construction of prototype 3. A schematic showing a typical flow path through these new counter-cross flow panels is shown in Figure 1.7. Prototype 3 was designed by Mahmud (2009) to achieve a total effectiveness of 65% when operated at AHRI test conditions with an airflow face speed of 2.03 m/s (400 ft/min).

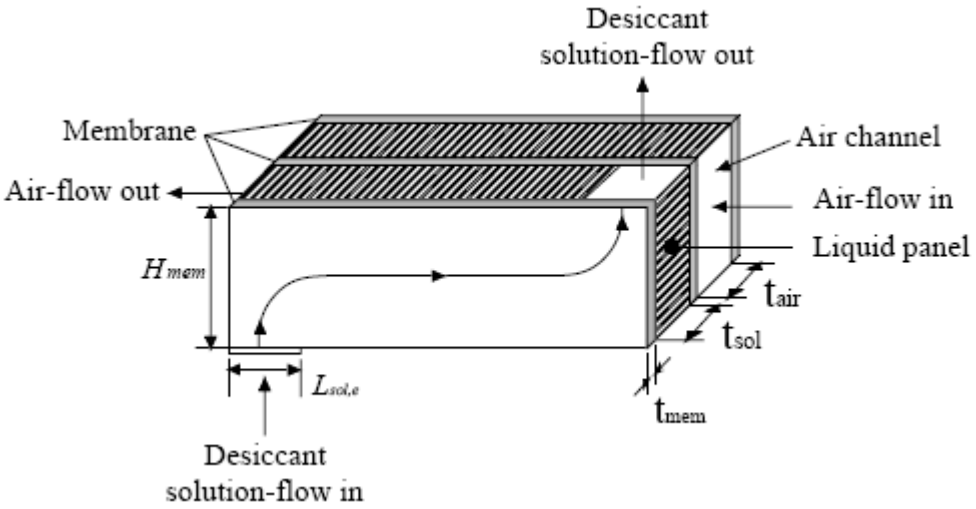

Figure 1.7. Schematic of the quasi counter-flow panels used to construct the prototype 3 RAMEE system (Mahmud, 2009).

The original intent of this thesis program was to design and construct a RAMEE similar to Prototype 3 but sized for a field installation. Before the construction of the field exchangers could begin more Propore™ was required. Upon contacting 3M™ Company it was found that the product Propore™ had been discontinued so there was a need for

sourcing a replacement membrane an using it in the new design. Due to the time delay caused by sourcing a replacement membrane and the risks associated with installing this new membrane in a field exchanger, it was decided that the exchangers would no longer be installed in a field application. Rather, a scaled down version of the field exchanger would be constructed and tested in the laboratory once a replacement membrane had been found. Similar to Larson, a replacement membrane would be selected based on measurements of the pertinent properties (i.e. the modulus of elasticity, vapour diffusion resistance, and liquid penetration pressure).

1.2.5 Membrane Alternatives

To find a suitable replacement for Propore™, many membrane alternatives are considered. Although Larson had previously determined that the Tyvek® Homewrap by DuPont™ was not a suitable membrane for use in the RAMEE, Tyvek® membranes were measured for comparison. Furthermore, Tyvek® 1059B and 1025B were used by Thompson in the construction of his field "enthalpy pumps", so the properties of these membranes were of interest to the numerical modelers Vali (2009) and Ahmadi (2008). A list of the membranes tested with the manufacturer specified polymer, cost, pore size, and percent porosity is given in Table 1.1. Some membranes are bonded to a support sub-straight but only the actual membrane polymer is listed in Table 1.1. The pore size is the average diameter of the micron-sized holes through which water vapour molecules diffuse thus transferring moisture. Porosity is defined as the volume fraction of interstitial voids (or lack of material) per unit volume of material.

Table 1.1. List of the porous membranes testes with manufacturer specifications.

	Membrane Polymer	Cost (US/ft^2)	Pore Size (μm)	Porosity
Propore™	Polypropylene	$ 0.10	<1	N/A
Tredegar VCL-510	Polypropylene	N/A	N/A	N/A
Tredegar #2	Polypropylene	N/A	N/A	N/A
Aptra™ RKW	Polypropylene	$ 0.35	0.2	60%
Porex® PM6M	Polytetrafluoroethylene	$ 40.00	1-2	35%-45%
Porex® PM3V	Polytetrafluoroethylene	$ 40.00	5	40%
Porex® X-7744	Polypropylene	$ 5.00	7	35%-45%
Porex® X-4904	Polypropylene	$ 5.00	2	35%-45%
Japanese Tyvek®	High Density Polyethylene	$ 0.15	2-15	45%
Tyvek® 1025B	High Density Polyethylene	$ 0.15	2-15	45%
Tyvek® 1059B	High Density Polyethylene	$ 0.15	2-15	45%
AY Tech Laminant	Polytetrafluoroethylene	$ 3.27	0.3	85%

1.3 Research Objectives and Thesis Overview

The objective of this thesis was to source a replacement porous membrane material and construct RAMEE Prototype 4 for laboratory evaluation. To accomplish this objective the following tasks must be accomplished:

- Measure the thickness, liquid penetration pressure, membrane vapour diffusion resistance, and modulus of elasticity for each membrane alternative in Table 1.1.
- Select a replacement membrane based on the membrane measurements combined with the cost information in Table 1.1.
- Construct a test apparatus capable of leakage testing the panels of the RAMEE prior to installation in the exchangers.
- Construct a RAMEE similar to Prototype 3 using the replacement membrane and measure the systems' effectiveness in the laboratory.
- Compare the results to previous experimental results and numerical simulations.

In the chapters to follow the membrane vapour diffusion resistance (VDR) is defined and the apparatus used to measure the membranes VDR is detailed. These VDR results are placed into context by comparing to other test methods and published results. Also presented in this thesis is the method used to measure the membranes' modulus of elasticity and a comparison is made between these findings and previously published data. The results of membrane thickness measurements and liquid penetration pressure measurements are presented and compared to manufacturer specifications and published results. The test apparatus used to measure the effectiveness of the new laboratory RAMEE is presented and modifications made to the apparatus are noted. The effectiveness results of the RAMEE are placed into context with the previous prototypes and compared to the numerical simulations. Lastly, this thesis presents conclusions and recommendations based on the findings of the preceding work.

CHAPTER 2

MEMBRANE VAPOUR DIFFUSION RESISTANCE

The mass transfer capabilities of the RAMEE are accomplished through use of a porous membrane to separate the liquid desiccant from the air streams. The membrane has micron sized caverns which allow water molecules to diffuse from one side of the membrane to the other. The flow of water vapour through the membrane is quantified by a mass flux which is analogous to a heat flux. Similarly, vapour diffusion resistance (VDR) is analogous to thermal diffusion resistance. A temperature gradient creates the driving potential for heat transfer while a water vapour concentration gradient creates the driving potential for water vapour transfer. Therefore, the mass flux of water vapour through the porous membranes can be calculated using equation (2.1).

$$\dot{m}'' = \frac{\Delta \overline{C}}{R_V} \tag{2.1}$$

where, $\dot{m}''$ = the water vapour transmission rate (WVTR) per unit area of membrane [kg/m^{2}s],

R_V = the vapour diffusion resistance (VDR) [s/m],

$\Delta \overline{C}$ = the log mean vapour concentration gradient across the membrane [kg/m^3].

The Permatran-W® 101K test apparatus was used to measure the water vapour transmission rate (WVTR) through the membrane alternatives. In the sections to follow, the Permatran-W® test method is outlined and the results are presented. The VDR results

are compared to other test results and sources for discrepancies are discussed to form conclusions based on the VDR results.

2.1 Significance of Membrane Vapour Diffusion Resistance

In the RAMEE system, the total VDR consists of three contributions: the air side boundary layer, the membrane, and the liquid desiccant boundary layer. Fan (2005) modeled RAMEE prototype 2 at AHRI summer conditions to obtain the variations in effectiveness with membrane VDR. His model used two liquid-to-air membrane energy exchangers (LAMEE), that measured 0.3 m x 0.6 m x 0.1 m (12" x 24" x 4"), coupled with a $MgCl_2$ water solution as the desiccant. The results obtained with an airstream face velocity of 0.22 m/s (44 ft/min) are presented in Figure 2.1.

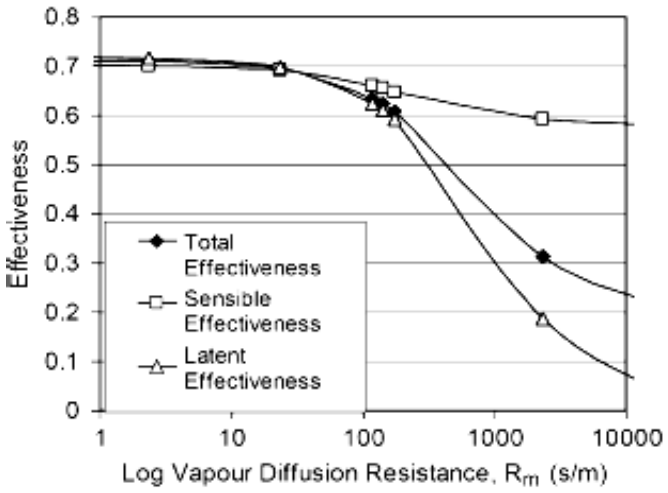

Figure 2.1. The dependence of the RAMEE sensible effectiveness, latent effectiveness, and total effectiveness to the membrane VDR (Larson et al. 2006).

As shown in Figure 2.1, Fan (2005) found that the effectiveness is sensitive to membrane VDR when the membrane VDR is higher than 20 s/m. Vali (2009) and Ahmadi (2008) also found that the membrane VDR was significant enough to dominate the total VDR within the RAMEE (Approx. 80%). Furthermore, the RAMEE systems

designed and tested by Erb (2007) (prototype 2) and Mahmud (2009) (prototype 3) were constructed using the Propore™ membrane. For both prototypes the overall system effectiveness was limited by the latent transfer capabilities. Larson (2006) measured the VDR of Propore™ to be 125 s/m which, as shown in Figure 2.1, is in the region where the effectiveness is sensitive to the membrane VDR. Therefore, an increase in the RAMEE effectiveness can be achieved by replacing the Propore™ membrane with a lower VDR membrane.

2.2 Water Vapour Transmission Measurement Methods

2.2.1 Standard Cup Test ASTM E 96

The water vapour transmission rate (WVTR) is a mass flux of water vapour through a porous material. Two methods commonly used to measure the WVTR are the wet cup test and dry cup test, as outlined in ASTM E 96 (2000). In the wet cup test, a cup is filled with water while in the dry cup test the cup is filled with a desiccant. For both tests the porous material is glued to the top of the cup and the cup is placed in a chamber maintained at 50% RH and 23°C. For the wet cup test, the water evaporates and is transferred through the porous material into the chamber. For the dry cup test, vapour is transferred from the chamber through the porous material and adsorbed by the desiccant. The mass of the cup is measured at standard time intervals until a constant mass transfer per unit time (g/day) is observed. By dividing the mass transfer by the transfer area, the WVTR is calculated (g/m^2day).

During both the wet and dry cup tests there is an air gap between the test material and the water or desiccant respectively. For relatively high VDR materials the air gap resistance is negligible but for low VDR materials, such as the porous membranes used in the RAMEE, the air gap resistance causes large uncertainties in the measurements. To

reduce the experimental uncertainty in low VDR materials measurements, the wet cup test was modified to the inverted cup test to eliminate the air gap.

2.2.2 The Inverted Cup Test ASTM E 96

In the inverted cup test method the top of the membrane is exposed to liquid water and the bottom side of the membrane is exposed to a 50% RH air-stream at 23°C. The test continues until a constant decrease in mass with time is observed indicating a steady state WVTR. The WVTR is converted to a vapour diffusion resistance (VDR) using equation (2.1). Some permeable materials have low liquid penetration pressures (LPP) and some are hygroscopic (adsorb liquid water). Water droplets can pass through low LPP materials under the static head pressure induced in the inverted cup test and the hygroscopic materials can transfer liquid water through surface diffusion. In either case water is not vapour diffusion is not the only mode of water transfer through the membrane causing a large bias in the observed WVTR used to calculated the VDR..

The modified inverted cup test uses an expanded polytetrafluoroethylene (PTFE) membrane (guard membrane) to ensure that the measured WVTR is from diffusion only. The PTFE membrane has a very low VDR and a high liquid penetration resistance to ensure that only water vapour contacts the test membrane. This test method is called the modified ASTM E96BW and is shown schematically in Figure 2.2 (a).

2.2.3 ISO 11092 Sweating Guarded Hot Plate Test

A method similar to the modified ASTM E9BW test is the ISO 11092 Measurement of Thermal and Water Vapour Resistance under Steady-State Conditions (Sweating Guarded hot Plate Test). In the ISO 11092 test a porous plate saturated with water is covered with a cellophane membrane similar to the PTFE membrane used in the modified ASTM E96BW test. The cellophane membrane prevents liquid water from

contacting the test sample but has a low enough VDR to allow water vapour to pass readily. The porous plate is maintained at 35°C by a resistive heater. As the water evaporated from the plate it requires the heat of phase change. Therefore, the power input into the heater is proportional to the WVTR. The test conditions and a schematic of the ISO 11092 test apparatus are shown in Figure 2.2 (b).

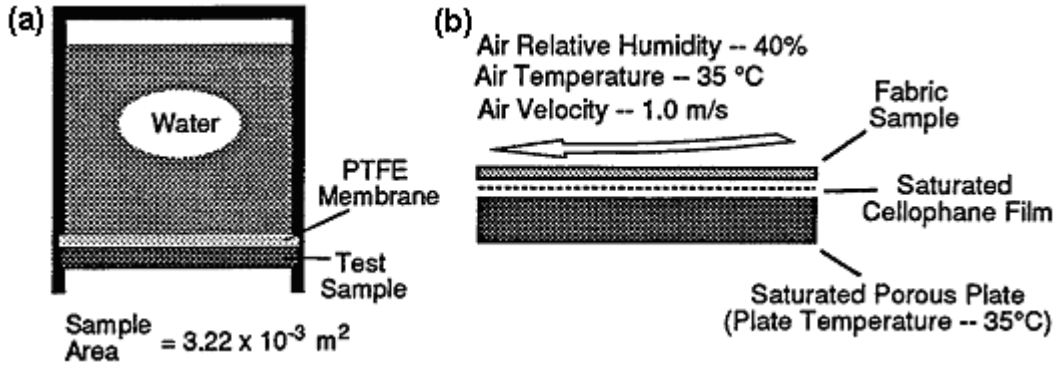

Figure 2.2. Schematic of (a) the modified ASTM E96BW with PTFE guard membrane and (b) ISO 11092 test appartus used for measuring the WVTR of porous membranes (Gibson, 2000).

2.2.4 The Dynamic Moisture Permeation Cell

Another method used to measure low VDR membranes is the dynamic moisture permeation cell (DMPC). In the DMPC both the top and bottom sides of the membrane are exposed to nitrogen streams. The nitrogen streams enter the test section with different vapour concentrations creating a gradient for vapour diffusion through the membrane. An exploded view of the DMPC is shown in Figure 2.3 with the chamber and sample dimensions. It should be noted that the nitrogen has sufficient entrance length to attain uniform fully developed flow and the chamber is wider than the sample ensuring that the side wall boundary layers do not impact the measurements.

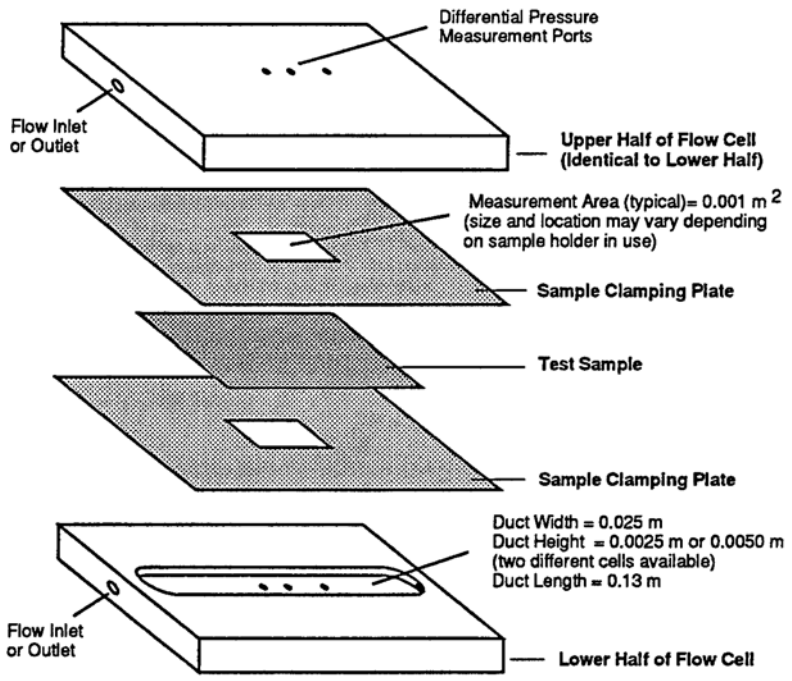

Figure 2.3. Dimensions and flow configuration of the DMPC used by Gibson to conduct Larson's measurements (Gibson, 2000).

The VDR measurements presented by Larson (2006), and Larson et al (2006,) were conducted by Gibson (2000) using the DMPC at the US Army Research, Development, and Engineering Center. Larson (2006) investigated the effect of moisture content within the membranes on the measured VDR. Figure 2.4 (a) presents the VDR measured (Larson, 2006) for Propore™ over a range of mean relative humidity's (RH) across the sample but at a fixed gradient of 50% RH. Figure 2.4 (b) presents the VDR measurements of Figure 2.4 (a) with two additional RH gradients (10% and 20%) induced across the Propore™.

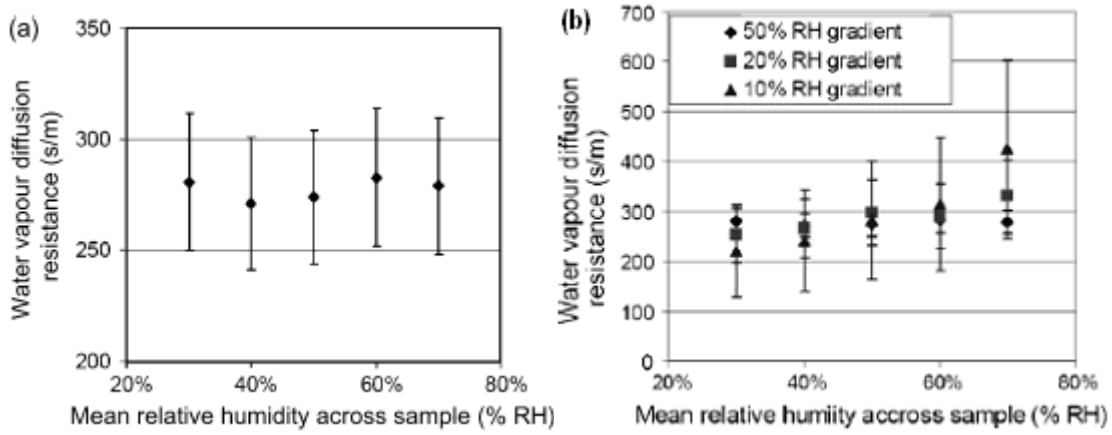

Figure 2.4. The VDR measurements for Propore™ for (a) variable mean relative humidity across the sample with a fixed gradient and (b) variable mean relative humidity across the sample with 10%, 20%, and 30% relative humidity gradients (Larson,2006).

As shown in Figure 2.4, Larson (2006) found that the VDR for Propore™ was insensitive to the RH gradient across the soecimen. Larson (2006) conducted similar test for Tyvek® and found that the VDR for Tyvek® was also insensitive to the RH gradient induced across the specimen. These membranes are non-hygroscopic materials so minimal water adsorption would have occurred. The mean relative humidity would likely have a greater effect on the transport properties of hygroscopic materials since they absorb water. The membrane alternatives presented in Table 1.1 are all non-hygroscopic membranes and as such should not be sensitive to the mean test RH.

2.3 Permatran-W® Model 101k Test Apparatus

The Permatran-W® Model 101k is an apparatus that was developed by Mocon based on the modified ASTM E96BW (inverted cup with a guard membrane) test procedure. However, there are two major differences between the Permatran-W® and the inverted cup with a guard membrane test methods. The first difference in these test

methods is the vapour concentration gradient used to drive vapour transfer through the test membrane. The second major difference is the method used to measure the WVTR.

The bottom side of the material being tested in the Permatran-W® is exposed to a dry (0% RH) high purity nitrogen stream while the modified inverted cup test method uses a 50% RH air stream. In the modified inverted cup test method the cup is mounted to a mass balance to measure the mass of water with time. In the Permatran-W® the mass flow rate and outlet RH of the nitrogen stream are measured to calculate the mass flow of water vapour through the membrane. To reduce the precision uncertainty of the Permatran-W® six different measurement areas are tested simultaneously. A schematic of a single test cell in the Permatran-W® is shown in Figure 2.5.

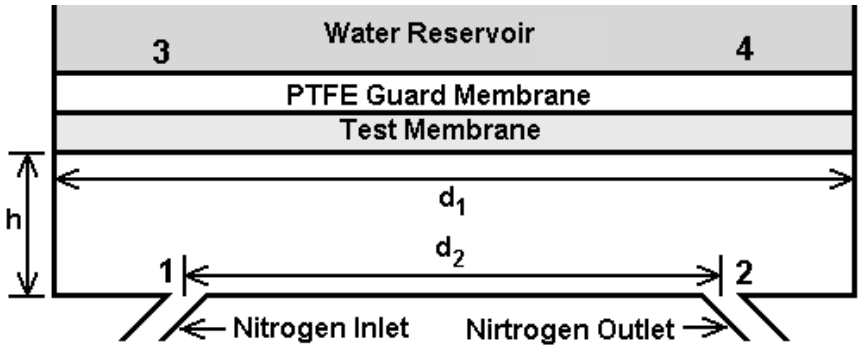

Figure 2.5. Schematic of each test cell in the Permatran-W® showing the locations at which the vapour concentration is needed to calculate the bulk mean concentration gradient. The dimensions of the nitrogen flow chamber were measured to be: h=3.10±0.02 mm, d_1=34.97±0.05 mm, and d_2=21.12±0.07 mm.

Before entering the test cells in the Permatran-W® the high purity nitrogen is passes through a desiccant chamber to ensure that the nitrogen is completely dry. The nitrogen then passes through a pressure regulator to reduce the nitrogen pressure to 103 kPa (15 Psi). The nitrogen stream is split to each of the six test cells and passed through valves used to balance the nitrogen flow through the test cells. Prior to venting to

atmosphere, one nitrogen stream is diverted to a CMOS semiconductor relative humidity sensor, through a dryer, and lastly through a mass flow meter for five minutes. The measurements observed at the five minute mark are used to determine the WVTR in that cell. The Permatran-W® measurement is compared to the previous measurement for that cell. If the WVTR agrees within the convergence criteria of 1%, the most recent WVTR is recorded for that cell and the cell is removed from the measurement cycle. This continues until all of the cells obtain steady WVTR measurements.

The Permatran-W® uses the relative humidity measurement, the test temperature, and the atmospheric pressure measurement, to calculate the nitrogen humidity ratio using equations (A.2), (A.3), and (A.4) (modified for nitrogen instead of air) of Appendix A. The dry nitrogen flow rate is measured using a volume flow meter with an output of standard cubic centimeters per minute (SCCM). Therefore, this volume flow rate is converted to a mass flow rate by multiplying by the density of the nitrogen at standard temperature (0°C) and 1 atmosphere pressure. Using the nitrogen flow rate and the humidity ratio, the WVTR is calculated using equation (2.2). The manufacturer specified uncertainty in the WVTR is ±10% and is used as the bias uncertainty.

$$\dot{m}'' = \frac{W}{A}\dot{V}_N \rho_S \tag{2.2}$$

where, $\dot{m}''$ = the measured WVTR [g_W/m^2day],

W = the outlet nitrogen humidity ratio [g_W/g_N],

$\dot{V}_N$ = the standard volume flow rate of nitrogen [cm^3/day],

ρ_S = the standard nitrogen density [$1.2922x10^{-3} g_N/ cm^3$],

A = the transfer area [0.001 m^2].

The WVTR measurements output by the Permatran-W® provide a relative comparison between the membrane alternatives. Unlike the VDR, the WVTR is dependent on the test conditions such as the nitrogen flow rate, flow condition, and relative humidity. Therefore, the VDR is a more suitable quantity for comparing results obtained using different test methods and conditions.

The Permatran- W® outputs the test temperature, the test membrane WVTR, the calibration WVTR (measured without a test membrane), the atmospheric pressure, the number of cycles to reach convergence, and the standard volume flow rate. However, none of the properties of the nitrogen streams are output, complicating the membrane VDR calculation. The method used to interpret the Permatran-W® results/measurements and calculate the test membrane VDR is outlined in Appendix B.

2.4 Water Vapour Permeability

In addition to the membrane VDR, the water vapour permeability is required for use in the computer models. Permeability is defined as "the measure of the flow conductance of the matrix" (Kaviany, 1995) where the matrix is the solid constituent in the media. Equation (2.3) was used (Larson, 2006) to calculate the water vapour permeability based on the membrane thickness and VDR measurements.

$$k_m = \frac{\Delta z \cdot M_W \cdot P_{atm}}{R_M \cdot R \cdot T \cdot 0.6219} \tag{2.3}$$

where, k_m = the water vapour permeability [kg/(ms)],

Δz = the membrane thickness [m],

M_W = the molecular weight of water [18.02 kg/kmol],

P_{atm} = atmospheric pressure [101.3kPa],

R = the universal gas constant [8314 J/(K kmol)],

T = the test temperature [296 K].

The thickness of the membranes was obtained using a 0.0001 mm precision micrometer. Twenty spatially distributed thickness measurements were made to obtain an average for each of the membranes. A bias uncertainty of 0.0002 mm was assumed to account for the slight compression of the membranes due to the clamping pressure of the micrometer.

2.5 Permatran-W® Results and Discussion

2.5.1 Results of the Permatran-W® Measurements

Using the Permatran-W® the WVTR through the membrane alternatives were measured. The Permatran-W® test temperature was set to 23°C and the same sample size (N=6) was used for all of the samples except for the Japanese Tyvek and Propore (N=12). The VDR, permeability, and average thickness obtained for each membrane alternative is presented in Table 2.1 and are denoted by a U with the subscript of the property which it quantifies. All uncertainties are given at a confidence interval of 95% in accordance with ANSI/ASME PTC 19.1 (1998). The bias uncertainty quoted by Mocon was 10% of the WVTR measurements and the precision uncertainty was obtained using the standard deviation of the N measurements as per ANSI/ASME PTC 19.1 (1998).

Table 2.1. Summary of the results obtained for the membrane alternatives including the vapour diffusion resistance, vapour permeability, and thickness.

	R_M (s/m)	U_{RM} (s/m)	k_m (kg/ms)	U_{km} (kg/ms)	Δz (mm)	$U_{\Delta z}$ (mm)
Propore™	301	34	8.88E-07	1.07E-07	0.22	0.009
Tredegar VCL-510	2080	271	2.22E-07	2.96E-08	0.39	0.011
Tredegar #2	11035	2034	4.02E-08	7.51E-09	0.37	0.012
Aptra™ RKW	733	74	7.20E-08	7.71E-09	0.04	0.002
Porex® PM6M	160	20	8.48E-07	1.06E-07	0.11	0.001
Porex® PM3V	109	12	1.71E-06	1.84E-07	0.16	0.001
Porex® X-7744	194	24	3.73E-06	4.61E-07	0.61	0.001
Porex® X-4904	76	8	4.14E-06	4.32E-07	0.26	0.002
Japanese Tyvek®	626	109	3.41E-07	6.37E-08	0.18	0.012
Tyvek® 1025B	466	175	3.75E-07	1.42E-07	0.15	0.008
Tyvek® 1059B	409	80	5.09E-07	1.10E-07	0.17	0.016
AY Tech ePTFE Lam	185	21	3.48E-06	4.03E-07	0.54	0.016

For the purpose of comparison, the membrane VDRs and WVP are presented in graphical form in Figures 2.6 and 2.7 respectively. It should be noted that Tredegar membranes are not shown in Figure 2.8 for the purpose of expanding the remaining data.

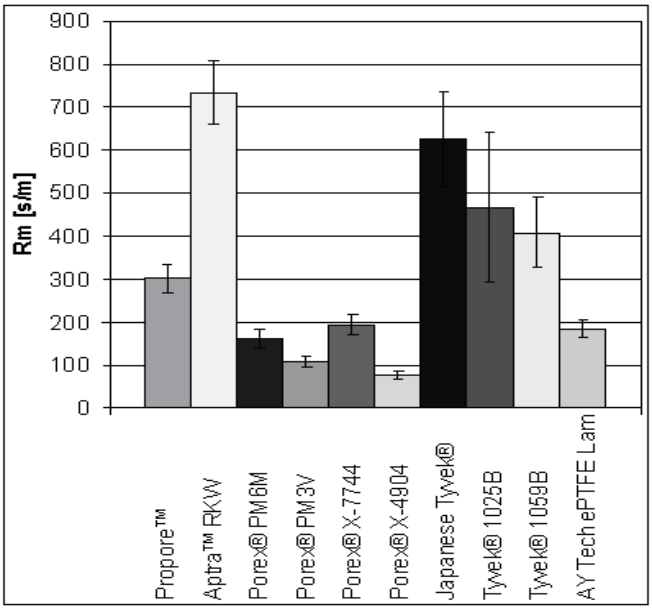

Figure 2.6. Average vapour diffusion resistances (VDRs) obtained using the WVTR measurements from the Permatran-W®.

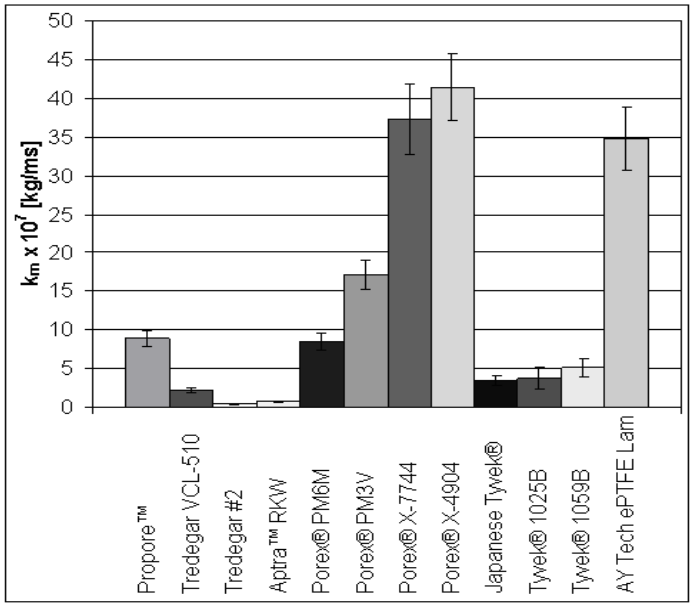

Figure 2.7. Average water vapour permeabilities (k_m) presented in Table 2.1 and obtained from the average VDRs and average thicknesses calculated using equation (2.19).

2.5.2 Discussion of the Permatran-W® VDR and WVP Results

It can be seen in Table 2.1 and Figure 2.6, that the Porex® and AY Tech. ePTFE Lam membranes measured VDR's were lower than Propore™. As shown in Figure 2.1, the latent effectiveness of a RAMEE constructed with Porex® or AY Tech. ePTFE Lam. membranes should exceed that of a RAMEE constructed with Propore™.

Porex® X-7744 and Porex® X-4904 have the same percent porosity with average pore size of 7 μm and 2 μm respectively (Table 1.1). Furthermore, the membrane thicknesses were measured to be 0.61 mm and 0.26 mm for the X-7744 and X-4904 respectively. As shown in Figure 2.6, the X-7744 had a VDR of 194 s/m, while the X-4904 had a VDR of 76 s/m. The manufacturer and percent porosity of these membranes are the same leaving pore size and thickness as the primary factors for the difference in VDR. However, as shown in Figure 2.7, the water vapour permeability of these membranes agrees within experimental uncertainty. The water vapour permeability is

normalized to a 1 m membrane thickness indicating the primary cause for the difference in the VDRs of these membranes is the thickness. Furthermore, the ratio of the X-7744/X-4904 VDRs is 2.6±0.4 and for thicknesses is 2.303±0.015 which agree within the uncertainty of the ratios. Therefore, the VDR would appear to be proportional to these membrane thicknesses and insensitive to the pore size.

As shown in Figure 2.6. the Porex® PM6M and Porex® PM3V membranes had VDRs of 160 s/m and 109 s/m respectively and do not agree within experimental uncertainty. Furthermore, the PM6M and PM3V WVPs (shown in Figure 2.7) also did not agree within experimental uncertainties. Therefore, unlike the Porex® X-7744 and X-4904, the difference in the measured VDR between the PM6M and PM3V is not due a difference in thickness. The only noted difference between the PM6M and PM3V was their pore sizes (1-2 μm and 5 μm respectively). However, the X-7744 and X-4904 had a larger difference in their pore sizes (7 μm and 2 μm respectively) and their WVPs agreed within experimental uncertainty. Therefore, more information regarding the manufacture of the PM3M and PM3V would be required to determine the cause of this discrepancy.

The Porex® X-7744 and the Porex® PM3V have very similar pore size (7 μm and 5 μm respectively) and percent porosity (35-45% and 40% respectively). Despite the similarities in these membranes, the X-7744 and PM3V WVPs did not agree within experimental uncertainty (Figure 2.7). Similarly, the Porex® X-4904 and the Porex® PM6M had similar pore size (2 μm and 1-2 μm respectively) and percent porosity (35-45% for both) but again their water vapour permeabilities did not agree within experimental uncertainty (Figure 2.7). However, the PM6M and PM3V membranes are constructed of polytetrafluoroethylene (PTFE) while the X-7744 and X-4904 membranes

are constructed of polypropylene (PP). Therefore, the difference in the observed water vapour permeabilities, presented in Figure 2.7, may be due to the molecular make up of the membranes.

Tyvek® 1025B and 1059B were found to have lower VDR's (466 s/m and 409 s/m respectively) than the Japanese Tyvek® (626 s/m) and almost agree within experimental uncertainty. The Tyvek® membranes have the same construction method, material, manufacturer, and percent porosity. However, unlike the Porex® X-7744 and X-4904, these membranes also have similar pore distributions. The 1025B and 1059B thicknesses, VDRs, and water vapour permeabilities all agree within experimental uncertainty (as seen in Table 2.1, Figure 2.6, and Figure 2.7). Therefore, the small difference in VDRs is likely due to the difference in the membrane thicknesses.

The Tredegar VCL-510 and Tredegar #2 membranes VDRs were found to be 2080 s/m and 11035 s/m respectively. The Tredegar thicknesses agreed within their uncertainty. Therefore, unlike the Porex® X-7744 and X-4904 and Tyvek® membranes, the large difference in the Tredegar membrane VDRs cannot be attributed to a difference in thickness. The manufacturer did not specify the percent porosity and pore size/distribution of the Tredegar membranes and there is likely a large difference in these properties causing the difference observed in the VDRs.

2.5.3 Comparison of the Different Test Methods

To validate the Permatran-W® measurements and data analysis, the results were compared to those obtained by Larson (2006). The VDRs of Propore™ and Japanese Tyvek® obtained using the Permatran-W® are compared to that obtained using the DMPC (Larson, 2006) in Figure 2.8.

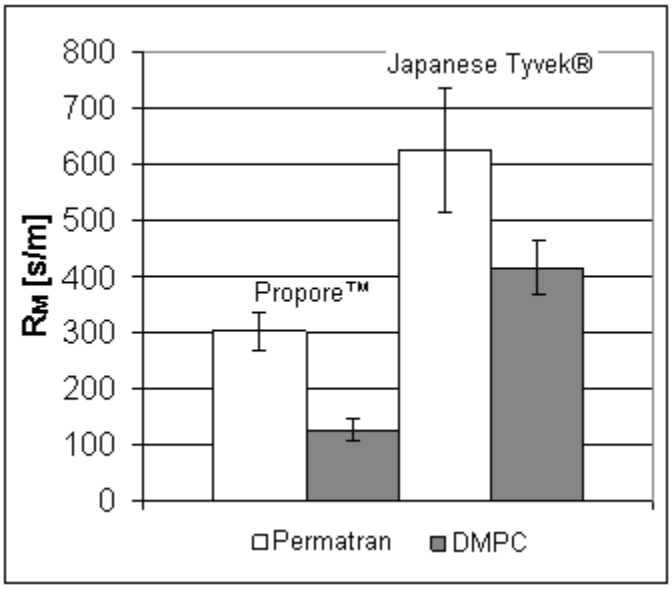

Figure 2.8. Comparison of the Propore™ and Japanese Tyvek® VDRs measured using the Permatran-W® to those obtained by Larson (2006) using the DMPC.

As observed in Figure 2.8, the VDRs obtained using the Permatran-W® were higher than those obtained using the DMPC and do not agree within experimental uncertainty. To understand the source of this discrepancy, a closer look at Gibson's (2000) findings is required. Gibson (2000) conducted measurements of many fabrics and membranes using many different test methods and apparatuses. Using the modified ASTM E96BW test apparatus, Gibson (2000) conducted two tests with the air flow tangential to the membrane at velocities of 0.5 m/s and 3.1 m/s and one test with perpendicular air flow at 6.5 m/s. Figure 2.9 is a plot of the VDR results obtained using the modified ASTM E96BW compared to the VDR results obtained using the DMPC for the same samples.

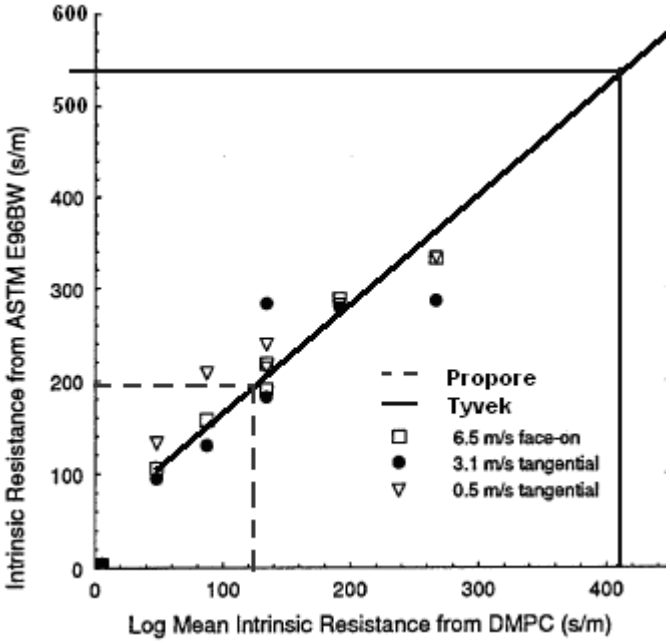

Figure 2.9. Comparison of the VDR measurements obtained for five different membranes using the ASTM E96BW, at three different flow conditions, to that obtained for the same five membranes using the DMPC (Gibson, 2000).

From Figure 2.9, it is clear that the modified ASTM E96BW measurements are consistently higher than the DMPC measurements regardless of the flow configuration. Furthermore, using the best fit shown in Figure 2.9, the points of intersection for Propore™ (125 s/m DMPC) and Tyvek® (415 s/m DMPC) are at 200 s/m and 540 s/m respectively. Thus, the membrane VDR results obtained using the Permatran-W® are more comparable to the ASTM E96BW than to the DMPC results adding confidence to the Permatran-W® measurements. However, the membrane VDRs should not depend on the test method used to determine them. This means that the Permatran-W® and ASTM E96BW test methods have an upward bias, or the DMPC has a downward bias, or both.

2.5.4 Nitrogen Leakage as a Source of Error in the Permatran-W® Results

One potential source of bias error in the Permatran-W® measurements is leakage of nitrogen from the test cell. In all of the Permatran-W® tests, the nitrogen flow rate decreased from the calibration value (typically around 1-2%) due to leakage. There are

two contact surfaces in the Permatran-W® at which the nitrogen could have leaked. The first contact surface is between the test membrane and the nitrogen chamber. However, this leakage would not affect the outlet relative humidity. The second contact surface is between the PTFE guard membrane and the test membrane. If leakage occurred at this site, the effect would be nitrogen flow through the test membrane. This flow would be in the opposite direction of the moisture diffusion, thus inhibiting the diffusion process. Therefore, the amount of vapour that diffused through the membrane would decrease, resulting in a lower nitrogen outlet relative humidity and an increase in the calculated VDR.

Larson (2006) measured the VDRs for Tyvek® and Propore™ over a range of pressure gradients induced across the membrane. The pressure gradient induced across the membrane created the potential for flow through the membrane. The observed VDRs at each of the pressure gradients are presented in Figure 2.10 with the corresponding volume flow rates of nitrogen measured at the outlet of the bottom stream.

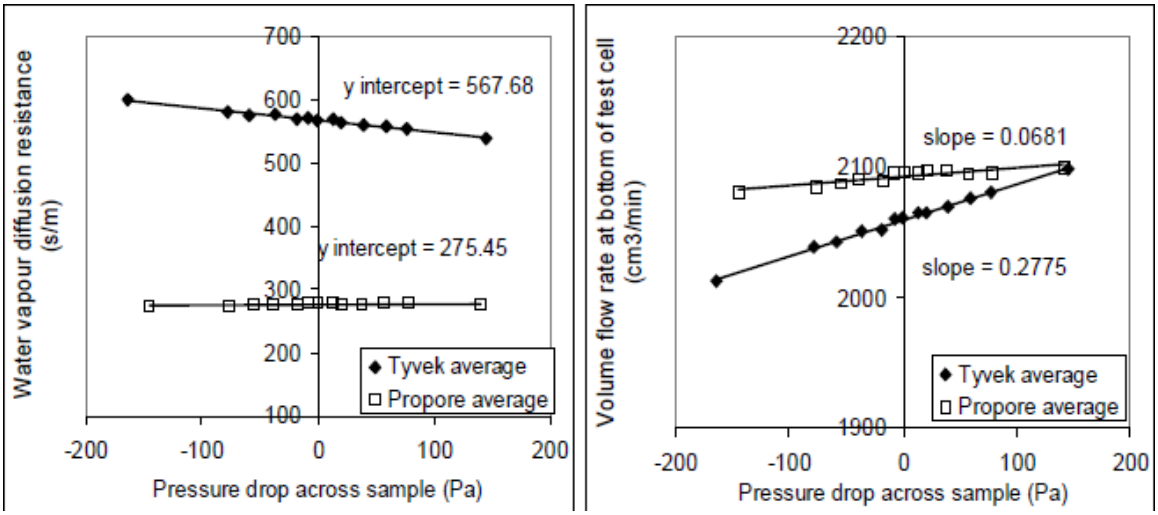

Figure 2.10. The effect of inducing a pressure gradient across the membrane on the observed VDR (Larson, 2006). Note: These water vapour diffusion resistances include the boundary layer resistances of the nitrogen stream.

As shown in Figure 2.10, the VDRs measured for Tyvek® were more sensitive to the induced pressure gradient than Propore™ due to the increased flow of nitrogen through Tyvek®. For Propore™, the pressure gradient created little flow of nitrogen through the membrane and thus had little effect on the VDRs. Therefore, it is unlikely that the small leakage observed in the Permatran-W® could have caused the large bias in the Propore™ VDR measurement. Furthermore, the impermeability of nitrogen through Propore™ would suggest that the leakage likely occurred at the interface of the test membrane and the nitrogen chamber not through the membrane. This location for leakage would have little effect on the observed VDR and as such leakage is likely not the cause of the bias observed in Figure 2.8.

2.5.5 Contact Resistance as a Source of Error in the Permatran-W® Results

Another possible source of bias in the Permatran-W® and the modified ASTM E96 BW of Figure 2.9 is an additional resistance caused by the contact between the ePTFE guard film and the test film. Gibson (2000) used the ISO 11092 test method to measure the VDR of various membranes for comparison to the DMPC measurements. As shown schematically in Figure 2.2 (b), the ISO 11092 test method also has a cellophane film, similar to PTFE, in contact with the test membrane. Therefore, if a contact resistance was present in the Permatran-W® and the modified ASTM E96BW, a similar bias error should be present in the ISO 11092 measurements.

Figure 2.11 presents the VDR results obtained by Gibson (2000) using the ISO 11092 test apparatus and plots these values against the VDR results obtained using the DMPC.

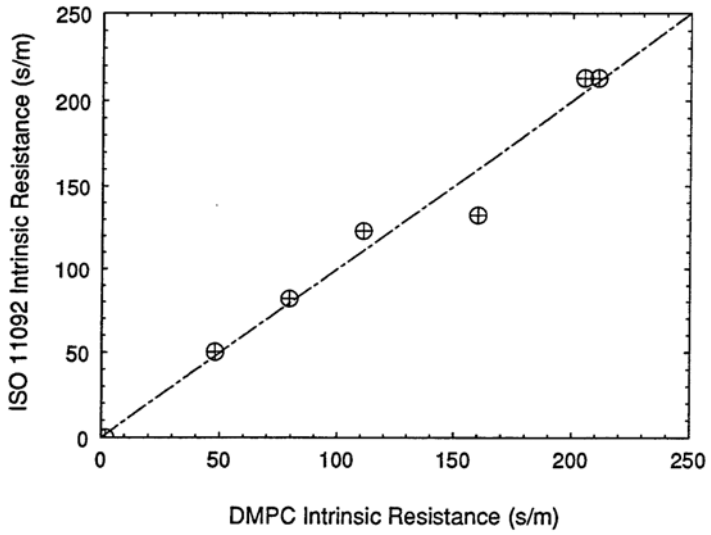

Figure 2.11. Comparison of Gibson's ISO 11092 membrane VDR results to those obtained using the DMPC (Gibson, 2000).

It can be seen in Figure 2.11 that the ISO 11092 membrane VDR measurements agreed well with the DMPC membrane VDR measurements. The ISO 11092 test apparatus did not yield VDR results with a similar bias to that observed in the Permatran-W® and modified ASTM E96 BW results. Therefore, it not likely that a contact resistance exists in either the Permatran-W® or modified ASTM E96 BW, eliminating this as a source of the bias observed in the VDR results.

2.5.6 Area Bias as a Source of Error in the Permatran-W® Results

The bias error in the Permtran-W® VDR results may be due to the test chamber construction (shown in Figure 2.5). The flow chamber diamater was measured to be 34.97±0.05 mm equating to an area of $(9.6\pm0.8)\times10^{-4}$ m^2. The measured area agrees with the default area used by the Permatran-W® of 0.001 m^2. However, the nitrogen flow in the Permatran-W® does not enter from the sides and is not fully developed as in the DMPC; Rather, the flow enters the test section through 1.25 mm ports in the bottom of the

3.1 mm high cylinder. In addition, the nitrogen inlets and outlets are angled towards one another as shown in Figure 2.5. Therefore, it is likely that near the edges of the test section the nitrogen is stagnant and the majority of the flow is bridging from the inlet to the outlet.

The flow through a Permatran-W® test section is a complex 3D viscous flow with entry effects, requiring a computational fluid dynamic numerical model to capture the flow behaviour properly. However, it is known that the nitrogen enters the chamber with a laminar Reynolds of 1500 and near the edges of the chamber there would be little to no air movement greatly increasing the boundary layer resistance. The increased boundary layer resistance at the edges of the chamber in effect reduce the area over which the bulk of the mass transfer occurs. For a fixed outlet concentration the WVTR is also fixed but decreasing the area will also decrease the VDR as shown in equation (2.4).

$$R_M = \frac{\Delta \overline{C} A}{\dot{m}} \tag{2.4}$$

A plot of the equivalent Permatran-W® Propore™ and Tyvek® resistances achieved by reducing the area for vapour transfer is shown in Figure 2.14 (a) and (b) respectively. Also plotted in Figure 2.14 is the DMPC resistances presented by Larson (2006) with experiemental uncertainty.

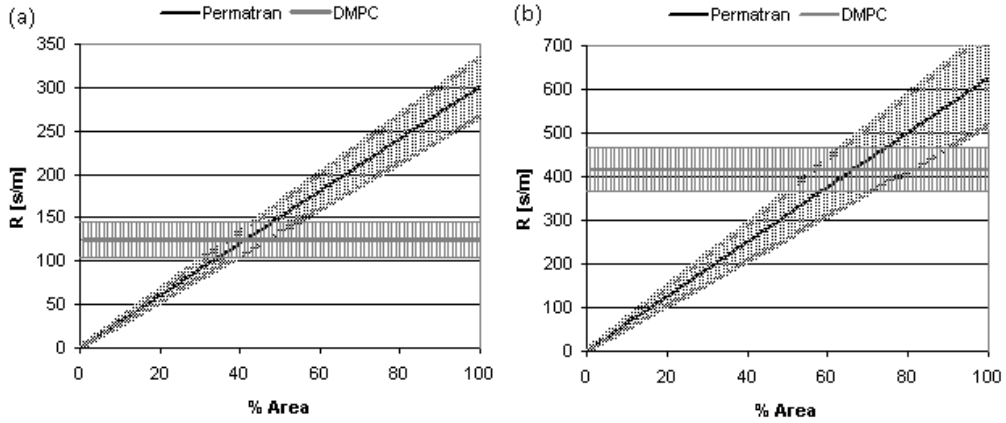

Figure 2.12. Intersection of the DMPC results (Larson, 2006) with the Permatran-W® results obtained by reducing the area of transfer for (a) Propore™ and (b) Tyvek®.

As shown in both Figure 2.14 (a) and (b), there is an area of intersection between the Permatran-W® and the DMPC results. For Propore™ (Figure 2.14 (a)) the Permatran-W® results agree within experimental uncertainty with the DMPC results for the range of % Area of (32-55) %. For Tyvek® (Figure 2.14 (b)) the Permatran-W® results agree within experimental uncertainty with the DMPC results for the range of Area of (50-90)%. Therefore, the Permatran-W® and DMPC results agree within experimental uncertainty for both Propore™ and Tyvek® for the range of % Area of (50-55) %. The diamter of the equivalent circular 52.5% area for mass transfer is 25.9 mm which seems resonable considering that the distance between the nitrogen inlet and outlet is 21.0 mm. The corrected VDRs and WVPs based on this new area are presented in Table 2.2.

Table 2.2. Summary of the new results obtained for the various membranes tested based on a percent area of 52.5% which equals a diameter of 25.9 mm for the equivalent circular transfer area of 0.000525 m^2.

	R_M (s/m)	U_{RM} (s/m)	k_m (kg/ms)	U_{km} (kg/ms)
Propore™	158	18	1.69E-06	2.04E-07
Tredegar VCL-510	1092	142	4.23E-07	5.64E-08
Tredegar #2	5793	1068	7.65E-08	1.43E-08
Aptra™ RKW	385	39	1.37E-07	1.47E-08
Porex® PM6M	84	10	1.61E-06	2.01E-07
Porex® PM3V	57	6	3.25E-06	3.51E-07
Porex® X-7744	102	13	7.10E-06	8.78E-07
Porex® X-4904	40	4	7.89E-06	8.24E-07
Japanese Tyvek®	329	57	6.50E-07	1.21E-07
Tyvek® 1025B	245	92	7.14E-07	2.70E-07
Tyvek® 1059B	215	42	9.70E-07	2.09E-07
AY Tech ePTFE Lam	97	11	6.63E-06	7.68E-07

2.5.7 Boundary Layer Distribution

For high VDR membranes the mass flux will be relatively constant throughout the chamber. However, for low VDR membrane the boundary layer distribution will create a mass flux distribution. Three possible mass flux distributions through the test cell are shown in Figure 2.13. The original distribution is representative of the assumtion made in the calculation of the VDRs presented in Table 2.1 and the equivalent distribution is the assumtion used to calculate the VDRs of Tabl2 2.1.

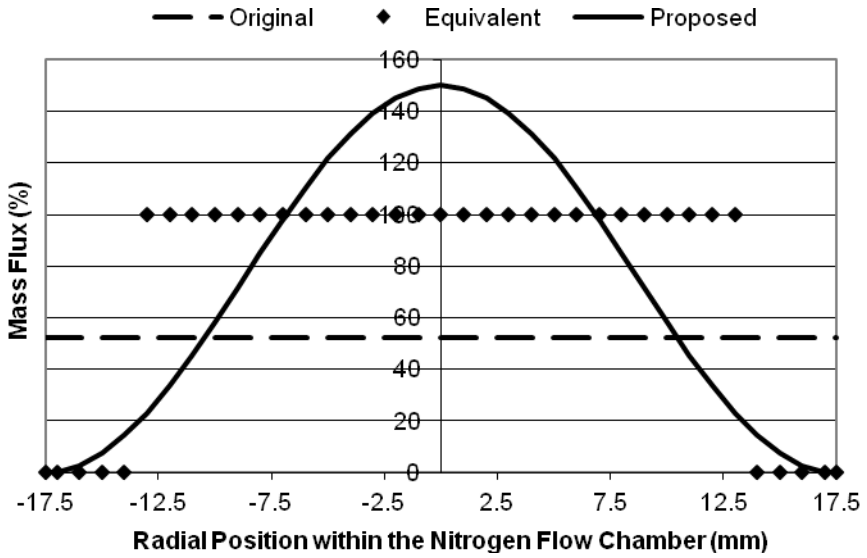

Figure 2.13. The different distributions of mass transfer assumed to calculate the area for transfer in the Permatran-W® test cell.

The Permatran-W® assumes that the mass flow is uniformly distributed throughout the test section and would have a mass flux distribution shown as the "original" plot in Figure 2.14. By reducing the area to 52.5% and fixing the net flow of vapour, a new mass flux distribution through the test cell is obtained. However, likely neither the "original" nor the "equivalent" distributions are accurate representations of the true distribution in the test cells. The nitrogen in the test cells undergoes a rapid expansion upon entering the test

chamber and then exits through a sudden contraction. Therefore, the velocity is not uniform throughout the test section, which would cause a variation in the convective mass transfer coefficient. The variation in the convective mass transfer coefficient is reflected by variance in the boundary layer resistence of the nitrogen chamber and would likely create a mass flux distribution closer to the "proposed" distribution of Figure 2.13.

Although the exact distribution in mass flux within the Permatran-W® test cells is not known, it is known that the distribution is caused by a boundary layer resistance distribution. To obtain the "original" mass flux distribution in Figure 2.14 the boundary layer resistance would need to be uniform (500 s/m). Therefore, varying the boundary layer resistance across the transfer area will result in a different membrane VDR. To vary the boundary layer distribution the sample area is divided into A_1=52.5% (Rb_1) and A_2=47.5% (Rb_2). Rbl_1 is varied from 260 s/m to 500 s/m and Rbl_2 is calculated using equation (2.5).

$$Rbl_2 = \left(\frac{1}{500 s/m} - \frac{\%A_1}{Rbl_1} \right)^{-1} \%A_2 \qquad (2.5)$$

where, Rbl_1 = the boundary layer resistance for area 1 [s/m],

Rbl_2 = the boundary layer resistance for area 2 [s/m],

$\%A_1$ = the first area for mass transfer (0.525),

$\%A_2$ = the second area for mass transfer (0.475).

The resistive circuits used to analyze the effect of varying the boundary layer resistance over the transfer area are presented in Figure 2.15. The total resistance is what is measured by the Permatran-W®. Therefore, by varying the boundary layer resistances the effect on the total resistance and membrane resistance can be investigated.

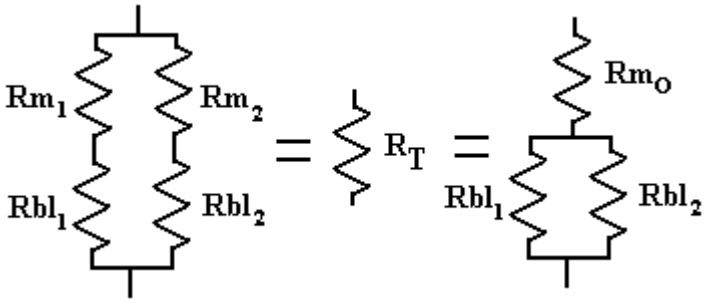

Figure 2.14. Schematic detailing the resistive circuits used to determine the observed membrane resistance.

As shown in Figure 2.14, the two area resistance are placed in parallel with each other and each consist of a membrane resistance (Rm_1=(Table 2.2 VDR)*0.525, Rm_2=(Table 2.2 VDR)*0.475) in series with the boundary layer resistances (Rbl_1 and Rbl_2 respectively). These resistances are used to calculate the equivalent total resistance (R_T). The observed membrane resistance (Rm_O) is calculated by subtracting the boundary layer resistance in parallel with each other from the total resistance. The observed membrane resistance is the theoretical resistance obtained assuming that the mass flux is uniform through the test cells ("original" in Figure 2.13).

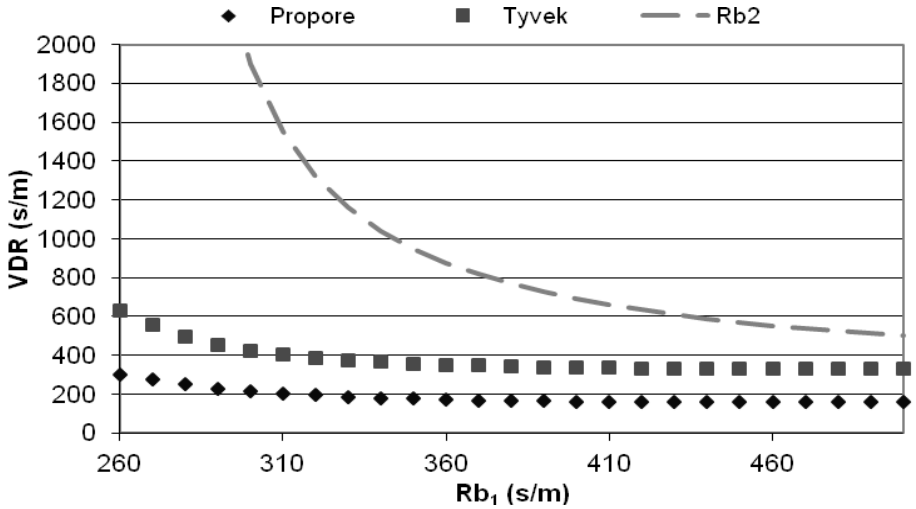

Figure 2.15. The observed Propore™ and Tyvek® membrane resistance using different boundary layer resistances where Rbl_1 corresponds to A_1=52.5% and Rbl_2 corresponds A_2=47.5%.

Figure 2.15 clearly demonstrates that if there is a variation in the boundary layer resistance across the transfer area will impact the observed membrane VDR (output by the Permatran-W®). If the boundary layer resistance below the membrane were uniformly equal to 500 s/m, the uniform mass flux assumption would yield the correct membrane VDR. Thus, the further the boundary layer resistances deviate from uniform the larger the upward bias in observed membrane resistance.

There are an infinite number of boundary layer distributions which would yield the observed membrane resistances (biased) presented in Table 2.1. For a given boundary layer resistances acting on A_1 (Rbl_1), there is a corresponding boundary layer resistance (Rbl_2), which would cause the observed membrane VDR's to be as presented in Table 2.1, if the actual membrane VDR's were as presented in Table 2.2. Pairs of boundary layer resistances are plotted in Figure 2.16 which yield a VDR of 301 s/m (Propore™, Table 2.1) assuming the correct membrane VDR is 160 s/m (Propore™, Table 2.2).

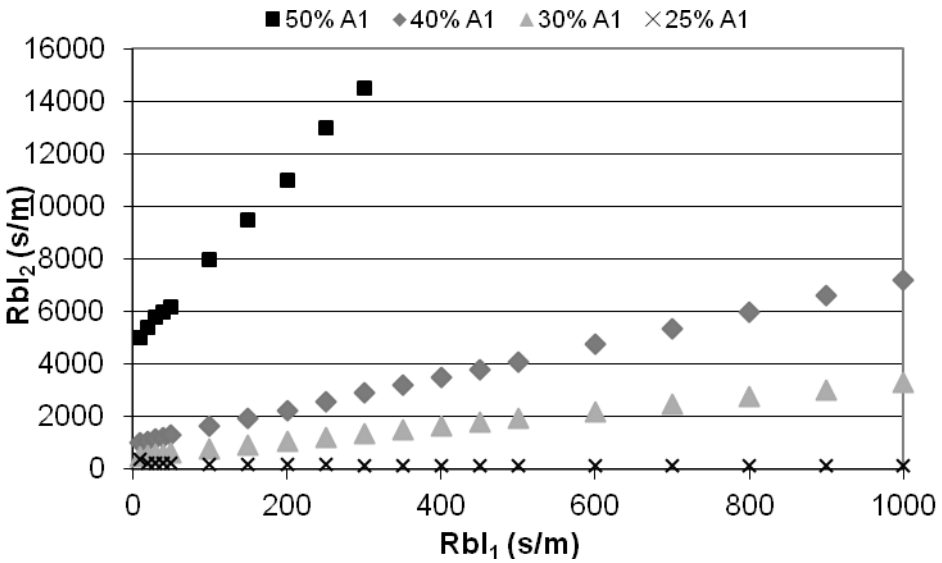

Figure 2.16. Boundary layer vapour diffusion resistances distributions which yield a fixed observed membrane VDR of 301 s/m while the actual membrane resistance is 160 s/m.

2.6 Conclusions from the Membrane Vapour Diffusion Results

The VDR results presented in Table 2.1 are subject to many possible sources of error with the most significant source being the variation in boundary layer resistance in the Permatran-W® nitrogen stream. To accurately use the Permatran-W® measurement to determine the membrane VDR's and permeabilities, more information regarding the boundary layer resistance distribution is required. However, by altering the area for transfer to 52.5% of the total membrane area, agreement with the DMPC results presented by Larson (2006) was obtained. Although the Permatran-W® VDR results are suspect, they do provide a good means for comparing one membrane to another.

Based on the membrane VDR measurements presented in Table 2.2, it is clear that the previously used Propore™ and Tyvek® are not the lowest resistance membranes tested. Therefore, the RAMEE performance can be improved by replacing Propore™ (VDR=158±18 s/m) with any of the lower VDR membranes such as the Porex® membranes (VDR= 40-120 s/m) or the AY. Tech ePTFE Lam. membrane (97±11 s/m). In addition, the VDR of Propore™ (158±18 s/m) was measured to be lower than the Tyvek® 1025B and 1059B membranes (245±92 s/m and 215±42 s/m respectively) used by Dave Thompson in the enthalpy pump system.

CHAPTER 3

LIQUID PENETRATION PRESSURE AND MECHANICAL PROPERTIES

The vapour diffusion resistance of a membrane used to construct a RAMEE is critical to the effectiveness of the system as discussed in Chapter 2. In addition, the liquid penetration pressure must also be known to prevent the desiccant from leaking into the airstreams under normal operation. The membrane strength and elasticity are also critical to the design of the RAMEE to prevent large deflections and/or rupture. Therefore, a suitable membrane cannot leak, rupture, or deflect significantly under the normal operating pressures of the RAMEE system. Unfortunately, membrane properties are often guarded by the manufacturers, not known, or if known, cannot be directly compared due to the wide range of testing methods used. Therefore, the liquid penetration pressure (LPP) and modulus of elasticity of each of the membrane alternatives needs to be measured.

The LPP is the water pressure at which liquid water will pass through a membrane. Larson (2006) measured the LPP of his membrane alternatives and approximated the design pressure for the RAMEE to be 33 kPa (4.8 psi). In the laboratory, Mahmud (2009) observed that the operating pressures of RAMEE Prototype 3 were below 35 kPa (5 psi). Therefore, a membrane that does not leak below 35 kPa (5 psi) would be suitable to replace Propore™.

The desiccant pressures in the RAMEE stress the membrane in the transverse direction (in plane with the membrane) which creates a strain in this same plane. The

lower the membrane modulus of elasticity, the more the membrane will deflect, creating variations in the RAMEE flow channels. Variations in the RAMEE flow channels create flow maldistributions which decrease the RAMEE effectiveness. Prototype 2 (Erb, 2009) and Prototype 3 (Mahmud, 2009), constructed using Propore™ had significant membrane deflections. Therefore, the modulus of elasticity of the replacement membrane should exceed that of Propore™.

In the sections to follow, the apparatuses and methods used to measure the LPP and determine the modulus of elasticity are described. The results of these tests are presented and compared to the manufacturer specified properties and published data. Lastly, the sources of error in the measurements and measurement methods are discussed and conclusions are made.

3.1 The Bulge Test Apparatus

The bulge test apparatus is designed to hold a membrane sample with pressurized water on the bottom and atmospheric air on the top. By varying the water pressure below the membrane, the LPP can be observed. By measuring the membrane deflections with water pressures below the membrane, the membrane stiffness can be obtained. Pressurized air is connected to a sealed water reservoir that is connected to the underside of the membrane in the test cell. Thus, the desired liquid penetration pressure below the membrane can be obtained by regulating the air pressure supplied to the reservoir. Larson (2006) utilized a line pressure of 344 kPa (50 Psi) with a regulator valve. However, this system was replaced with the Druck DPI 605 to generate more accurate and controllable air pressures.

The pressure output by the Druck is close to the liquid pressure in the test cell, observed below the membrane using a pressure transducer. However, slight differences

in these pressures would be obtained due to the static head of water, in the reservoir, changing throughout the tests. The pressure transducer outputs a voltage that is linearly proportional to the pressure being measured. The transducer output is amplified and displayed on a voltmeter. With elevated water pressures below the membrane and atmospheric pressure above, the membrane will deflect. The deflections can be measured using a linearly variable displacement transducer (LVDT). The LVDT outputs a voltage that is linearly proportional to the position. This voltage is also amplified and observed using a voltmeter. A schematic of the bulge test apparatus is shown in Figure 3.1.

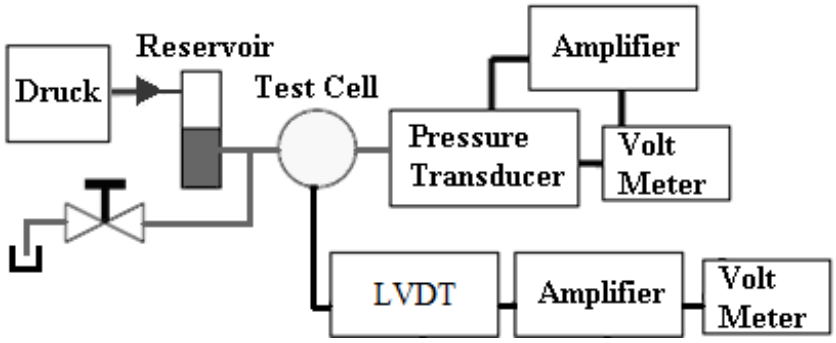

Figure 3.1. Schematic of the bulge test apparatus used to measure the liquid penetration pressures and determine the modulus' of elasticity of the membrane alternatives.

The pressure transducer and the LVDT calibration procedures, and the methods used to obtain the measurement uncertainties, are outlined in Appendix C.1. Furthermore, how these measurement uncertainties impact the modulus of rigidity uncertainty is outlined in Appendix C.2. Typical measurement uncertainties obtained using the methods outlined in Appendix C.1 are presented in Table 3.1.

Table 3.1. Typical measurement uncertainty obtained for the pressure transducer and LVDT.

Pressure Transducer	0.05 (psig)	345 (Pa)
LVDT	0.26 (mm)	0.010 (in.)

3.2 Liquid Penetration Measurement Method

3.2.1 Bulge Test Apparatus Configuration

The test cell used in the bulge test apparatus was design and built by Larson (2006). Larson (2006) designed the test cell to meet the requirements of the modified AATCC test method 127 (2003) built in accordance with the ASTM F 903 (2004). However, some membranes deflect significantly during LPP testing and burst due to the large stresses/strains induced during testing. These bulk deflections would likely alter the actual liquid penetration pressure by deforming the pores of the membranes. Furthermore, the stresses/strains caused by the bulk deflections are not representative of in situ stresses/ strains within the RAMEE. Therefore, as shown in Figure 3.2, the same screen used to support the membrane within the RAMEE is used to reduce bulk deflections in the membrane during LPP testing.

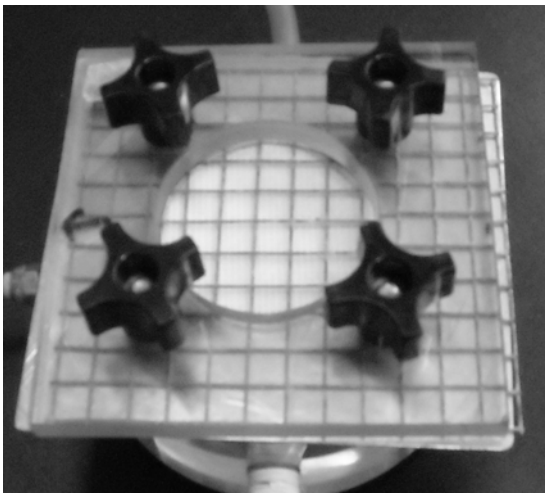

Figure 3.2. Photographs of the bulge test apparatus configured to measure the LPP. Note the outer screen used to provide support to the membrane preventing significant deflections.

In addition to the outer screen, a 1.58 mm (1/16”) thick stainless steel plate was placed between the outer screen and the membrane. The steel plate gives even clamping

pressure on the gasket below the membrane, creating a seal. The steel plate had a hole that is the same size as the 12.7 mm (½") thick plastic plate placed on top of the screen to maintain the area for leakage to occur during testing.

3.2.2 Measurement Methodology

The pressurization rate is critical when measuring the LPP. Larson (2006) held the pressure constant for a piece of Tyvek® and checked the membranes twice daily for liquid penetration. Larson observed that for short exposure times (less than an hour) the observed liquid penetration pressure for Tyvek® was around 18 kPa (2.6 Psi). However, when the exposure time was increased to 5 days the observed liquid penetration pressure was for Tyvek® was reduced to 6 kPa (0.9 Psi). This demonstrated that the time of exposure to the water pressure can dramatically affected the observed LPP. During normal operation, the RAMEE pressures are elevated for long durations of time. Therefore, testing membrane LPP's with a slow pressurization rate will be more representative of the LPP's during normal operation within the RAMEE.

In the AATCC test method 127 (2003), the pressure is increased at a constant rate of 6 kPa/min (0.9 Psi/min) for the "low pressure test" and 49 kPa/min (7 Psi/min) for the "high pressure test". In the ASTM F 903 (2004) test method, the pressure is held constant for a specified time and a pass fail system is used. For both test methods, the LPP is recorded when three water droplets are visible on the surface of the membrane. The LPP measurements obtained using the bulge test apparatus were made by increasing the liquid pressure in 3.45 kPa (0.5 Psi) intervals every minute. Once the pressure was increased, the membrane surfaces were inspected for the remainder of the minute. Once three water droplets were observed of approximately 0.25 mm or greater were visually observed, the pressure transducer voltage was recorded as the LPP.

3.3 Modulus of Elasticity Measurement Method and Data Analysis

Larson (2006) utilized many test methods to measure the modulus of elasticity including ASTM D 882, ASTM D 4595, the secant method, energy minimization method, and linear fit method. The ASTM test methods utilize the Instron tension-testing machine to test strips of the membrane, while the remaining methods utilized the bulge test apparatus. Larson compared the results obtained using the different methods and concluded that the bulge test analyzed using the secant method was the "most effective and easily attainable elastic modulus (method)" (Larson, 2006). Due to the number of membrane alternatives, and based on Larson's recommendations, the bulge test using the secant method of analysis was selected to determine the membrane modulus of elasticity values.

Larson (2006) measured the modulus' for these membranes over a range of relative humidities and found that the relative humidity had a negligible effect on the results. Therefore, controlling the relative humidity was deemed unnecessary for these tests. Larson (2006) also investigated the effect of strain rate on the modulus' of Tyvek® and Propore™. The results of Larson's (2006) study are presented in Figure 3.3 (a) for Tyvek® and Figure 3.3 (b) for Propore™.

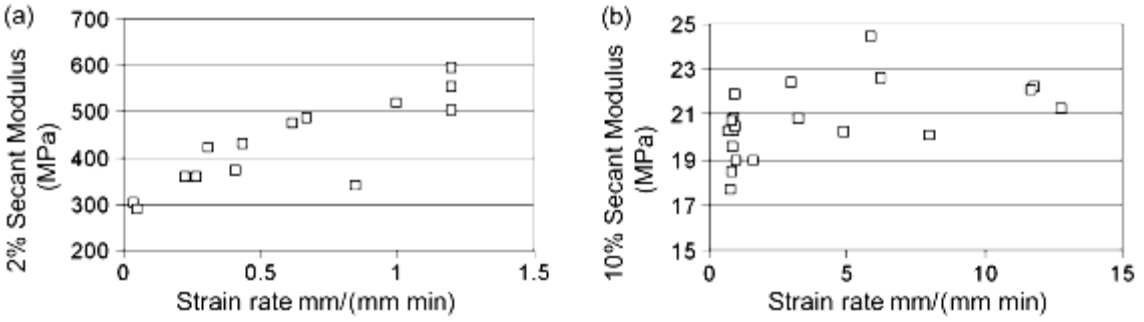

Figure 3.3. Effect of strain rate on the membrane modulus of elasticity obtained by Larson (2006) for (a) Tyvek® and (b) Propore™.

As shown in Figure 3.3, Larson (2006) found that the modulus for Tyvek® was sensitive to the strain rate. To be representative of the RAMEE under normal operation a slow strain rate (less than 0.1 mm/mm/min) was selected.

3.3.1 Bulge Test Apparatus Configuration

A photograph of the bulge test cell configured to conduct modulus measurements is shown in Figure 3.4. The LVDT stallis is placed in the center of the membrane measurement area. The LVDT voltages are converted to displacements using the calibration curve as shown in Appendix C.1.

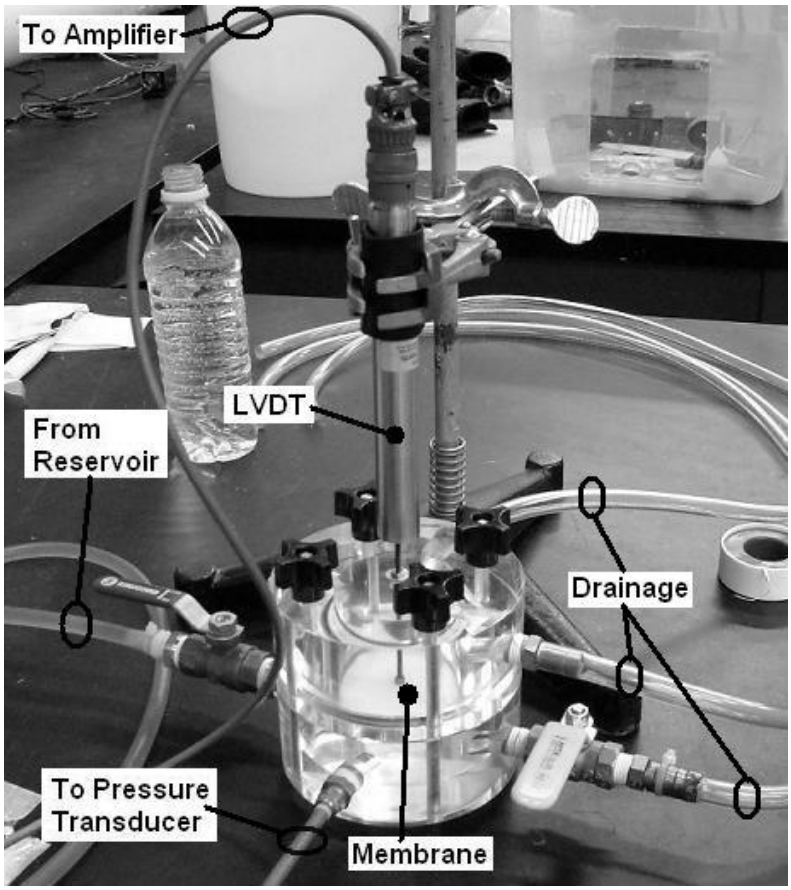

Figure 3.4. Photograph of the bulge test cell configured to determine the membrane modulus of elasticity.

3.3.2 Determining the Stress Strain Curves

The modulus of elasticity of the membrane alternatives is determined from the LVDT and pressure transducer measurements. The LVDT and pressure transducer voltages are converted to displacements and liquid pressures respectively using the calibration curves (see Appendix C). The membrane samples within the bulge test cell are assumed to follow a spherical deflection, as shown in Figure 3.5. Also, the membranes are thin (0.04-0.6 mm) and thus have negligible bending stiffness.

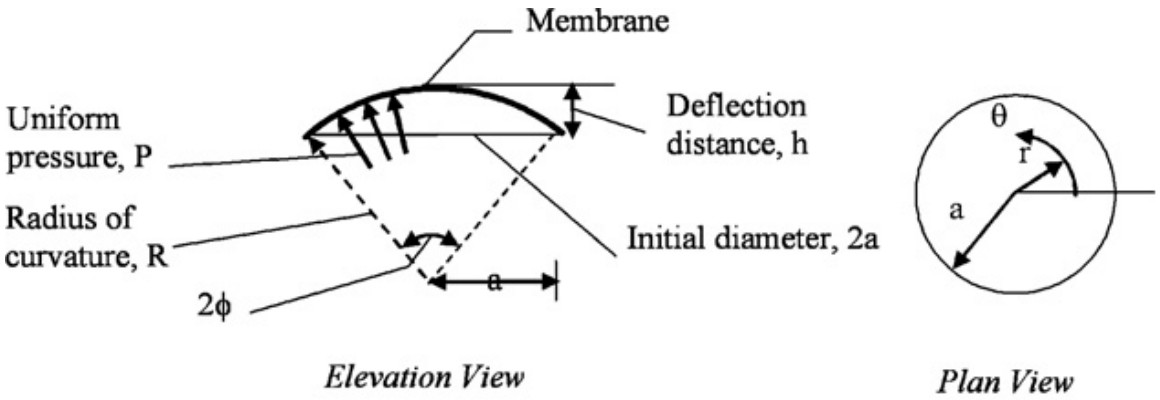

Figure 3.5. Schematic of the membrane deflections in the bulge test apparatus. Note: the deflections are assumed to be spherical (Larson et al., 2006).

The pressure measurements are converted to tensile stresses in the θ-r plane (shown in Figure 3.4) using equation (3.1) (Small & Nix, 1992). Built into equation (3.1) are the assumptions that the strain is in the elastic region and that the membrane deflections are much smaller than the bulge test cell radius.

$$\sigma = \frac{Pa^2}{4h\Delta z} \tag{3.1}$$

where, σ = the tensile stress induced on the membrane in the θ-r plane [Pa],

P = the liquid pressure below the membrane [Pa],

a = the radius of the bulge test cell [28.5±0.1 mm],

h = the membrane deflections [mm],

Δz = the membrane thickness (see Table 2.1) [mm].

The θ component of the strain is also required to determine a membrane modulus of elasticity. Equation (3.2) (Small & Nix, 1992) is used to convert the deflection measurements to θ component strains.

$$\varepsilon_\theta = \frac{2h^2}{3a^2} \tag{3.2}$$

where, ε_θ = the θ component of the membrane strains [mm/mm],

A typical plot of the results of equations (3.1) and (3.2) is shown in Figure 3.6. Based on Larson's recommendation, the secant method is used to determine the slope of a straight line drawn from the origin to the point of 0.1 strain as detailed in Figure 3.5.

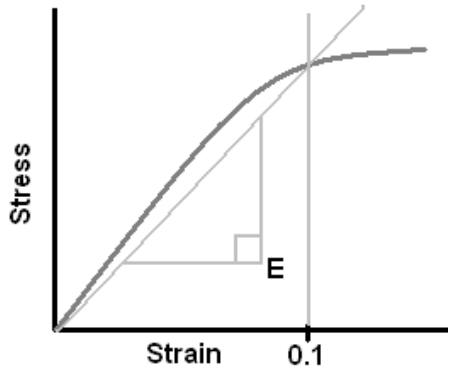

Figure 3.6. A typical membrane stress strain relationship and shows the 10% secant method used to determine the modulus of elasticity.

3.4 Bulge Test Results

3.4.1 Membrane Liquid Penetration Pressure Results

The liquid penetration pressures (LPP) were measured for each of the membrane alternatives. The maximum measurable pressure was 12 Psi (82 kPa) which exceeded the

desired LPP of >5 Psi (34 kPa). The LPP was measured four times for each membrane alternative and the average observed pressures are presented in Table 3.2.

Table 3.2. Liquid penetration pressure measured for the various membrane alternatives. Note: Due to the test trajectory the uncertainty in the LPP results is approximately 0.5 Psi (3 kPa).

	LPP (psig)	LPP (kPa)
Propore™	>12	>82
Porex® PM3V	7.2	49
Porex® X-7744	2.2	15
Porex® X-4903	1.4	9
RKW	>12	>82
Tredegar #2	>12	>82
Japanese Tyvek®	2.8	19
Tyvek 1025B	2.3	16
Tyvek 1059B	2.4	17
AY Tech ePTFE Lam.	>12	>82

As shown in Table 3.2, the LPP of Propore™, Porex® PM3V, RKW, Tredegar #2, and the AY Tech. ePTFE Lam. Membranes all exceeded the design LPP of 34.5 kPa (5 psig). The LPP measured for Tyvek® is compared to that observed by Larson (2006) and specified by the manufacturer in Figure 3.7. Also contained in Figure 3.6 is a comparison of the Porex® PM3V membrane LPP to the manufacturer specified value.

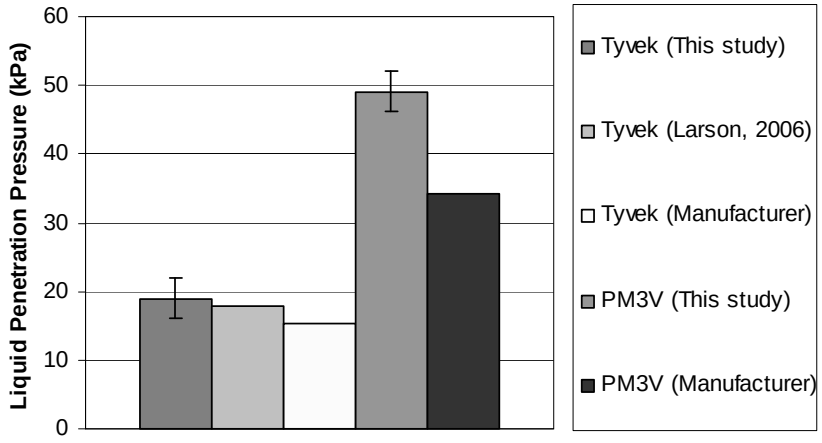

Figure 3.7. Comparison of the LPP for observed for Tyvek® and Porex® to previously published results.

As shown in Figure 3.7 the Tyvek® LPP agreed within experimental uncertainty with both Larson's (2006) and the manufacturer specified values. The Porex® PM3V value did not agree within experimental uncertainty with the manufacturer value. However, the test method was not specified by the PM3V manufacturer which has a large effect on the result. For Propore™, the LPP exceeded the maximum measurable pressure of 82 kPa (12 Psi). Larson (2006) also found that the LPP exceeded his measurement capabilities of >276 kPa (40 Psi). This supported the 3M™ specified >345 kPa (50 Psi) LPP. Furthermore, AY Tech. guaranteed the ePTFE laminate LPP to exceed 34 kPa (5 Psi) and when tested the membrane did not leak below the maximum test pressure of 82 kPa (12 Psi). Based on the good agreement for Tyvek® with Larson's (2006) and the manufacturer specified value, the LPP's of Table 3.1 likely conform to the AATCC test method 127 (2003) despite using a slower pressurization rate (3.5 kPa/min vs 6.2 kPa/min) (0.5 Psi/min vs 0.9 Psi/min).

3.4.2 Membrane Modulus of Elasticity Results

When the membranes were installed in the bulge test cell there was no pre-stress placed on the membranes. Large deflections were observed initially at very low pressures due to the initial slack in the membrane. The large initial deflections caused an upward offset in the stress strain curves. Therefore, to remove this offset the membranes were pre-stressed 0.5 kPa (0.07 psig). This pressure was enough to remove any initial slack in the membranes and became the new zero point of the stress strain curves. This shift created accurate stress strain curves that intersect at the origin. The resulting zero offset stress strain curves obtained for the membranes are shown in Figure 3.8.

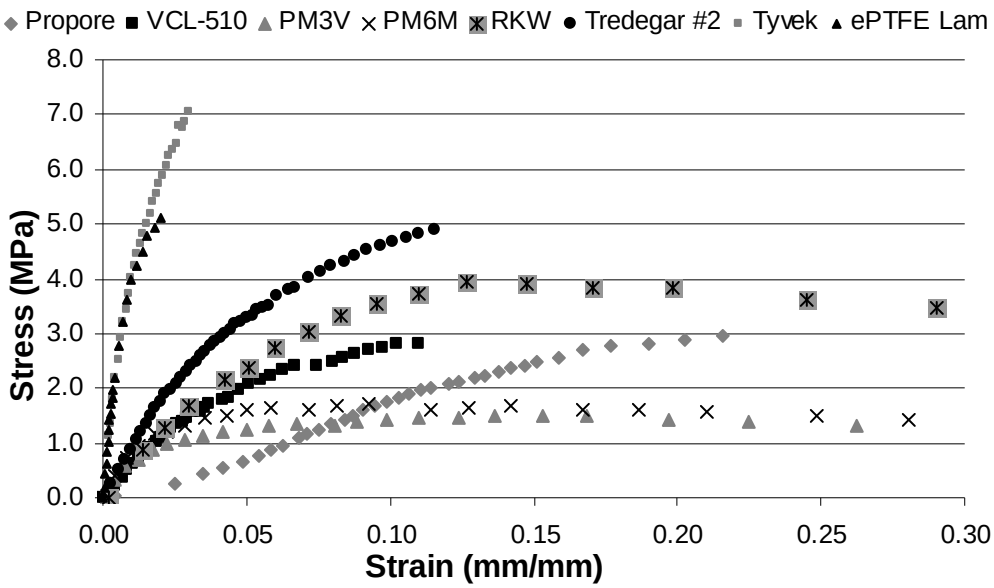

Figure 3.8. The stress strain relationships obtained for the membranes using the bulge test apparatus. Note: the zero is offset to the slack removing pressure of 0.5 kPa (0.07 psi).

The maximum pressure that could be measured by the pressure transducer was 82 kPa (12 Psi). This test pressure is higher than the typical operating pressure within the RAMEE (34.5 kPa,5 Psi) and was sufficiently high to attain a 0.1 strain for most of the membranes. However, the Japanese Tyvek® and AY Tech. ePTFE Lam. membranes were too stiff to obtain a 0.1 strain at the maximum test pressure. Therefore, to obtain the modulus of elasticity for these membranes, using the secant method, a 0.01 strain was used. The membrane modulus of elasticity results are presented in Table 3.3.

Table 3.3. Summary of the membrane modulus of elasticity results obtained from the stress strain curves of Figure 3.7 using the secant method.

	E (MPa)	U_E (MPa)
Propore™	17	2
Tredegar VCL-510	54	10
Tredegar #2	45	10
Porex® PM3V	12	1
Porex® PM6M	16	1.7
RKW	35	7
Japanese Tyvek®	382	72
AY Tech ePTFE Lam.	387	32

As presented in Table 3.3, all but the Porex® PM3V membrane modulus of elasticity results exceeded the desired modulus of Propore™. The uncertainty in the modulus of elasticity results was determined in accordance with ASME/ANSI PTC 19.1 (1998). Since only four samples were taken the majority of the uncertainty was caused by the variations in the observed modulus of elasticity. The details of this analysis are shown in Appendix C.

To validate the modulus' of elasticity presented in Table 3.3, the modulus' obtained for Tyvek® and Propore™ are compared to those obtained by Larson (2006) in Figure 3.9.

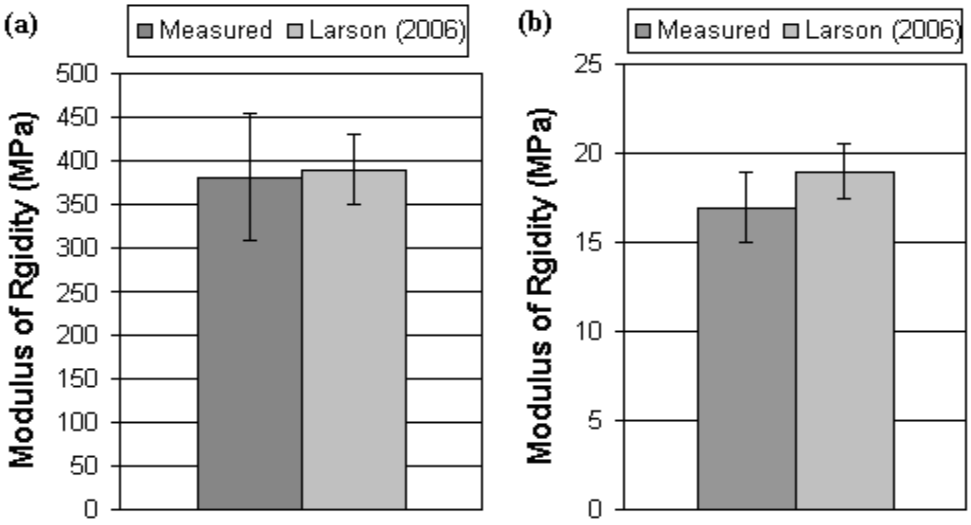

Figure 3.9. The measured modulus of elasticity compared to that presented by Larson (2006) for (a) Tyvek® and (b) Propore™.

As shown in Figure 3.9, the modulus' results for both Tyvek® and Propore™ agree within the experimental uncertainty with those obtained by Larson (2006).

3.5 Conclusions from the LPP and Modulus of Elasticity Results

A suitable membrane used to replace Propore™ for use in the RAMEE should have a LPP higher than 34 kPa (5 Psi) and a modulus of elasticity higher than Propore™ (17 MPa). Based on both the LPP's presented in Table 3.1 and the modulus of elasticity results of Table 3.2, the RKW, Tredegar #2, and AY Tech. ePTFE laminate membranes are suitable replacements for Propore™. However, as presented in Chapter 2, the vapour diffusion resistance (VDR) of a suitable membrane should be less than that obtained for Propore™. Based on the VDR results, presented in Table 2.1, the LPP results, presented in Table 3.2, and the modulus of elasticity results, presented in Table 3.3, the only membrane measured that met all of the performance criteria is the AY Tech ePTFE laminate membrane.

CHAPTER 4

RUN-AROUND MEMBRANE ENERGY EXCHANGER PERFORMANCE EVALUATION

In order to demonstrate the run-around membrane energy exchanger (RAMEE), the system should be tested in a building ventilation system. However, RAMEE prototype 4 would be constructed with a new membrane, which introduced unknowns and associated risk. Therefore, it was decided to test a laboratory model RAMEE prototype 4 to further investigate the performance characteristics and trouble shoot the new membrane. The laboratory exchangers tested had the same height and length as the designed field exchangers (Note: See attached Appendix D for laboratory exchanger drawings), but the width was reduced from 24 in. (610 mm) to 4in (100 mm). By scaling the exchangers the edge effects will be more significant in the laboratory model.

The energy exchanger test facility was used to determine the effectiveness of RAMEE prototype 4 over a range of desiccant flow rates and air flow rates. This chapter outlines the energy exchanger test facility, the test results obtained for RAMEE prototype 4, and conclusions drawn from these results.

4.1 Energy Exchanger Test Facility

The energy exchanger test facility was designed and built by Erb (2007) to evaluate the performance of energy exchangers in a laboratory setting. The energy exchanger test facility was designed to maintain the AHRI 1060-2005 standard testing conditions presented in Table 4.1.

Table 4.1. American Heating and Refrigeration Institute 1060-2005 standard test conditions.

Summer	Supply Inlet	35 °C	50% RH
	Exhaust Inlet	24 °C	50% RH
Winter	Supply Inlet	1.7 °C	80% RH
	Exhaust Inlet	21 °C	50% RH

The following sections outline how the energy exchanger test facility is used to maintain the 1060-2005 test conditions and what measurements are obtained with associated uncertainties. A schematic of the energy exchanger test facility is presented in Figure 4.1 The details of the desiccant pumping and control box shown in Figure 4.1 are presented schematically in Figure 4.2.

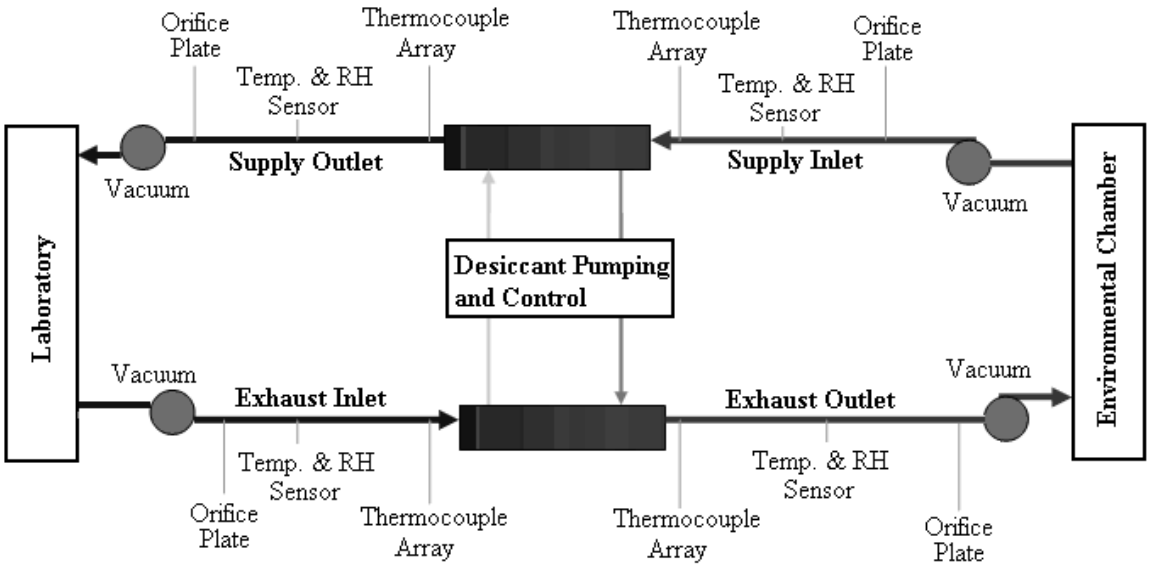

Figure 4.1. Schematic of the energy exchanger test facility showing the air side configuration including the vacuums, orifice plates, temperature/relative humidity sensors, and thermocouple arrays.

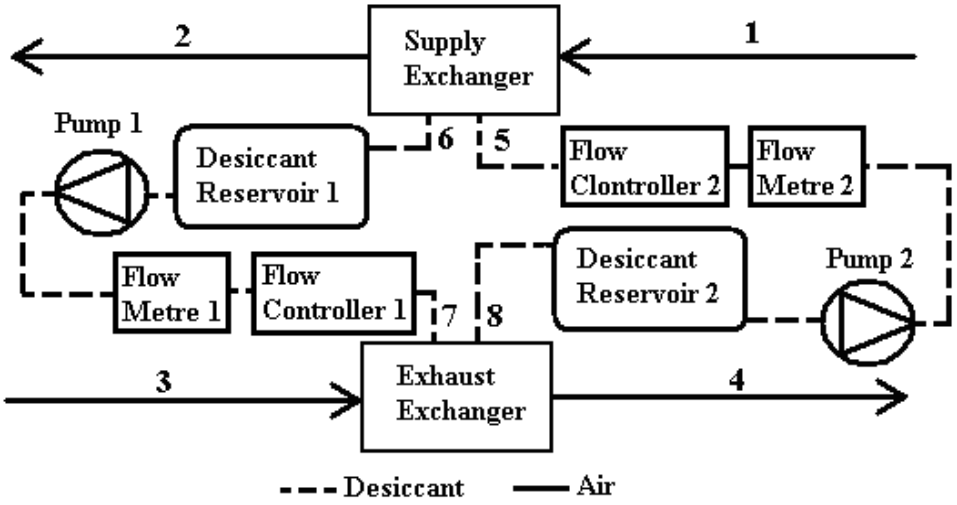

Figure 4.2. Schematic of the energy exchanger test facility desiccant pumping and control loop. The numerical legend is as follows: 1-supply air inlet, 2-supply air outlet, 3-exhaust air inlet, 4-exhaust air outlet, 5 supply desiccant inlet, 6-supply desiccant outlet, 7-exhasut desiccant inlet, 8-exhaust desiccant outlet.

4.1.1 The Air Side Flow Path in the Energy Exchanger Test Facility

As shown in Figure 4.1, the energy exchanger test facility uses four vacuum pumps to generate the airflow through the supply and exhaust exchangers. The vacuums are configured in a draw/blow configuration such that the air pressure through the exchangers is near atmospheric. Each vacuum is connected to the power source through a variable transformer. By adjusting the variable transformers, the electrical power supplied to each of the four vacuums can be set to obtain the desired test airflow rate.

The supply air inlet is drawn from an environmental chamber. The chamber has both temperature and relative humidity control, which are active during testing due to the chamber having a volume change rate time constant of approximately once per 6 hours (i.e. less than test duration). The chamber uses a refrigeration loop to maintain the desired temperature of the air and a steam generator to maintain elevated moisture contents. The first of the four vacuums draw the air from the chamber and then pass the

air through a series of flow conditioners and measurement devices. The air then enters the supply exchanger, where it gains or losses heat/moisture depending on the test conditions. The supply outlet air stream is drawn through another series of flow conditioners and measurements devices by the second vacuum. The vacuum then blows the supply outlet air into the laboratory which has a volume change rate time constant of approximately 600 hours (i.e. much longer than any test).

The exhaust inlet air stream is drawn from the laboratory by a third vacuum. However, prior to the vacuum the laboratory air passes through an evaporative cooler to lower the temperature and increase the relative humidity. Upon exiting the vacuum the air stream is blown through a series of flow conditioners and measurement devices similar to the supply inlet. The air stream enters the exhaust exchanger gaining/loosing heat/moisture depending on the test conditions. The exhaust outlet air is drawn through another series of flow conditioners and measurement devices by the fourth vacuum pump. The exhaust outlet air stream is then blown into the environmental chamber completing the airside loop.

The airflows are transported in the energy exchanger test facility through 2 in. (50.8 mm) polyvinyl chloride piping. However, the RAMEE Prototype 4 exchangers have inlets/outlets measuring 12 in. (300 mm) high by 4 in. (100mm) wide. Therefore, to connect the 2 in. (50.8 mm) piping to the exchangers, four round to rectangular transition ducts with 10° angle of expansions are used. The 10° angle of expansion is intended to eliminate flow separation and helps ensure uniform inlet face velocities.

4.1.2 Air Side Measurements in the Energy Exchanger Test Facility

After the supply and exhaust inlet vacuums, the air stream passes through a similar series of conditioners and measurement devices. First the air streams pass

through honeycomb flow straighteners shown in Figure 4.3. The straighteners help eliminate large scale vortices in the airflow which would cause errors in the orifice plate pressure drop measurements.

Figure 4.3. Photograph of the honeycomb flow straighteners placed before all of the orifice plates in the energy exchanger test facility (Erb, 2007).

After the straightener the airflows pass through 38 mm throat diameter orifice plates designed and machined in accordance with ISO Standard 5167-1. Each orifice plate creates pressure drops proportional to the flow rate. The pressure drops are measured using pressure transducers calibrated from 0 to 1244 Pa (0 to 5 in. H_20) (as shown in Appendix C). The pressure drops are converted to mass flow rates using equation (4.1) (Erb, 2007). Evaluating equation (4.1), for a pressure drop of 1244 Pa (5 in. H_20), equates to a maximum measureable flow rate of 0.048±0.006 kg/s (≈37±8 L/s = 260±56 ft/min face velocity). The uncertainty in the air flow rate is calculated as shown in Appendix C.3.

$$q = C_d \frac{\pi}{4} D_2^2 \left[\frac{2(248.8429)\Delta P}{\rho(1-d^4)} \right]^{\frac{1}{2}} \tag{4.1}$$

where, q = the air flow rate [m^3/s],

C_d = the discharge coefficient [Approx. 0.61],

D_2 = the orifice plate diameter [0.038 m ± 0.0001 m],

d = the ratio $D_2 / D_1 = 0.038 / 0.0508 = 0.748 \pm 0.002$ [m/m],

D_1 = the pipe diameter [0.0508±0.0001 m],

ΔP = the pressure drop measured across the orifice [in. H_2O],

ρ = the density of the air [kg/m^3].

Sufficiently downstream from the orifice plates, the air streams pass through flow mixers. The mixers help to eliminate any non-uniform spatial distributions in temperature and relative humidity across the piping. After each mixer, the air streams pass over a Vaisala temperature/relative humidity probe. Each probe outputs two voltages, one being proportional to the temperature and the other being proportional to the relative humidity. The calibration precision uncertainty in the temperature/relative humidity probes and orifice plate pressure transducer measurements, determined as shown in Appendix C and Appendix D respectively, are listed in Table 4.2.

Table 4.2. Calibration precision uncertainty of the four temperature/relative humidity probes and the orifice plate pressure transducers used to determine the air mass flow rate.

Supply Inlet	Supply Outlet	Exhaust Inlet	Exhaust Outlet
0.30 (°C)	0.25 (°C)	0.27 (°C)	0.26 (°C)
0.8 %RH	1.0 % RH	1.0 % RH	0.7 % RH
0.037 in. H_2O	0.002 in. H_2O	0.001 in. H_2O	0.002 in. H_2O

The last measurement taken before the air enters the supply and exhaust exchangers (and the first taken upon exiting) are temperatures. Three thermocouples are spaced equally along the height of the exchanger, as shown in Figure 4.4, to obtain mean

inlet and outlet air temperatures. The average of these three thermocouples is used to reduce the uncertainty of the temperature measurement.

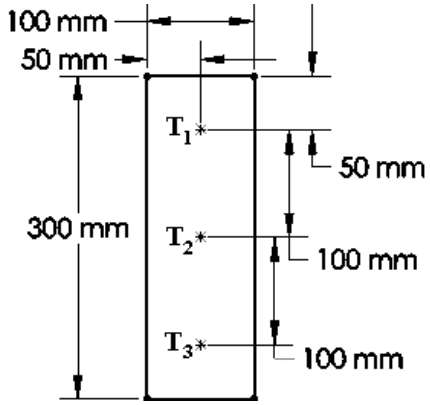

Figure 4.4. Positioning of the three thermocouples used to obtain a mean temperature measurement at the inlet and outlet of both the supply and exhaust exchangers.

Once the air streams enter the exchangers, the temperature change in the air streams is measured along the length of the exchangers. Four thermocouples are in the middle air stream channel of both exchangers and positioned as shown in Figure 4.5.

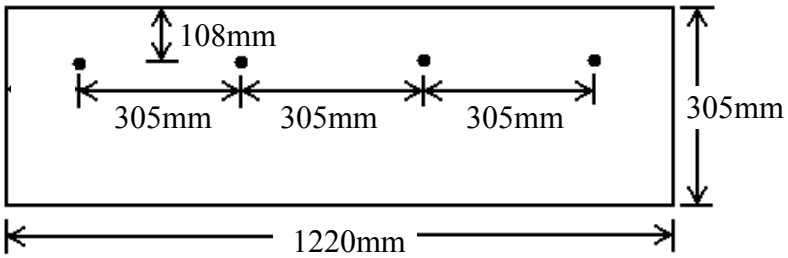

Figure 4.5. Positioning of the thermocouples placed in the middle air streams within the exchangers to measure the temperature profile through length of the exchangers.

All thermocouples were calibrated before installation in the exchangers as detailed in Appendix D.2. The calibration precision uncertainty for the thermocouples was determined to be ±0.2°C yielding the mean air temperatures uncertainty to be ±0.1°C.

4.1.3 The Desiccant Side of the Energy Exchanger Test Facility

For RAMEE Prototype 4, the desiccant used as the transfer medium was an aqueous salt solution of magnesium chloride. As detailed in Figure 4.2, the desiccant outlet of both exchanger are connected to reservoirs. The reservoirs store excess desiccant when the system is idol and prevents air from being drawn into the pumps. The reservoirs feed two Finish Thompson Incorporated (FTI) KC3 Magnetic Sealless 1/8 hp (70 W) pumps which provide the desiccant flow through the exchangers. There are valves located between the pumps and the exchangers to control the flow rate and an inline flow measurement device to monitor the flow.

Originally two Dwyer variable area flow meters (rotometers) were used to measure the desiccant flow rate. The accuracy and smallest measurable flow rate of these meters was limited to 0.2 GPM (0.8 l/min) which limited the lower range testing capabilities. Since the flow rate measurement would vary during each test this required continuous monitoring and adjustment to the flow rate. To test at lower flow rates and simplify the testing procedure the rotometers were replaced with electronic flow meters and electronically actuated flow controllers were added.

Omega FMG 220 Low Flow Magnetic Flow Meters are used to measure the flow rate of desiccant with a calibration precision uncertainty of 0.3 l/min as shown in Appendix D. The desired flow rate is obtained using electronically actuated Belimo B3 Series Characterized Control Valves. Using the flow meter measurements the position of the flow valve can be continuously adjusted to attenuate to the desired flow rate. A photograph of the flow meters and flow valves is presented in Figure 4.6.

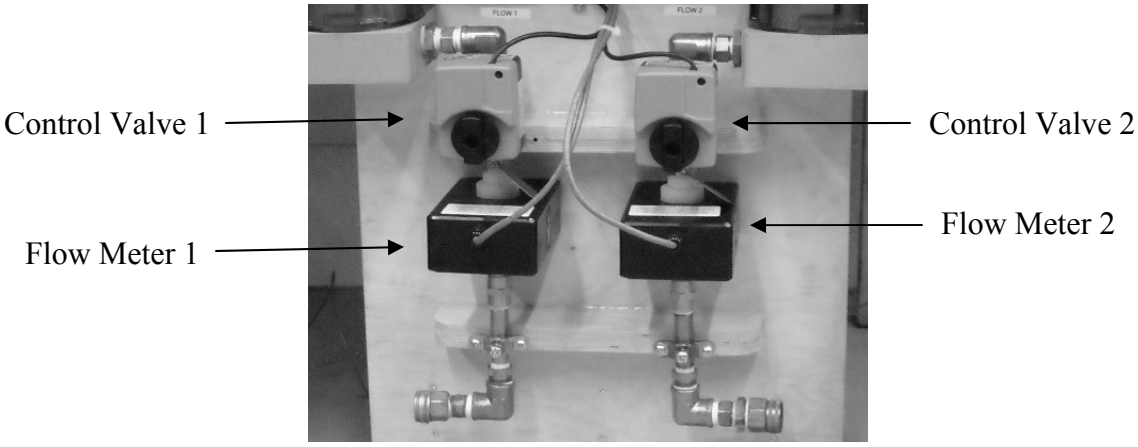

Figure 4.6. Photograph of the desiccant electrical flow meters and electronically actuated flow control valves.

The desiccant temperature and salt concentration changes through the exchangers are of interest. Thermocouple wells, shown in Figure 4.47(a), are installed in both the supply and exhaust exchangers inlet and outlet headers (locations 5-8 of Figure 4.2). There are also sampling ports placed in the desiccant lines for removing samples of the desiccant before/after the headers as shown in Figure 4.7 (b). Using the sampling ports, a sample of approximately 5 ml of desiccant can be removed with a hypodermic needle and syringe. The samples are injected into a densitometer with a measurement accuracy of ±0.00001 g/cm^3. The density measurements are used to determine the salt concentrations and convert the desiccant volume flow rate to a mass flow rate. The densitometer is routinely calibrated by obtaining a density measurement for HPLC (0.99822 g/cm^3).

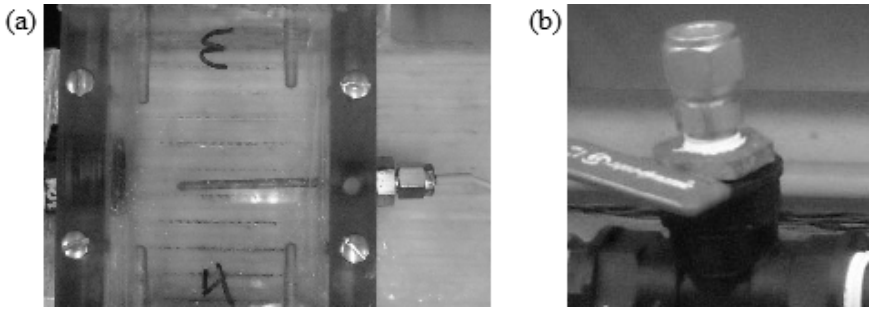

Figure 4.7. Photographs of a (a) thermocouple well installed in an exchanger header and (b) desiccant sampling port.

4.2 RAMEE Prototype 4

To interpret the energy exchanger test results an understanding of the RAMEE Prototype 4 construction and operation is required. The construction drawings for RAMEE Prototype 4 are given in Appendix E with material specifications given in Appendix F. Each of the RAMEE exchangers contains ten panels (all the same), totaling twenty panels. Each of the panels used two 1270 mm x 381mm (50" x 15") pieces of membrane, two outer screens, one inner screen, four air spacers, six desiccant spacers, and two pieces of corrugated plastic. The air spacers create a 6.35 mm (¼") air gap between adjacent panels and the desiccant spacers create a 3.175 mm (1/8") solution flow gap. A section view of the top portion of one panel is shown in Figure 4.8.

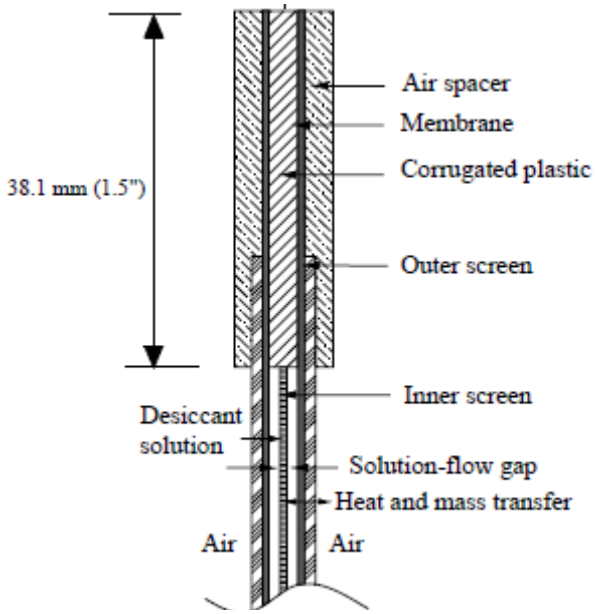

Figure 4.8. Detail of the components used to construct the RAMEE modules (Mahmud, 2009).

To construct the 20 panels required for RAMEE Prototype 4, 40 sheets of the AY Tech. ePTFE Laminate membrane were cut and punched as shown in Figure 4.9. The

desiccant spacers, corrugated plastic, and the inner screen are glued between two of these membranes forming the desiccant flow path.

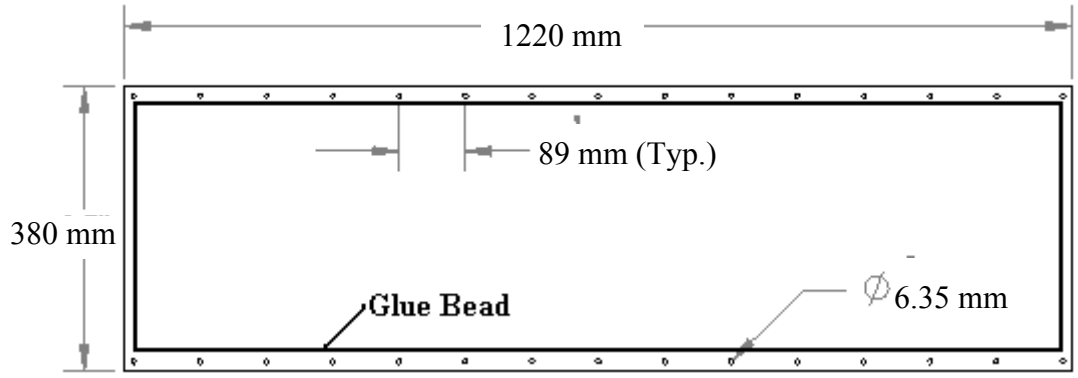

Figure 4.9. AY Tech. ePTFE Laminate cut to length and width with the bolt holes drilled.

The components which form the desiccant flow path are configured as shown in Figure 4.10. With some additional glue in the corners of the panels, a seal is formed around the perimeter containing the desiccant between the two layers of membrane. However, the corrugated plastic board allows the desiccant to flow in and out of the envelopes. The desiccant flows in through the bottom piece of corrugated plastic, through/around the heavy felt, and out of the envelopes via the top piece of corrugated plastic.

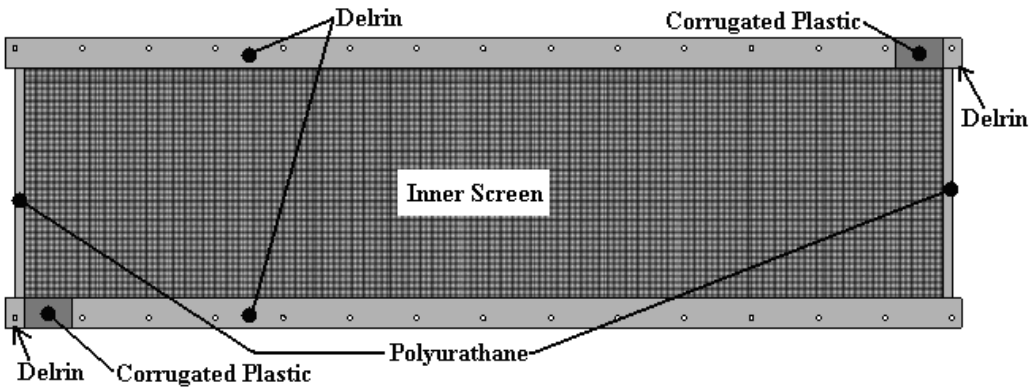

Figure 4.10. The positioning of the components glued between two sheets of membrane to form the desiccant flow path.

A total of four air side spacers are glued to the desiccant envelopes, two on the top (as shown in Figure 4.8) and two on the bottom. The spacers also hold two outer screen pieces (one on each side) against the membrane to reduce bulk deflections into the air stream. Once all of the panels were constructed they were tested for leaks using the pressure testing apparatus shown in Appendix G. Pieces of C-channel extruded plastic were glued to the leading and trailing edge of all envelopes to reduce leakage at these sites. All other small leakage sites were sealed and envelopes with large issues were discarded.

Using the assembled panels and assembling the remaining exchanger components, as detailed in Appendix E, the exchangers shown in Figure 4.11 were constructed. All mating surfaces in the headers and between the panels, which are exposed to desiccant, were glued to help eliminate leakage. Furthermore, the finished exchangers, shown in Figure 4.11, were leakage tested prior to insulating with spray foam. The air side gap along the height was ensured by placing three horizontally aligned pieces of 3.125 mm (1/8") diameter acrylic rods between each of the panels and the sidewalls totaling 33 rods per exchanger.

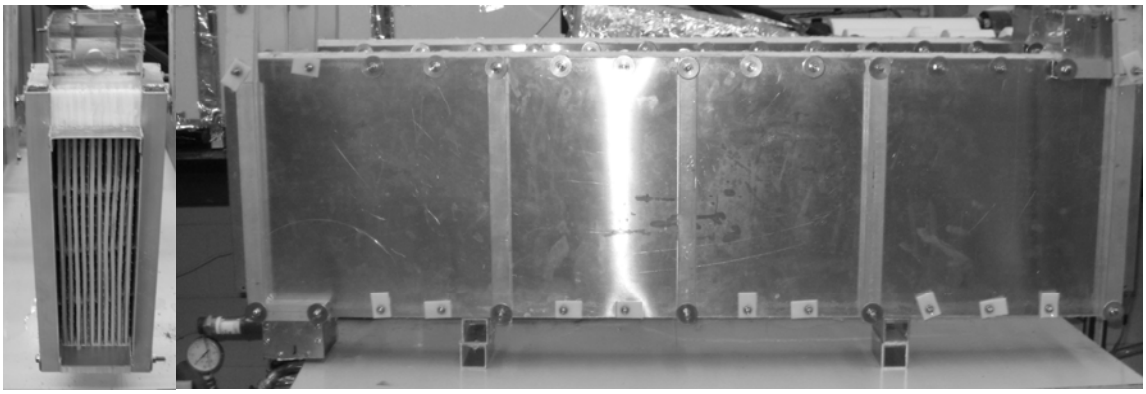

Figure 4.11. End and side views of an assembled exchanger used in the RAMEE Prototype 4.

4.3 Results and Discussion from the RAMEE Laboratory Testing

The results presented in this section were collected using data acquisition software (Labview). The desiccant flow control results are presented followed by air stream temperature changes observed through the exchangers during testing. The performance at AHRI summer test conditions are presented finishing with peak effectiveness results.

4.3.1 Desiccant Flow Control

With the addition of the flow control valve and the flow meter a control strategy needed to be developed to attenuate to the desired flow. It was decided to use a proportional feedback control strategy as shown in the schematic presented in Figure 4.12. The input to the control loop is the desired desiccant flow rate, or set point, and the output is the measured flow rate.

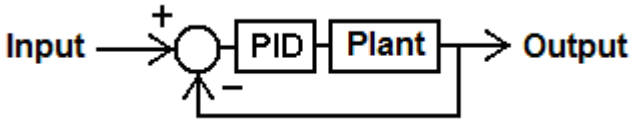

Figure 4.12. Schematic of a proportional, integral, and derivative controller used to determine a control strategy that attenuated to the desired desiccant flow rate.

Using the Ziegler-Nichols method, the coefficients for a PID controller were determined (Ellis, 1991). However, the PID control strategy equated to a long transient time with little effect on the steady state fluctuations. As such it was decided that a simple proportional controller with flow measurement feedback was sufficient for the relatively constant set-points. The response obtained with this control strategy is shown in Figure 4.13 (a) with flow rate measurements for a fixed valve position (b) (constant voltage).

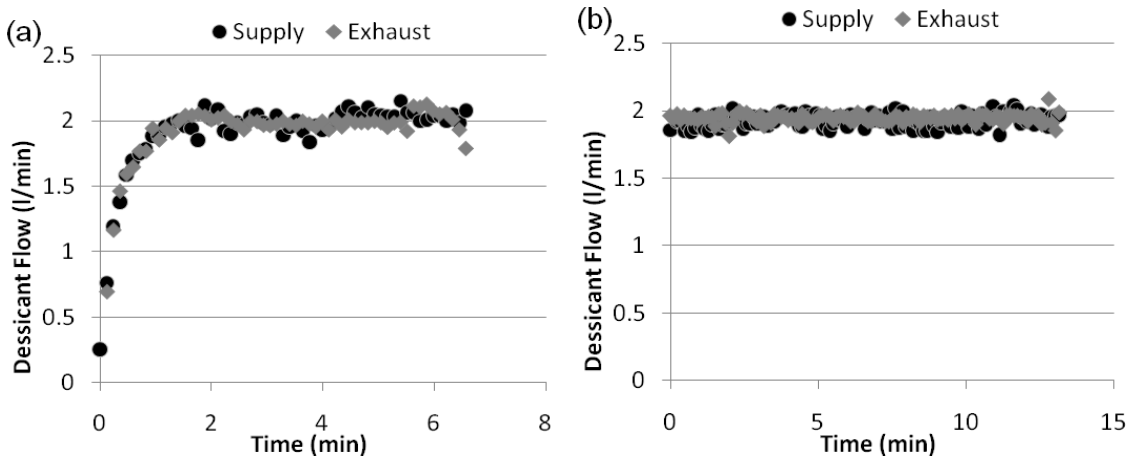

Figure 4.13. Flow results obtained using (a) a proportional control with P=0.3125 and (b) a constant valve voltage.

Using the results presented in Figure 4.13, the steady-state means were calculated for both the supply and exhaust desiccant flow rates. To quantify the steady state fluctuation, the standard deviations in the steady state responses were also calculated. The resulting means and standard deviations are presented in Table 4.3.

Table 4.3. Mean steady state desiccant flow rates of the responses presented in Figure 4.13 with the standard deviation. Note: all units are in l/min.

	Supply		**Exhaust**	
	Mean	Std Dev.	Mean	Std Dev.
P=0.3125, I=0, D=0	2.01	0.07	2.00	0.06
Constant Voltage	1.93	0.05	1.95	0.03

As seen in Table 4.3, the standard deviation for both the supply and exhaust flow rates was reduced when a constant voltage was supplied to the control valve. This would indicate that the fluctuations observed in the steady portion of Figure 4.13 (a) were slightly magnified by the proportional control. A mean flow rates (2.01 l/min for supply and 2.00 for exhaust) were obtained very close to the set point (2.0 l/min). Due to the

mean flow rates (2.01 l/min for supply and 2.00 for exhaust) were obtained very close to the set point (2.0 l/min). Due to the relatively constant nature of the testing flow rate set-point, the proportional control was deemed sufficient for maintaining set point flow rates.

4.3.2 Air Stream Temperature Change

Using the thermocouples positioned as shown in Figure 4.5, the temperature of the air streams through the exchangers were monitored. In this section, two test results are presented: one at a relatively high specific heat ratio (Cr* = 9.5, calculated as shown in Appendix A) and the other at a relatively low heat capacity ratio (Cr* = 2.5). The temperature profile results are then compared and discussed.

Specific Heat Capacity Ratio Cr* = 9.5

Once a test had reached quisi-steady state conditions (Mahmud, 2009), data acquisition continued until a large statistically significant (N>30) data set was collect to accurately determine average values (with time) for the measurements. Using these averaged values, the temperature distribution through the length of the supply and exhaust exchangers was determined. The resulting air stream temperature profiles are presented in Figure 4.14. The horizontal axis was normalized by the exchanger length such that 0 indicates the inlet and 1 indicates the outlet.

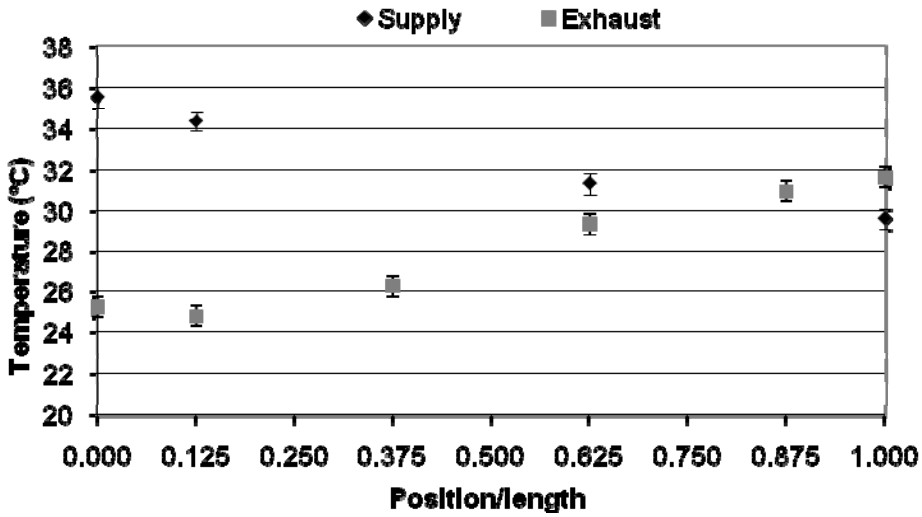

Figure 4.14. Air stream temperature profile measured through the length of the exchangers for Cr*=9.5, NTU = 12.2, V_f=106 ft/min, supply inlet of 36°C @ 44 %RH, and exhaust inlet of 25 °C @ 16 %RH.

The average humidity ratios and desiccant temperatures measured across the exchangers, for the test results presented in Figure 4.14, are presented in Table 4.4. Also shown in Table 4.4 is the absolute change measured across the exchangers (Delta).

Table 4.4. Humidity ratios of the air streams and temperatures in the desiccant measured across the exchangers.

	Supply			Exhaust		
	Inlet	Outlet	Delta	Inlet	Outlet	Delta
Humidy Ratio (g_W/kg_A)	16.4	11.6	4.8	0.6	12.0	8.4
Desiccant Temperature (°C)	27.8	29.9	2.1	31.6	27.7	9.9

As shown in Figure 4.14, the air stream was cooled through the supply exchanger and warmed through the exhaust exchanger. Also, as indicated by the humidity ratios presented in Table 4.4, the air was dried through the supply exchanger and humidified in the exhaust exchanger. The resulting effectiveness values observed during this test are presented in Figure 4.15.

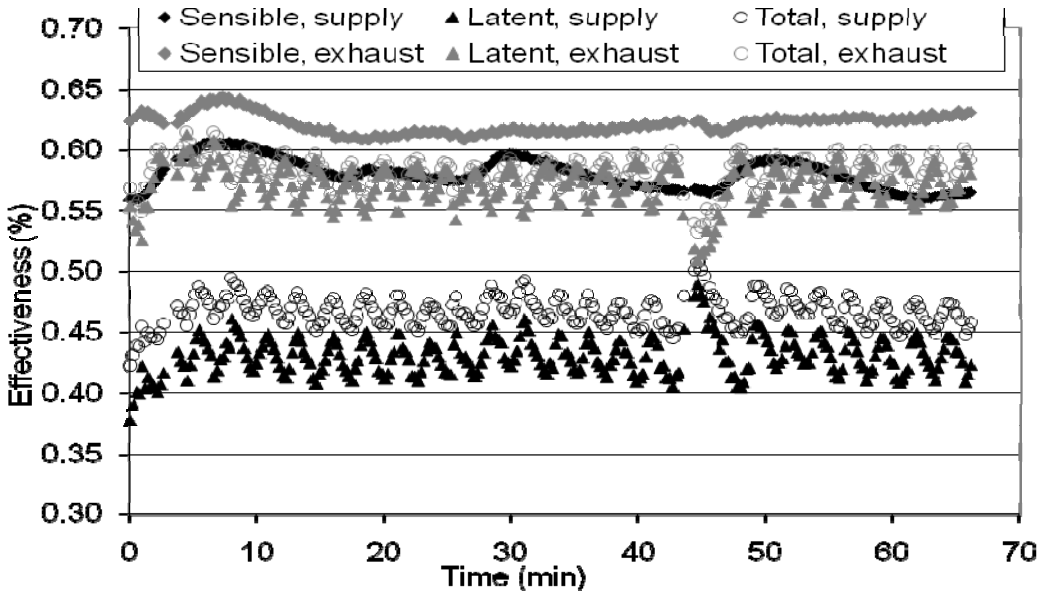

Figure 4.15. The resulting effectiveness values determined for the entire test duration at Cr*=9.5

The effectiveness values presented in Figure 4.15 show large periodic fluctuations. These fluctuations are caused by fluctuations in the supply inlet moisture content (W) created by the steam generator automatically turning on and off to maintain the environmental chamber moisture content. Using a mean of the supply inlet moisture smoothes out the effectiveness curves as presented in Figure 4.16.

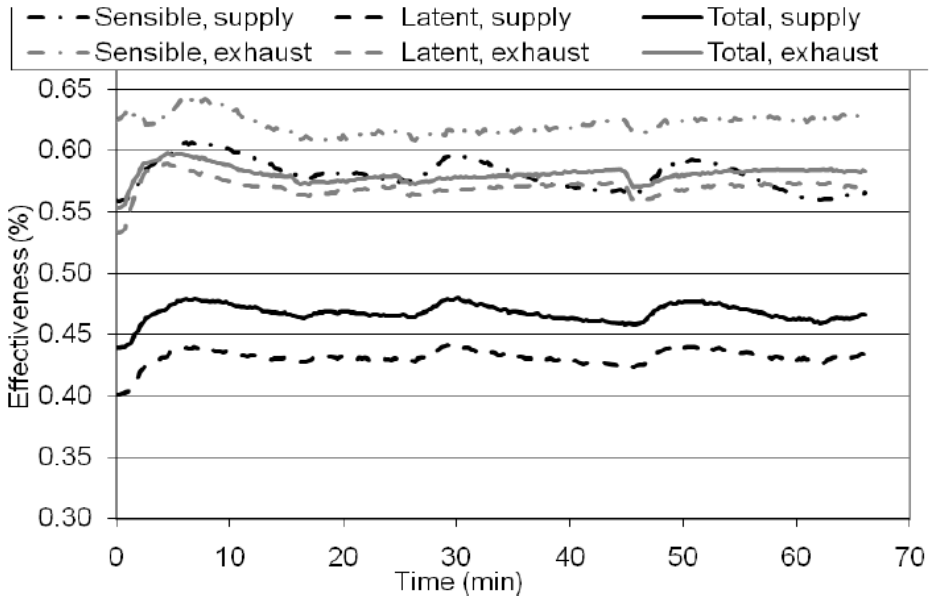

Figure 4.16. The resulting effectiveness values determined using a mean supply inlet moisture content for the Cr*=9.5 test data presented in Figure 4.15.

Specific Heat Capacity Ratio Cr* = 2.5

Similar to the higher specific heat capacity ratio test (Cr*=9.5), the temperature profiles observed through the exchangers are presented in Figure 4.17. Furthermore, the humidity ratios and desiccant temperatures measured across the exchangers are presented in Table 4.5.

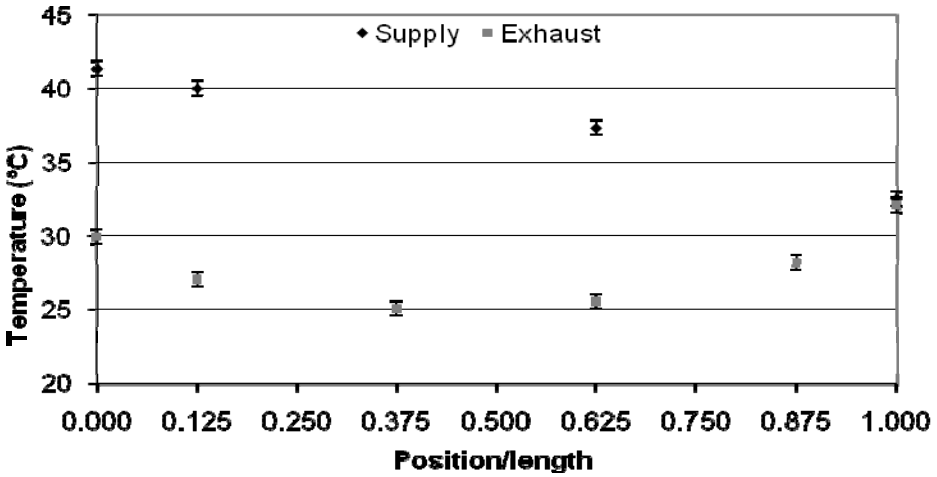

Figure 4.17. Air stream temperature profiles measured through the length of the exchangers for Cr* = 2.5, NTU = 6.3, V_f = 211 ft/min, supply inlet of 41°C @ 32 %RH, and exhaust inlet of 30°C @ 15%RH.

Table 4.5. Humidity ratio change measured in the air streams and temperature changes in the desiccant measured across the exchangers.

	Supply			Exhaust		
	Inlet	**Outlet**	**Delta**	**Inlet**	**Outlet**	**Delta**
Humidy Ratio (g_W/kg_A)	17.7	14.1	3.6	4.1	10.1	6.0
Desiccant Temperature (°C)	27.5	35.7	8.2	36.5	25.8	10.7

Figure 4.17 shows that the air stream was again cooled through the supply exchanger but unlike the higher Cr* test result, the exhaust air stream temperature drops and then rises. As presented in Table 4.5, the air was dried through the supply exchanger and humidified in the exhaust exchanger. Therefore, the direction of the sensible and latent transfer were both to the desiccant in the supply exchanger and from the desiccant in the exhaust exchanger for both of the Cr* tests. The resulting effectiveness values observed during the Cr*=2.5 test are presented in Figure 4.18.

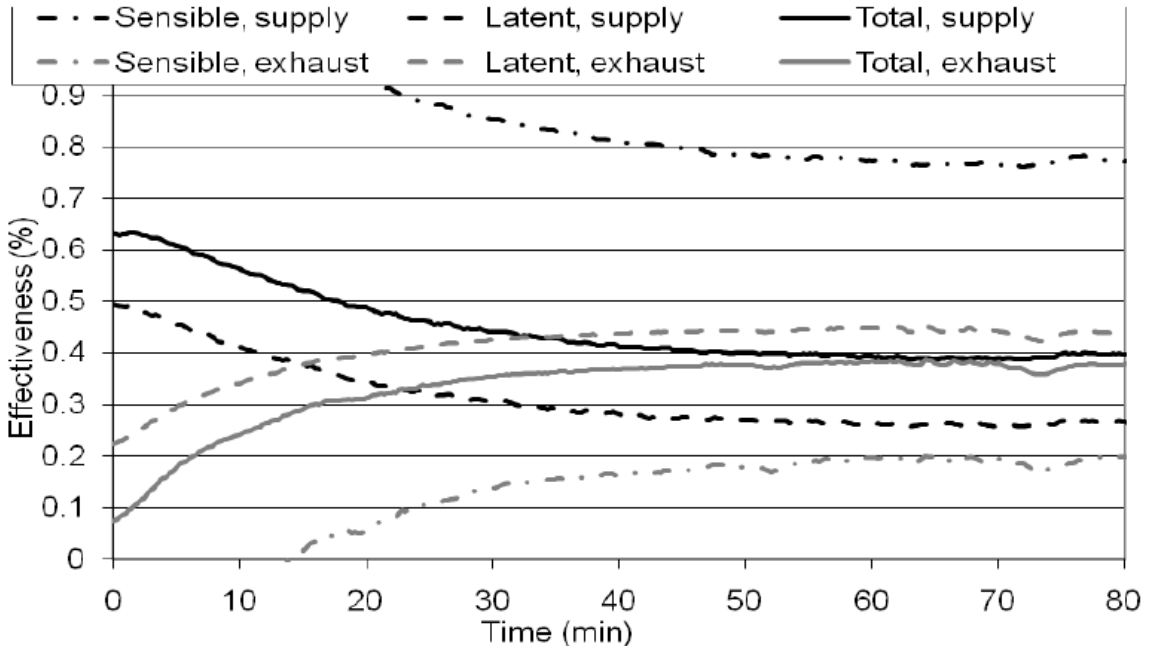

Figure 4.18. The resulting effectiveness values determined during the test conducted using the mean supply inlet moisture content for Cr* = 2.5.

Comparison of the Cr* = 9.5 to the Cr* = 2.5 Results

The results of the Cr* = 9.5 test and the Cr*=2.5 test are similar, but with one critical difference observed in the exhaust air stream temperature profiles. There is a slight drop in the exhaust air temperature at the dimensionless length of 0.125 in Figure 4.14 but for the most part it rises through the length of the exchanger. However, in Figure 4.17, the exhaust air stream temperature drops until the middle of the exchanger, where it begins to rise again. This difference is due to the differences in test conditions.

The airflow rate in the Cr*=9.5 was 0.019 kg/s which equated to V_f = 0.538 m/s (106 ft/min) while for the Cr*=2.5 test the airflow rate was 0.033kg/s equating to V_f = 1.072 m/s (211 ft/min). Presented in Tables 4.4 and 4.5, the change in exhaust humidity ratio measured were 6.0 g_W/kg_A and 8.3 g_W/kg_A respectively. This equated to a moisture transfer rate of 0.020 g_W/s and 0.016g_W/s from the desiccant to the air. The desiccant flow rates were 0.022kg/s and 0.044 kg/s respectively yielding a mass flow rate ratio of 0.9 g_W/kg_{Des} and 0.35 g_W/kg_{Des}. Thus, nearly three times the water was being evaporated from the desiccant in the exhaust exchanger during the low Cr* test. The heat of phase change for evaporating the water is taken from the desiccant causing evaporative cooling to the desiccant. Therefore, the desiccant was cooled below the inlet temperature of the air causing the initial drop in the exhaust airstream temperature (see Figure 4.17).

The total energy transfer in the exhaust exchanger of the Cr*=2.5 test was dominated by latent transfer. This equated to a latent effectiveness that was higher than the sensible effectiveness as shown in Figure 4.18. This is not typically the case but will likely occur whenever the desiccant is undergoing a large change in concentration or the test conditions are such that there is little potential between the airstreams for heat transfer and a high potential for moisture transfer.

4.3.3 AHRI Summer Effectiveness

The goal of these tests was to determine the effectiveness of RAMEE Prototype 4 over a range of heat capacity ratios (Cr*) at AHRI summer test conditions. The desiccant heat capacity, the air flow rate, and the air inlet conditions were near constant for each set of data. Thus, the ratio of heat capacities is mostly proportional to the mass flow rate of desiccant. By varying the mass flow rate of the desiccant, the effectiveness values of RAMEE prototype 4 are determined over a range of Cr*.

Test Conditions

The effectiveness value distributions with Cr* were determined at two different air flow rates with one being low and the other relatively high. The low airflow rate equated to net heat transfer units (NTU) of 12.3 and a face velocity of V_f = 0.48 m/s (88 ft/min). The high airflow rate equated to a NTU of 5.0 and a face velocity of V_f = 1.25 m/s (264 ft/min). The air inlet conditions obtained during these tests are shown on the psychometric chart in Figure 4.19 and Figure 4.20 for the low and high airflow rate tests respectively.

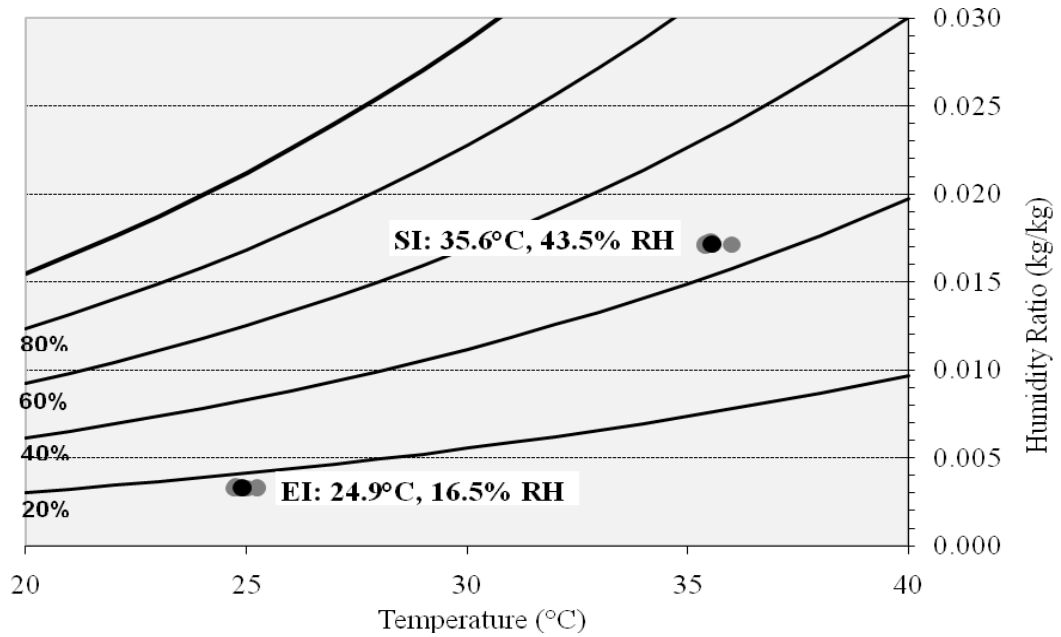

Figure 4.19. The inlet conditions obtained when evaluating the RAMEE Prototype 4 performance for NTU = 12.3, V_f = 88 ft/min (0.45 m/s). Note: The average inlet conditions are plotted in black and denoted as SI (supply inlet) and EI (exhaust inlet).

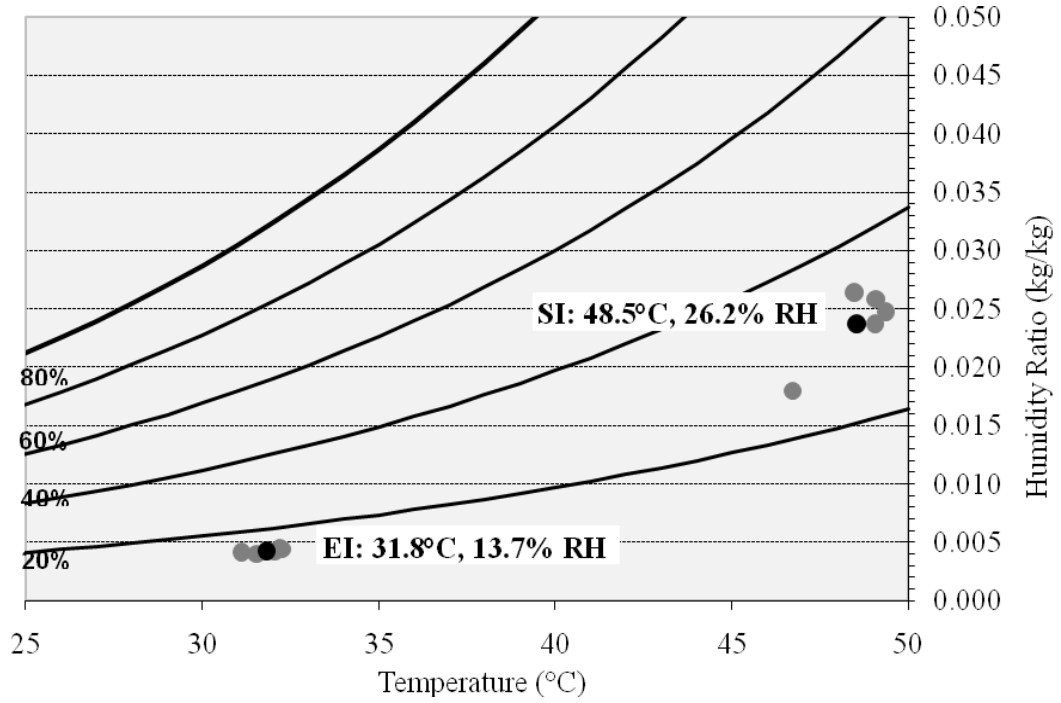

Figure 4.20. The inlet conditions obtained when evaluating the RAMEE Prototype 4 performance for NTU = 5.0 and V_f = 264 ft/min (1.34 m/s). Note: The average inlet conditions are plotted in black and denoted as SI (supply inlet) and EI (exhaust inlet).

It can be seen in Figures 4.18 and 4.19 that the inlet conditions were relatively constant for the tests but not equal to the AHRI test conditions presented in Table 4.1. For the higher airflow rate more heat was produced by the vacuums causing elevated inlet temperatures.

Average Effectiveness Values Compared to Numerical

Using the average supply and exhaust inlet conditions shown in Figures 4.19 and the exchanger specifications in Appendix F, the numerical model (Hemingson, 2010) was used to determine the effectiveness of the RAMEE prototype 4. Figures 4.21 and 4.22 present the average sensible (S), latent (L), and total (T) effectiveness values measured using the energy exchanger test facility (with uncertainty). Figure 4.21 is for the low air flow rate (NTU = 12.3) and Figure 4.22 is for the high air flow rate (NTU = 5).

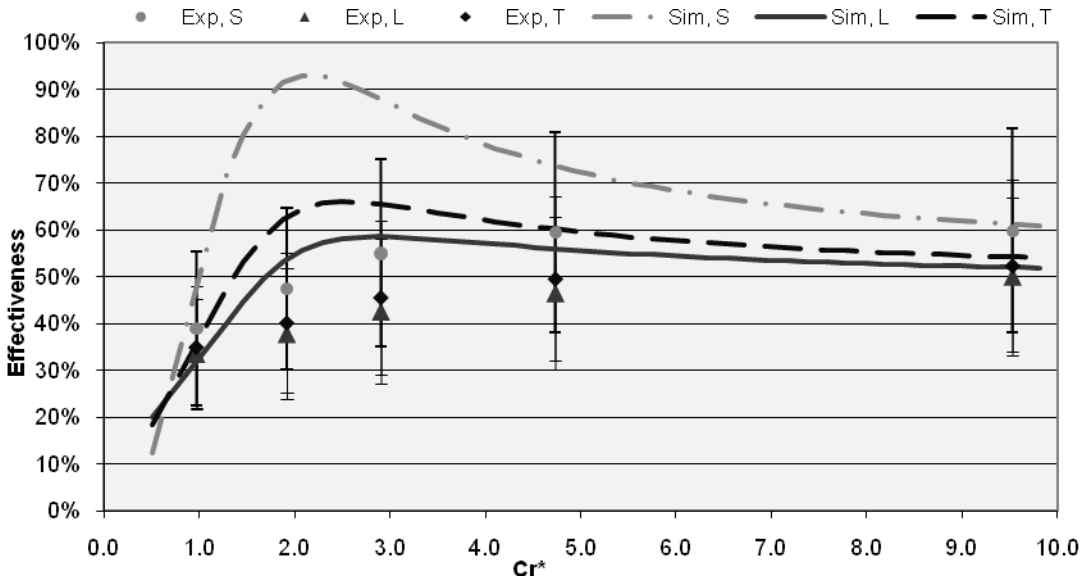

Figure 4.21. The experimentally measured RAMEE Prototype 4 effectiveness for a range of desiccant flow rates (heat capacity ratio) at NTU = 12.3, V_f = 88 ft/min (0.45 m/s). Note: the simulation results were obtained for a purely counter-flow exchanger.

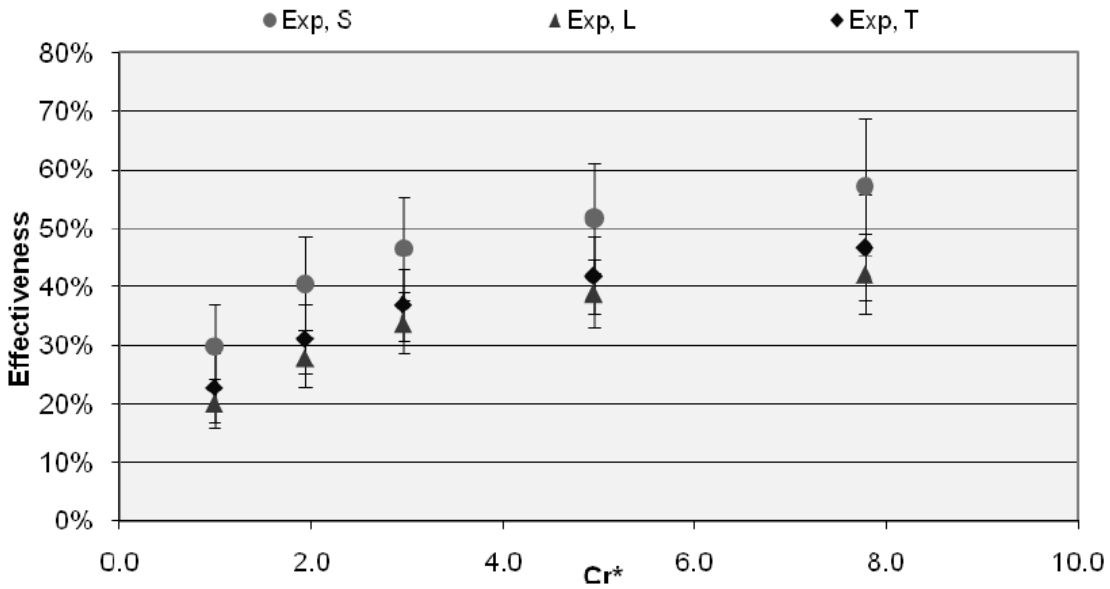

Figure 4.22. The experimentally determined RAMEE Prototype 4 effectiveness for a range of desiccant flow rates (heat capacity ratio) at NTU = 5, V_f= 264 ft/min (1.34 m/s).

As shown in Figures 4.21, agreement between the experimental results and the numerical model was obtained at high and low Cr* values. However, agreement was not obtained for the ratio of heat capacity rates between 2 and 3 where the numerical model (Hemingson, 2010) predict a peak in effectiveness. The highest total effectiveness occurred at the maximum desiccant flow rates (Cr* max) and was measured to be (52±16)% and (47±7)% for NTU=12.3 and NTU=5.0 respectively.

Comparison to Previous RAMEE Prototypes

The average total effectiveness results obtained for RAMEE prototype 2 (Erb, 2007) and prototype 3 (Mahmud, 2009) are plotted with those obtained for RAMEE Prototype 4 in Figure 4.23.

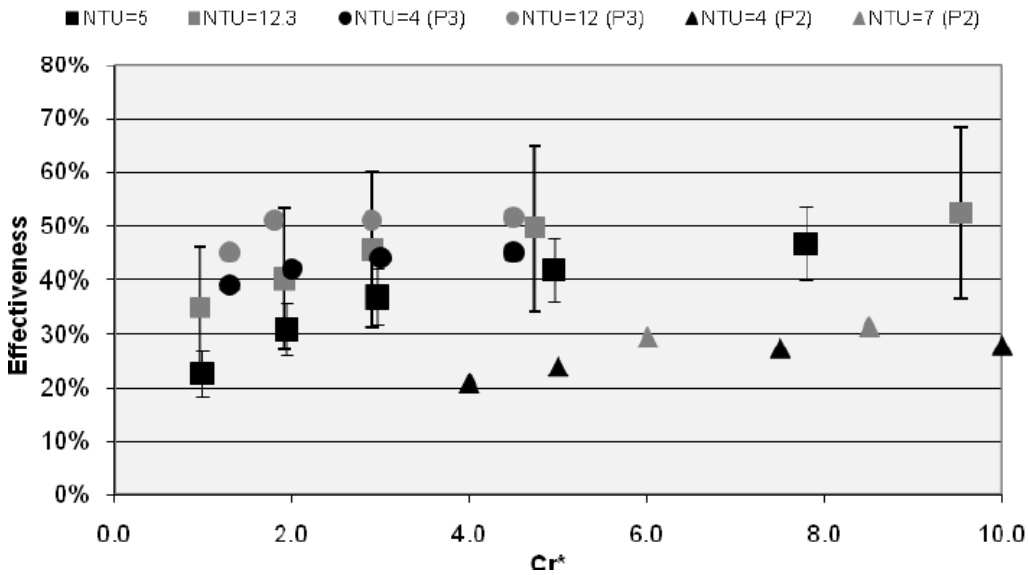

Figure 4.23. Comparison of the average total effectiveness experimentally obtained for RAMEE prototype 4 to those obtained for RAMEE prototype 2 (P2) (Erb, 2007) and RAMEE Prototype 3 (P3) (Mahmud, 2009).

As shown in Figure 4.23, the effectiveness trend obtained for prototype 3 (Mahmud, 2009) is higher than for prototype 4 which is higher than for prototype 3 (Erb, 2007). Prototype 2 (Erb, 2007) should have the lowerst effectiveness values because it was constructed in a cross-flow configuration, while prototype 3 (Mahmud, 2009) and prototype 4 used a cross-counter flow configuration. Furthermore, prototype 3 was longer and less vertical than prototype 4 at 1800 mm x 200 mm (71" x 8") vs 1220 mm x 300 mm (48" x 12") respectively. Therefore, the flow would have been closer to purely counter-flow in the prototype 3 (Mahmud, 2009) exchangers than in the prototype 4 exchangers equating to a higher effectiveness. In addition, if "dead zones" (areas where the desiccant became stagnant) existed in the corners of the exchangers, they would have been smaller in the prototype 3 exchangers than an in the prototype 4 exchangers which would result in a higher effectiveness. In addition, the "dead zones" were more likely

present in the prototype 4 exchanger due to the felt flow separator used as apposed to a screen material in prototype 3.

Also shown in Figure 4.23, all of the prototypes displayed a similar trend in effectiveness and none of the results displayed a peak in effectiveness at lower Cr* values. However, as shown in Figures 4.21, the model (Hemingson, 2010) predicted a peak effectiveness in the range of heat capacity rates between 2 and 3. Mahmud (2009) suggested many reasons for this discrepancy including flow maldistribution, heat losses and heat gains, etc. However, this is built on the assumption that the numerical model is correct and that the discrepancy is due to experimental errors. Therefore, in the section to follow, test conditions were selected such that the numerical model predicted a large peak in effectiveness to investigate the cause of this discrepancy.

4.3.4 Effectiveness Peak Test Conditions

The test conditions selected for these tests were with one airstream cool and moist and the other warm and dry. In this case the sensible and latent energy transfers are in the opposite direction through each exchanger, equating to a relatively small total heat transfer in each exchangers. The measurements were taken at one airflow rate over a range of desiccant flow rates (Cr*). It should be noted that these test conditions are not typical operating conditions for the RAMEE but were selected to investigate the cause of the discrepancy between the numerical predictions and the experimental findings. The inlet conditions obtained during the tests are presented on the psychometric chart in Figure 4.24 as well as the average inlet conditions.

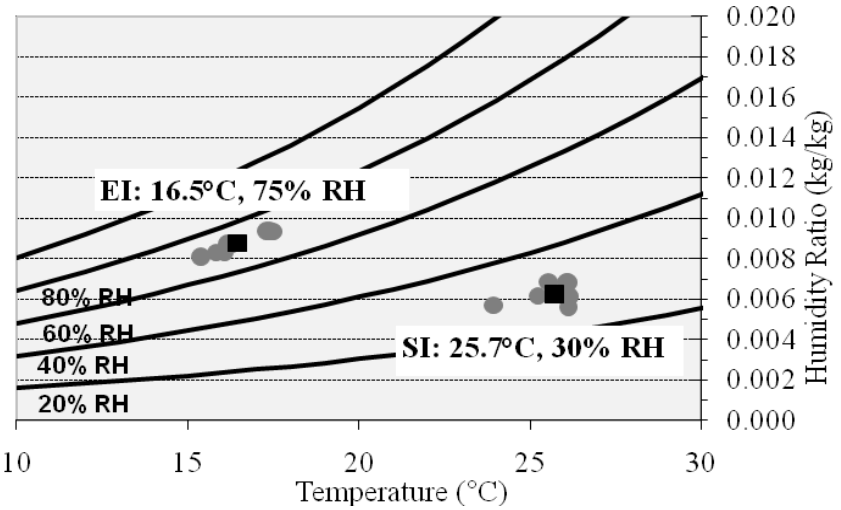

Figure 4.24 The inlet conditions obtained when evaluating the RAMEE Prototype 4 performance for NTU = 8.4, V_f = 129 ft/min (0.65 m/s). Note: The average inlet conditions are plotted in black and denoted as SI (supply inlet) and EI (exhaust inlet).

Using the average values presented in Figure 4.24, the model (Hemingson, 2010) was used to determine the expected effectiveness over a range of desiccant flow rates (heat capacity rate Cr*). The values predicted by the model are plotted with the experimental values in Figure 4.25.

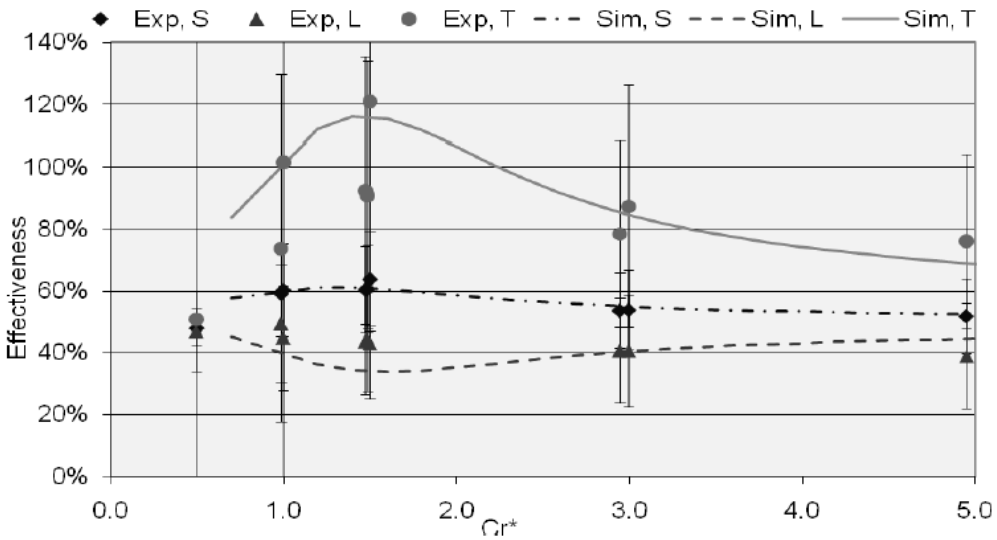

Figure 4.25. The experimentally determined effectiveness values determined for RAMEE Prototype 4 at NTU = 8.4, V_f = 129 ft/min (0.65 m/s). Note: The average inlet conditions are plotted in black and denoted as SI (supply inlet) and EI (exhaust inlet).

It can be seen in Figure 4.25 that agreement between the experimental results was obtained over the entire test range of Cr*. In addition, a peak was observed in the experimental results for both the sensible and total effectiveness. Furthermore, additional measurements were taken near the peak in effectiveness and the results were repeatable. This was the first time the peak had been observed in the experimental results. However, as previously mentioned, the total energy transfer by the exchangers was small, equating to a large uncertainty in the experimentally determined total effectiveness values.

Effect of Heat Gains

The experimental results presented in Figure 4.25 were obtained with the addition of a cooling coil placed in the desiccant lines. The purpose of this coil was to remove the heat gained by the desiccant from the pumps. To investigate the effect of adding the coiling coil, the effectiveness data obtained prior to the addition of the coiling coil is presented in Figure 4.26. An average of the effectiveness values observed with the coiling coils is presented in Figure 4.26 for comparison.

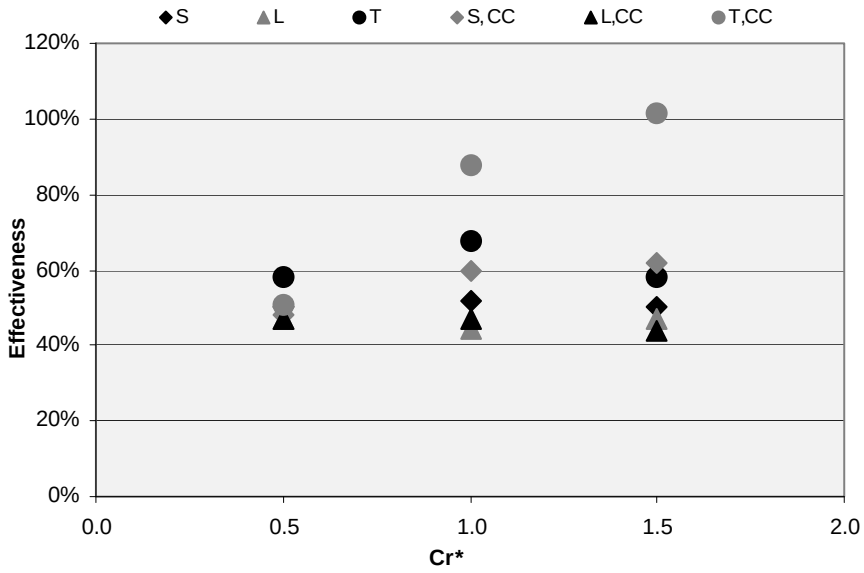

Figure 4.26. The average effectiveness values obtained prior to the installation of the cooling compared to those obtained with the addition of the coiling coil. Note: S=sensible, L=Latent, T=total, and CC= with the cooling coil.

It can bee seen in Figure 4.24 that the effectiveness data obtained prior to the installation of the cooling coil has lower sensible and total effectiveness values at Cr* = 1.0 and 1.5. Therefore, the results obtained prior to installing the cooling coils did not capture the peak in effectiveness. This suggests that heat gains/losses in the desiccant may have caused the lake of peak in effectiveness to be observed in previous tests. The location of the peak is at relatively low desiccant flow rates allowing more time for the desiccant to gain/loss heat supporting this finding. In addition, Ahmad (2008) found that the heat gains/losses eliminated the peak observed in effectiveness values predicted using his model again supporting this finding.

The individual exchanger effectiveness values are presented in Figure 4.27 and 4.28 for no cooling coil and with the cooling coil respectively. These tests were for the same air and desiccant flow rates equating to a Cr* = 1.5 and NTU = 8.5.

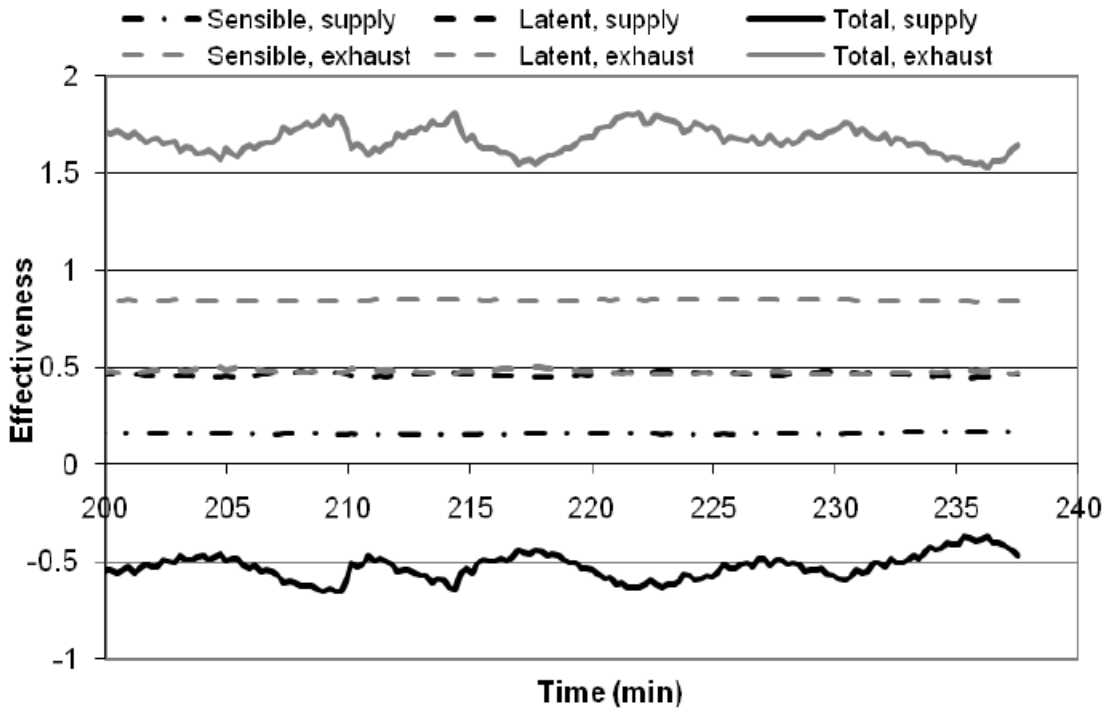

Figure 4.27. Individual exchanger effectiveness with no cooling coil at Cr*=1.5 and NTU=8.5.

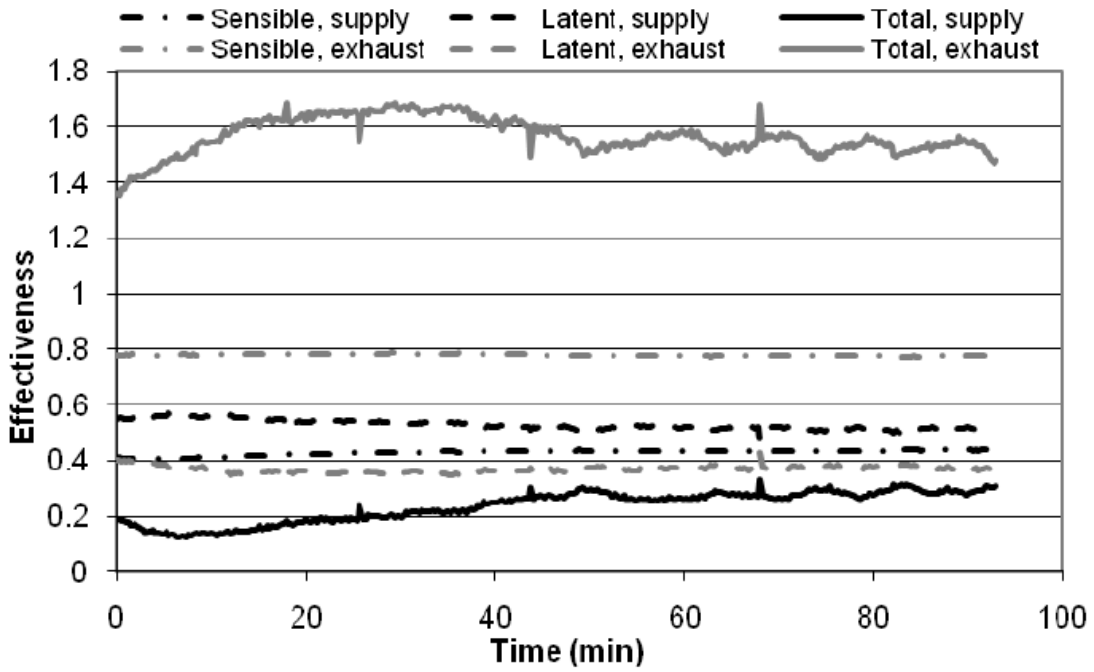

Figure 4.28. Individual exchanger effectiveness with the cooling coils installed at Cr*=1.5 and NTU=8.5.

As shown in Figure 4.27, the difference in supply and exhaust effectiveness values, prior to the addition of the cooling coils, was approximately 70% for sensible, 2% for latent, and 225% for total. As shown in Figure 4.28, the difference in supply and exhaust effectiveness values, with the cooling coils, was approximately 35% for sensible, 14% for latent, and 125% for total. Therefore, the addition of the cooling coils substantially reduced the difference between the supply and exhaust exchanger sensible and total effectiveness. However, the increase in the difference in latent effectiveness with the coiling coils is due to the desiccant concentration being out of equilibrium and not the addition of the coiling coils.

4.4 Conclusions from RAMEE Laboratory Testing

A counter-cross flow RAMEE was constructed using AY Tech. ePTFE laminate membrane with a height of 305 mm (12”) and a length of 1220 mm (4’). This RAMEE

prototype 4 was tested in the energy exchanger test facility. Electronically actuated flow controllers and electric flow meters were added to the energy exchanger test facility to replace the previously used rotometers. Based on flow measurements, it was decided that only a proportional controller was necessary to attenuate the control valve and obtain the desired flow rate.

Temperature measurements were taken in the air streams through the length of the exchangers. Typically one airstream would cool through the length of the exchanger while the other warmed. However, in one case the exhaust airstream was cooled in the first half of the exchanger and warmed in the second half. It was determined that the latent transfer was dominating the total energy transfer in the exhaust exchanger due to a large amount of water evaporating from the desiccant. The desiccant was cooled below the inlet temperature of the airstream, creating the initial drop observed in the airstream temperature. Likely, whenever the latent energy transfer dominates the total energy transfer in the exchanger the potential for a rise then drop or drop then rise in airstream temperature exists. Furthermore, these conditions are likely to occur when the supply and exhaust inlet conditions are close in temperature and not in relative humidity or the desiccant is not at the equilibrium concentration for the operating conditions.

The effectiveness at AHRI test conditions was measured at two airflow rates over a range of desiccant flow rates (Cr*). The results agreed well with the numerical model (Hemingson, 2010) at high and low desiccant flow rates but did not agree well in the range $2<Cr^*<3$. The average effectiveness trends agreed well with the previous findings for RAMEE prototype 2 (Erb, 2007) and RAMEE prototype (Mahmud, 2009). Furthermore, prototype 2 (Mahmud) had higher experimentally determined effectiveness

values because it was longer with less height equating to a closer to strictly counter-flow configuration. Prototype 2 had lower effectiveness values because it was constructed with a strictly cross-flow configuration.

RAMEE Prototype 4 was tested at conditions selected to determine the cause of the discrepancy between the experimental effectiveness values and those predicted by the model (Hemingson, 2010). A peak in effectiveness was observed by adding cooling coils to the desiccant lined in the energy exchanger test apparatus. This suggested that heat gains were the cause of the lack of peak observed in previous exchanger performance measurements. Furthermore, the addition of the cooling coils reduced the difference between the supply and exhaust effectiveness values.

The conservation of dry air, water vapour, and energy was observed for all of the RAMEE prototype 4 effectiveness tests excluding the Cr*=1 data point for the no coiling coils results of Figure 2.26. However, conformance to ASHRAE Standard 84 could not be claimed for any of the RAMEE prototype 4 tests presented due to the exhaust and supply effectiveness values not agreeing within experimental uncertainty.

CHAPTER 5

SUMMARY, CONCLUSIONS, AND RECOMMENDATIONS

5.1 Summary

To maintain good indoor air quality, buildings need to be ventilated with fresh outdoor air. However, the outdoor air often requires heating/cooling and humidifying/dehumidifying to obtain the desired supply air temperature and relative humidity. Conditioning the air uses energy, which can be reduced using an energy exchanger to recover the energy in the exhaust air.

There are many types of energy recovery systems including: heat/energy wheels, flat plate heat/energy exchangers, glycol run-around heat exchangers, and the twin tower enthalpy loop. The twin-tower enthalpy loop utilizes a liquid desiccant to transfer both heat and moisture between non-adjacent ducts using an open loop configuration. One problem with the open loop configuration is that the desiccant can become entrained in the airstreams and deposited on downstream mechanical equipment causing corrosion. The run-around membrane energy exchanger (RAMEE) is a novel design that utilizes a membrane to enclose the desiccant and prevent it from transferring to the air stream. The RAMEE has been the topic of several recent Masters theses at the University of Saskatchewan and this thesis was a continuation of this collaborative research between Venmar CES Inc. and the University.

The membrane used in the previous RAMEE prototypes, Propore™, was discontinued. Therefore in this research, replacement membrane alternatives were

obtained and evaluated based on the vapour diffusion resistance (VDR), liquid penetration pressure (LPP), modulus of elasticity (E), and price.

5.1.1 Vapour Diffusion Resistance (VDR)

The Permatran-W® 101k test apparatus, designed by Mocon based on the modified inverted cup test, was used to measure the VDR of the membrane alternatives. The goal of the VDR measurements was to find a replacement membrane with a lower VDR than the previously used Propore™. A wide range of VDRs were obtained due to a large variation in the membrane properties such as thickness, porosity, and pore size. Most importantly, some of the membranes had a lower VDR than the previously used Propore™ membrane, which if selected, would increase the moisture recovery capabilities of the RAMEE.

The VDR measured for Propore™ and Tyvek® in the Permatran-W® were higher than those presented by Larson (2006), which were obtained using the dynamic moisture permeation cell (DMPC) test apparatus of Gibson (2000). The cause of this discrepancy was investigated. The Permatran-W® utilizes a guard film that is not presented in the DMPC apparatus but this was eliminated as the cause of the discrepancy. The effects of nitrogen leakage during the Permatran-W® measurements were also investigated but again were eliminated as the cause of the discrepancy. Using an area correction, agreement was obtained between the Permatran-W® and DMPC results. The need for this correction was attributed to the boundary layer distribution in the nitrogen stream used as the moisture sink in the Permatran-W® test cell.

5.1.2 Liquid Penetration Pressure and Modulus of Elasticity

The liquid penetration pressure (LPP) and modulus of elasticity for each of the membrane alternatives were measured using a bulge test apparatus. The goal was to find

a membrane that did not leak below 5 psi (34 kPa) and that exceeded the modulus of elasticity of Propore™ (17 MPa). The AATCC test method 127 (2003) was used to measure the membrane LPP and the secant method was used to convert stress strain measurements to modulus' of elasticity. Some of the LPP measurements agreed well with previous studies and manufacturer specified values while others did not. The cause of the discrepancy was attributed to the pressurization rate used to conduct the tests. The modulus results agreed well with those obtained by Larson (2006).

5.1.3 RAMEE Prototype 4

Based on the VDR, LPP, and modulus results, the AY Tech. ePTFE Laminate was selected to replace Propore™ despite the cost being higher than the target cost of $\$0.25/ft^2$ set by Venmar CES. The AY Tech. membrane had an area corrected VDR of 97 ± 11 s/m, a LPP that exceeded the maximum test pressure of 12 Psi (82 kPa), a 387 ± 32 MPa, and a cost of $\$3.27/ft^2$. Using the AY Tech membrane RAMEE prototype 4 was build for laboratory evaluation. Similar to prototype 3, prototype 4 utilized a cross-counter flow configuration. The exchangers used in prototype 4 were 4' (1220 mm) long by 1' (305 mm) high by 4" (102 mm) wide.

5.1.4 RAMEE Prototype 4 Performance Evaluation

The energy exchanger test facility was used to evaluate the heat and mass transfer capabilities of prototype 4. The test facility provides conditioned airflow through both of the supply and exhaust exchangers which are coupled by liquid desiccant. The temperature, relative humidity, and flow rate of the air and the temperature and concentration of the desiccant entering and leaving each exchanger was measured to determine the heat and moisture transfer rates in the RAMEE.

Energy Exchanger Test Facility Desiccant Flow Control

Electronic output flow meters and electronically actuated flow valves were installed in the desiccant streams. Using the flow meter measurements, a proportional control strategy was devised to attenuate the control valves and achieve the desired flow rate.

Air Stream Temperature Profile

The air stream temperature profiles were monitored using thermocouples installed along the length of the exchangers. In a sensible exchanger the expected results is a increasing air stream temperature profile in one exchanger and a corresponding decreasing air stream temperature profile in the other. However, the RAMEE has sensible and latent transfer capabilities so an interesting temperature profile was observed at a supply inlet of 41°C and 32 %RH (W=17.7 g_W/kg_{DA}), and exhaust inlet of 30°C and 15%RH (W=4.1 g_W/kg_{DA}) (Cr* = 2.5, NTU = 6.3, V_f = 211 ft/min). In this test, the exhaust air stream temperature decreased to 25°C in the first half of the exchanger and then increased to an outlet temperature of 32°C. The drop and rise in the exhaust air stream temperature was attributed to the large amount of moisture evaporated out of the desiccant. The heat of evaporating the water was taken from the desiccant, cooling it to a temperature below the air inlet temperature (30°C). Therefore, the latent transfer dominated the overall energy transfer within the exchanger and caused the airstream temperature to first drop in through the length of the exchanger and then rise.

RAMEE Effectiveness Values

The effectiveness of RAMEE Prototype 4 was evaluated at AHRI summer test conditions at two airflow rates (NTU = 12.3 (V_f = 88 ft/min) and NTU = 5 (V_f= 264 ft/min)) and over a range of desiccant flow rates (Cr*). The highest total effectiveness

was experimentally measured to be 52±16% and 47±7% for NTU=12.3 and NTU=5.0 respectively. However, in both cases this maximum did not occur in the range of 2<Cr*<3 as predicted by the numerical model of Hemingson (2010). Instead, the maximum was observed at the maximum tested Cr* (9.5 and 8 respectively). This agreed with the previous experimental finding for Prototype 2 (Erb, 2007) and Prototype 3 (Mahmud, 2009).

Comparison with Numerical Data

To validate the numerical model and to add validity to the previous findings, inlet conditions were selected to produce an exaggerated peak in effectiveness. Although these test conditions caused a large uncertainty in the total effectiveness, the experimental results agreed well with those predicted by the model and showed a notable peak at Cr*~3. However, this was only after adding coiling coils to reduce the heat gained by the desiccant. Therefore, the lack of peak observed in the previous results was likely due to heat gains/losses in the system, which was also found by Ahmadi (2007).

5.2 Conclusions

The following conclusions were drawn from the work presented in this thesis.

- Based on the vapoour diffusion resistance measurements obtained using the Permatran-W®, the RAMEE performance can be improved using any of the Porex® membranes or the AY Tech. ePTFE laminate membrane as a replacement for Propore™.
- Agreement between the Permatran-W® measurements and the dynamic moisture transfer permeation cell (DMPC) was obtained using a correction factor of 0.53 to account for the distribution in the boundary layer of the nitrogen stream in the Permatran-W®.

- Based on the liquid penetration pressure and modulus of elasticity measurements, the RKW, Tredegar #2, and AY Tech. ePTFE laminate membranes are suitable replacements for Propore™.
- Agreement was obtained between the liquid penetration pressures and modulus of rigidity measurements with those presented by Larson (2006).
- The AY Tech. ePTFE Laminate membrane was sourced as the replacement for Propore™ and used to construct RAMEE prototype 4 for laboratory evaluation.
- An electronic flow meter and electronically actuated control valve were added to the energy exchanger test facility. A proportional gain control system was deemed sufficient to attenuate the desiccant to the desired flow rate.
- The temperature profile in the air stream through exchangers were measured and found to be dependent on the relative magnitude of the sensible and latent transfers. When the latent transfer was much larger than the sensible transfer and initial drop then rise in the airstream temperature was observed.
- The measured effectiveness values for RAMEE prototype 4 agreed well with those predicted by the numerical model (Hemingson, 2010) at high and low desiccant flow rates (Cr*) but not for mid range flow rates ($2< Cr^*<4$) at AHRI test conditions.
- The measured effectiveness values for RAMEE prototype 4 showed a similar trend to those obtained for prototype 2 and prototype 3.
- The measured effectiveness values for RAMEE prototype 4 were lower than prototype and higher than prototype 2 due to desiccant flow differences between the designs.

- The effectiveness values measured for RAMEE prototype 4 agreed with those predicted using the numerical model (Hemingson, 2010) for the mid-range desiccant flow rates with the addition of a cooling coil to remove the heat gained by the desiccant.
- The conservation of dry air, water vapour, and energy was observed for all of the RAMEE Prototype 4 effectiveness tests excluding the Cr*= 1 data point for the no coiling coil results of Figure 4.26.
- Conformance to ASHRAE Standard 84 could not be claimed for any of the RAMEE Prototype 4 tests presented in Chapter 4.

5.3 Recommendations and Future Work

The design and construction of a run-around membrane energy exchanger presented many challenges. Although great progress was made through the completion of the work presented in this thesis, there are still tasks that need to be completed. These tasks include:

- Determining the boundary layer resistance distribution in the Permatran-W® nitrogen chamber. This will require a computational fluid dynamics model to accurately determine the flow through the chamber and the local convective coefficients.
- Sourcing a membrane with a similar vapour diffusion resistance, liquid penetration pressure and mechanical properties as the AY Tech membrane, but meets the cost criteria of $\$0.25/ft^2$.

- Developing an entirely leak proof method of assembling the envelopes and exchangers. This can be accomplished by utilizing a heat sealing assembly method and injection molding a continuous piece flow seperator.

LIST OF REFERENCES

AATCC test method 127, 2003. Water resistance: Hydrostatic pressure test, American Association of Textile Chemists and Colorists, Research Triangle Park, NC.

AHRI 1060, 2005, Performance Rating of Air-to-Air Heat Exchangers for Energy Recovery Ventilation Equipment, Arlington, VA.

ANSI-ASHRAE Standard 41.1, 1986, Standard Method for Temperature Measurement, American Society of Heating, Refrigerating and Air-Conditioning Engineers Inc., Atlanta, GA.

ANSI-ASHRAE Standard 41.2, 1987, Standard Methods for Laboratory Air-flow Measurement, American Society of Heating, Refrigerating and Air-Conditioning Engineers Inc., Atlanta, GA.

ANSI-ASHRAE Standard 41.3, 1989, Method for Pressure Measurement, American Society of Heating, Refrigerating and Air-Conditioning Engineers Inc., Atlanta, GA.

ANSI-ASHRAE Standard 41.6, 1994, Standard Method for Measurement of Moist Air Properties, American Society of Heating, Refrigerating and Air-Conditioning Engineers Inc., Atlanta, GA.

ANSI-ASHRAE Standard 84, 1991, Method of Testing Heat/Energy Exchangers, American Society of Heating, Refrigerating and Air-Conditioning Engineers Inc., Atlanta, GA.

ASHRAE Fundamentals Handbook, 2005, American Society of Heating, Refrigerating and Air-Conditioning Engineers Inc., Atlanta, GA.

ASME/ANSI Performance Test Code 19.1, 1998, Test Uncertainty: Instruments and Apparatus, New York, NY.

ASME/ANSI Performance Test Code 19.2, 1987, Pressure Measurement, New York, NY.

ASME Performance Test Code 30, 1991, Air Cooled Heat Exchangers, New York, NY.

ASTM E 96-00, 2000, Standard Test Method for Water Vapour Transmission of Materials, ASTM International, West Conshohocken, PA.

ASTM F 903-03, 2004, Standard Test Method for Resistance of Materials Used in Protective Clothing to Penetration by Liquids, ASTM International, West Conshohocken, PA.

Ahmadi, M.S., 2008, Modeling the Transient Behavior of a Run-Around Heat and Moisture Exchanger System, M. Sc. Thesis, Department of Mechanical Engineering, University of Saskatchewan, SK.

Al-Ghamdi, A.S., 2006, Analysis of Air-to-Air rotary Energy Wheels, Doctorate Thesis, College of Engineering and Technology, University of Ohio, OH.

Bennett, I.J.D., 1992, The Development of a High Performance Run-Around Heat Recovery System, M. Sc. Thesis, Department of Mechanical Engineering, University of Saskatchewan, SK.

Ellis, George, 1991, Control System Design Guide, Academic Press Inc, CA.

Erb, Blake, 2007, Run Around Membrane Energy Exchanger Prototype 2 Testing, Summer Work Report, University of Saskatchewan, Saskatoon, SK.

Erb, Blake, 2009, Run Around Membrane Energy Exchanger Performance and Operational Control Strategies,M. Sc. Thesis, Department of Mechanical Engineering, University of Saskatchewan, SK.

Fan, Haisheng, 2005, Modeling a Run Around Heat and Moisture Recovery System, M. Sc. Thesis, Department of Mechanical Engineering, University of Saskatchewan, SK.

Gibson, Phillip, 1996, Multiphase Heat and Mass Transfer Through Hygroscopic Porous Media with Applications to Clothing, US Army Soldier Systems Command Natick, MA.

Gibson, Phillip, 2000, Effect of temperature on water vapor transport through polymer membrane laminates, Journal of Polymer Testing, Vol. 19, 673-691.

Gommed, K., Grossman, G., 2007, Experimental investigation of a liquid desiccant system for solar cooling and dehumidification, Journal of Solar Energy, Vol. 18, 131-138.

Hemingson, H., 2005. Preliminary Testing for Run Around Heat and Moisture Exchanger, Summer Work Report, Department of Mechanical Engineering, University of Saskatchewan, SK.

Johnson, A.B., Besant, R.W., and Schoenau, G.J., 1995, ASHRAE Transactions 104 (1B), Design of Multi-Coil Run-Around Heat Exchanger Systems for Ventilation Air Heating and Cooling , American Society of Heating, Refrigerating and Air-Conditioning Engineers Inc., Atlanta, GA, 967-978.

Johnson, A.B., Besant, R.W., and Simonson, C.J., 1998, Uncertainty Analysis in Testing Air-to-Air Heat/Energy Exchangers Installed in Buildings, ASHRAE Trans., 104 (1B), 1639-1650.

Katejanekarn, T., Chirarattananon, S., Kumar, S., 2009, An experimental study of a solar-regenerated liquid desiccant ventilation pre-conditioning system, Solar Energy, Vol. 83, 920-933.

Kaviany, M., 1995, Principles of Heat Transfer in Porous Media, Springer-Verlag, NY.

Krause, M., Saman, W. Heinzen, R., Jordan, U., Halawa, E., Vajen, K., 2007, Validation and Comparison of Absorber and Regenerator Models for Liquid Desiccant Air Conditioning Systems, Institute of Thermal Engineering, Kassel University, Germany.

Larson, M. D., 2006, The Performance of Membranes in a Newly Proposed Run Around Heat and Moisture Exchanger, M. Sc. Thesis, Department of Mechanical Engineering, University of Saskatchewan, SK.

Larson, M.D., Simonson, C.J., Besant, R. W., Gibson, P.W., 2006, The elastic and moisture transfer properties of polyethylene and polypropylene membranes for use in liquid-to-air energy exchangers, Journal of Membrane Science, Vol. 302, 136-149.

Mahmud, Khizir, 2009, Design and Performance Testing of Counter-Cross-Flow RunAround Membrane Energy Exchanger System, M. Sc. Thesis, Department of Mechanical Engineering, University of Saskatchewan, SK.

Mesquita, L., Harrison, S.J., Jones, B., 2007, Feasibility of Combined Heating/Cooling Solar-Driven Liquid Desiccant Systems for Dedicated Outdoor Air Systems, Department of Mechanical and Materials Engineering, Queen's University, Kingston, ON.

Neti, S., Wolfe, E.I., 2000, Measurements of effectiveness in silica gel rotary exchanger, Journal of Applied Thermal Engineering, Vol. 20, 309-322.

Nia, F.E., Paassen, D.V., Saidi, M.H., 2006, Modeling and simulation of desiccant wheel for air conditioning, Journal of Energy and Buildings, Vol. 38, 1230-1239.

Riffat, S.B., Gan, G., 1997, Determination of Effectiveness of Heat-pipe Heat Recovery for Naturally-Ventilated Buildings, Journal of Applied Thermal Engineering, Vol. 18, 121-130.

Saman, W., Halawa, E., Krause, M., 2007, Residential Application of Solar Liquid Desiccant Cooling System in Tropical Countries of South East Asia, Sustainable Energy Centre, University of South Australia, Mawson Lakes, SA.

Small, M.K, Nix, W.D., 1992, *Analysis of the Accuracy of the Bulge Test in Determining the Mechanical Properties of Thin Films*, Journal of Material Research, Vol. 7, 155-1563

Simonson, C.J., Ciepliski, D.L., and Besant R.W., 1999, ASHRAE Transactions 105 (1), Determining the Performance of Energy Wheels: Part I - Experimental and Numerical Methods, American Society of Heating, Refrigerating and Air-Conditioning Engineers Inc., Atlanta, GA, 174-187.

Simonson, C.J., Ciepliski, D.L., and Besant R.W., 1999, ASHRAE Transactions 105 (1), Determining the Performance of Energy Wheels: Part II - Experimental Data and Numerical Evaluation, American Society of Heating, Refrigerating and Air-Conditioning Engineers Inc., Atlanta, GA, 188-205.

Skiepko, T., Shah, R.K., 2004, A comparison of rotary regenerator theory and experimental results for and air preheater for thermal power plant, Journal of Experimental thermal and Fluid Science, Vol. 28, 257-264.

Vali, Alireza, 2009, Modeling a Run-around Heat and Moisture Exchanger Using Two Counter/Cross Flow Exchangers, M. Sc. Thesis, Department of Mechanical Engineering, University of Saskatchewan, SK.

Wu, Z., Melnik, R.V.N., Borup, F., 2006, Model-based analysis and simulation of regenerative heat wheel, Journal of Energy and Buildings, Vol. 38, 502-514.

Zaytsev, I.D., Aseyev, G.G., 1992, Properties of Aqueous Solutions of Electrolytes, CRC Press Inc., Boca Raton, FL.

Zhang, L.Z., Jiang, Y., 1999. Heat and mass transfer in a membrane-based energy recovery ventilator, Journal of Membrane Science, Vol. 163, 29-38.

Zhang, L.Z., 2007. Heat and mass transfer in a cross-flow membrane-based enthalpy exchanger under naturally formed boundary conditions, Journal of Heat and Mass Transfer, Vol. 50, 151-162.

APPENDIX A

PROPERTIES CALCULATION AND UNCERTAINTY

There are many air properties which are required when analyzing the RAMEE performance characteristics. All of these properties are calculated from the temperature, absolute pressure, and relative humidity measurements. Therefore, how these properties were calculated and how the uncertainty in the measurements propagate into these properties is critical. Similarly, desiccant properties are also required and based on temperature and salt concentration measurements which have associated uncertainty that propagates into the calculated properties. This appendix outlines how these properties are calculated, the propagation of the measurement uncertainties into these properties, and how the uncertainty in the properties propagate into the effectiveness values. Lastly, the methods in ASHRAE std. 84 (1991), used to check for the conservation of heat and mass within the experimental uncertainties, are outlined.

A.1 AIR AND DESSICANT PROPERTY CALCULATIONS

When the airstream temperature is measured to be less than 273.15 K (0°C) the saturation vapor pressure is calculated using equation (A.1) (ASHAE, 2005).

$$P_{V,SAT} = \exp\left(\frac{C_1}{T} + C_2 + C_3 T + C_4 T^2 + C_5 T^3 + C_6 T^4 + C_7 \ln(T)\right) \qquad \text{(A.1)}$$

where, $P_{V,SAT}$ = the saturation vapor pressure [Pa],

T = the measured dry bulb temperature of the air stream [K],

C_1 = -5674.5359,

C_2 = 6.3925247,

C_3 = $-9.677843*10^{-3}$,

C_4 = $6.2215701*10^{-7}$,

C_5 = $2.0747825*10^{-9}$,

C_6 = $-9.484024*10^{-13}$,

C_7 = 4.1635019.

Also, when the airstream temperature is measured to be more than 273.15 K (0°C) the saturation vapor pressure was calculated using equation (A.2) (ASHAE, 2005).

$$P_{V,SAT} = \exp\left(\frac{C_8}{T} + C_9 + C_{10}T + C_{11}T^2 + C_{12}T^3 + C_{13}\ln(T)\right) \qquad \text{(A.2)}$$

where, C_8 = -5800.2206,

C_9 = 1.3914993,

C_{10} = $-4.864023*10^{-2}$,

C_{11} = $4.1764768*10^{-5}$,

C_{12} = $-1.4452093*10^{-8}$,

C_{13} = 6.5459673.

Using the saturation vapor pressure calculated from either equation (A.1) or (A.2) and the relative humidity measurement the partial pressure of the water vapor was calculated using equation (A.3) (ASHAE, 2005).

$$P_V = P_{V,SAT}RH \qquad \text{(A.3)}$$

where, RH = the measured relative humidity of the air expressed as a fraction,

P_V = the vapour pressure [Pa].

Using the vapour pressure calculated from equation (A.3) and the atmospheric pressure measured using a mercury manometer, equation (A.4) (ASHAE, 2005) was used to calculate the humidity ratio.

$$W = 0.62198\left(\frac{P_V}{P - P_V}\right) \tag{A.4}$$

where, W = the humidity ratio [kg_W/ kg_{DA}],

P = the measured atmospheric pressure [Pa].

To calculate the enthalpy of the air the temperature measurement, humidity ratio calculated from equation (A.4), and equation (A.5) (ASHAE, 2005) were used.

$$h = 1006T + W\left(2.501 \cdot 10^6 + 1860T\right) \tag{A.5}$$

where, h = the mixture enthalpy [J/kg_{DA}],

T = the measured dry-bulb temperature of the air [°C].

The dry air density is calculated using the ideal gas law given in equation (A.6).

$$\rho_{DA} = \frac{P}{RT} \tag{A.6}$$

where, ρ_{DA} = the dry air density [kg/m^3],

T = the measured air stream dry bulb temperature [K],

R = the dry air gas constant (287.06 J/kgK).

Also of interest when describing the operating conditions of the RAMEE are the air face velocities and the heat capacity rates. The face velocity is defined as the airstream velocity directly prior to the inlets of the exchangers. To calculate the face velocities equation (A.7) was used.

$$V_F = \frac{\dot{m}}{\rho} A \tag{A.7}$$

where, V_F = the face velocity [m/s],

$\dot{m}$ = the inlet mass flow rate [kg/s],

ρ = the inlet air stream density [kg/m^3],

A = cross sectional area of the exchanger inlet [m^2].

After calculating the face velocity in m/s the result is multiplied by 60 s/min*3.28ft/m to convert to units of ft/min.

The heat capacity rates of the air and the desiccant is of interest in order to calculate the ratio of heat capacity rates. To calculate the air heat capacity the air specific heat was first calculated using equation (C.8) (ASHAE, 2005).

$$\left(c_P\right)_A = 1006 + 1860W \tag{A.8}$$

where, $\left(c_P\right)_A$ =the heat capacity of the air [J/kgK].

W = the humidity of the air [kg/kg].

Using the heat capacity of the air calculated using equation (A.8), the air heat capacity rate can be calculated by multiplying the specific heat by the mass flow rate of air as in equation (A.10).

$$C_{AIR} = \dot{m} \cdot \left(c_P\right)_A \tag{A.9}$$

where, C_{AIR} = the heat capacity rate of the air [W/K],

$\dot{m}$ = the mass flow rate of dry air at the location of interest [kg/s].

The specific heat of the desiccant was also needed to calculate the desiccant heat capacity rate. To calculate the desiccant heat capacity equation (A.10) was used (Zaytsev, 1992).

$$\left(c_P\right)_D = 134225.4\left(\frac{T_{DES}+273.15}{100}\right)^{-6.5} + 3490\left(\frac{T_{DES}+273.15}{100}\right)^{0.14} + \\ + \frac{C_{SALT}}{100}\left(B_1 + B_2\frac{C_{SALT}}{100} + B_3 T_{DES} + B_4 T_{DES}^2\right) \tag{A.10}$$

where, $\left(c_P\right)_D$ = the heat capacity of the desiccant [J/kgK],

T_{DES} = the temperature of the desiccant at the location of interest [°C],

C_{SALT} = the salt concentration of the desiccant [wt%],

B_1 **to** B_4 = salt dependent constants.

Similar to for the air, the desiccant heat capacity rate is calculated using equation (A.12).

$$C_{DES} = \dot{m}_D \cdot \left(C_P\right)_D \tag{A.11}$$

where, C_{DES} = the heat capacity rate of the desiccant [W/K],

$\dot{m}_D$ = the mass flow rate of desiccant at the location of interest [kg/s].

The average between the inlet and outlet heat capacity rates of the air and desiccant are also required to calculate the air heat capacity rate. The average is taken between the inlet and outlet on both the supply and exhaust sides. Therefore, the general form used to calculate the averages was equation (A.12).

$$C_{AVG} = \frac{C_{in} + C_{out}}{2} \tag{A.12}$$

where, C_{AVG} = the average heat capacity rate [W/K],

C_{in} = the inlet heat capacity rate [W/K],

C_{out} = the outlet heat capacity rate [W/K].

The average air heat capacity rates and average desiccant heat capacity rates were then used to calculate the heat capacity rate ratio. To calculate the heat capacity rate ratio equation (C.13) is used.

$$C^* = \frac{C_{DES}}{C_{AVG}} \tag{A.13}$$

where, C^* = the ratio of heat capacity rates,

C_{AIR} = the average heat capacity rate of the air on either the exhaust or supply side depending on the side of interest [W/K].

A.2 UNCERTAINTY IN PROPERTIES

To determine the propagation of the measurement uncertainties into the effectiveness values the method outlined in ASME Performance Test Code 19.1 was used. Also, in ANSI-ASHRAE Standard 84 tolerances in the uncertainties are presented along with a method for checking for the conservation of mass and energy. According to ASME PTC 19.1 there are two confidence intervals which are considered when determining the uncertainty in all of the RAMEETA measurements and/or all calculated results. The uncertainties in the RAMEETA measurements are determined from the calibration measurements. The two confidence intervals considered are the 95% and the 99% confidence intervals. To calculate the 95% confidence interval uncertainty equation (A.14) (ASME/ANSI PTC 19.1, 1998) was used.

$$U_{95} = \left(B^2 + (tS)^2\right)^{1/2} \tag{A.14}$$

where, U_{95} = the 95% confidence interval measurement uncertainty,

B = the measurement bias error,

t = the t-student distribution constant (2 for N>30),

S = the precision error in the measurement.

Equation (A.15) was used to calculate the 99% confidence interval.

$$U_{99} = B + 2S \tag{A.15}$$

where, U_{99} = the 99% confidence interval measurement uncertainty.

To calculate the propagation of the measurement uncertainty into the results a root-sum-square approach was used. Using the root-sum-square approach the uncertainty in the saturation vapor pressure, calculated from equation (A.1), was calculated using equation (A.16).

$$U_{P_{V,SAT}} = P_{V,SAT}\left(\frac{-C_1}{T^2} + C_3 + 2C_4T + 3C_5T^2 + 4C_6T^3 + \frac{C_7}{T}\right)U_T \tag{A.16}$$

where, $U_{P_{V,SAT}}$ = the approximate uncertainty in the saturation vapor pressure [Pa],

U_T = the uncertainty in the temperature measurement [K].

Similarly, the uncertainty in the saturation vapor pressure calculated from equation (A.2) was calculated using equation (A.17).

$$U_{P_{V,SAT}} = P_{V,SAT}\left(\frac{-C_8}{T^2} + C_{10} + 2C_{11}T + 3C_{12}T^2 + \frac{C_{13}}{T}\right)U_T \tag{A.17}$$

The uncertainty in the partial pressure of vapor calculated using equation (A.3) was calculated using equation (A.18).

$$U_P = \left(\left(RH \cdot U_{P_{V,SAT}}\right)^2 + \left(P_{V,SAT} \cdot U_{RH}\right)^2\right)^{1/2} \tag{A.18}$$

where, U_{P_V} = the uncertainty in the partial pressure of water vapor [Pa],

U_{RH} = the uncertainty in the measured relative humidity.

The uncertainty in the humidity ratio, calculated using equation (A.4), was calculated using equation (A.19)

$$U_{P_W} = 0.62198\left(\left(\frac{P}{(P-P_W)^2}U_{P_W}\right)^2 + \left(\frac{P_W}{(P-P_W)^2}U_P\right)^2\right)^{1/2} \qquad \text{(A.19)}$$

where, U_{P_W} = the uncertainty in the partial pressure of water [Pa],

U_P = the uncertainty in the total pressure of the air and vapor mixture [Pa].

The uncertainty in the enthalpy (calculated using equation (A.5)) is approximated using equation (A.20). This is an approximation because equation (A.20) does not include the uncertainty caused by the approximation in the dry air specific enthalpy and the saturated water vapor specific enthalpy. Therefore, the actual uncertainty in the enthalpy may slightly higher than that obtained using equation (A.20).

$$U_h = \left(\left((1006T + 1860W)U_T\right)^{1/2} + \left(\left(2.501\cdot 10^6 + 1860T\right)U_W\right)^{1/2}\right)^2 \qquad \text{(A.20)}$$

where, U_T = the mixture enthalpy [J/kg$_{DA}$],

U_W = the uncertainty in the humidity ratio [kg$_W$/kg$_{DA}$].

To calculate the uncertainty in the dry air density the root-sum-square of equation (A.6) was used to obtain equation (A.21).

$$U_{\rho_{DA}} = \left(\left(\frac{U_P}{RT}\right)^2 + \left(\frac{P}{RT^2}U_T\right)^2\right)^{1/2} \qquad \text{(A.21)}$$

where, $U_{\rho_{DA}}$ = the uncertainty in the dry air density [kg/m^3],

U_P = the uncertainty in the atmospheric pressure measurement [Pa],

U_T = the uncertainty in the temperature measurement [K].

The uncertainty in the face velocity is calculated using a root-sum-square approach from equation (A.7) to obtain equation (A.22).

$$U_{V_F} = \left(\left(\frac{A}{\rho} U_{\dot{m}} \right)^2 + \left(\frac{\dot{m}}{\rho} U_A \right)^2 + \left(\frac{\dot{m} A}{\rho^2} U_\rho \right)^2 \right)^{1/2} \tag{A.22}$$

where, U_{V_F} = the uncertainty in the face velocity [m/s],

$U_{\dot{m}}$ = the uncertainty in the inlet mass flow rate [kg/s],

U_A = the uncertainty in the area for air flow before the exchanger [m^2],

U_ρ = the uncertainty in the air stream density [kg/m^3].

The uncertainty in the face area used to calculate the face velocity uncertainty is calculated using equation (A.23).

$$U_A = \left((w U_h)^2 + (h U_w)^2 \right)^{1/2} \tag{A.23}$$

where, U_A = the uncertainty in the area used to calculate the face velocity [m^2],

U_h = the uncertainty in the duct height [m],

U_w = the uncertainty in the duct width [m].

From equation (A.8) the uncertainty in the specific heat for the air was calculated using equation (A.24).

$$U_{(c_P)_A} = 1860 \cdot U_W \tag{A.24}$$

where, $U_{(c_P)_A}$ = the uncertainty of the heat capacity of the air [J/kgK],

U_W = the uncertainty in the humidity ratio of the air [kg/kg].

The uncertainty in the air heat capacity rate was calculated from equation (A.9) and using a root-sum-square approach to obtain equation (A.25).

$$U_{C_{AIR}} = \left(\left(\dot{m} U_{(c_P)_A} \right)^2 + \left((c_P)_A U_{\dot{m}} \right)^2 \right)^{1/2} \tag{A.25}$$

where, $U_{C_{AIR}}$ = the uncertainty in the heat capacity rate of the air [W/K],

$U_{\dot{m}}$ = the uncertainty in the mass flow rate of air [kg/s].

From equation (A.10) and using a root-sum-square approach the uncertainty in the desiccant heat capacity is calculated using equation (A.26).

$$U_{(c_P)_D} = \left(\begin{array}{l} \left(\left[\begin{array}{l} \dfrac{256.42}{(T_{DES} + 273.15)} - \dfrac{8.724651 \cdot 10^{18}}{(T_{DES} + 273.15)^{0.75}} \\ + \dfrac{C_{SALT}}{100} (B_3 + 2B_4 T_{DES}) \end{array} \right] U_{T_{DES}} \right)^2 \\ + \left(\dfrac{1}{100} \left(B_1 + \dfrac{B_2 C_{SALT}}{50} + B_3 T_{DES} + B_4 T_{DES}^2 \right) U_{C_{SALT}} \right)^2 \end{array} \right)^{1/2} \tag{A.26}$$

where, $U_{(c_P)_D}$ = the uncertainty in the desiccant heat capacity [J/kgK],

$U_{T_{DES}}$ = the uncertainty in the desiccant temperature [°C],

$U_{C_{SALT}}$ = the uncertainty in the desiccant salt concentration [wt%].

Using equation (A.11) and a root-sum-square approach the uncertainty in the air heat capacity rate was determined to be given by equation (A.27).

$$U_{C_{DES}} = \left(\left(\dot{m}_D U_{(c_P)_D} \right)^2 + \left((c_P)_D U_{\dot{m}_D} \right)^2 \right)^{1/2} \tag{A.27}$$

where, $U_{C_{DES}}$ = the uncertainty in the heat capacity rate of the air [W/K],

$U_{\dot{m}_D}$ = the uncertainty in the mass flow rate of desiccant [kg/s].

The uncertainty in the average heat capacity rates were determine from equation (A.12) and a root sum square approach to obtain equation (A.28).

$$U_{C_{AVG}} = \frac{\left(\left(U_{C_{in}}\right)^2 + \left(U_{C_{out}}\right)^2\right)^{1/2}}{2} \tag{A.28}$$

where, $U_{C_{AVG}}$ = the uncertainty in the average heat capacity rate [W/K],

$U_{C_{in}}$ = the uncertainty in the inlet heat capacity rate [W/K],

$U_{C_{out}}$ = the uncertainty in the outlet heat capacity rate [W/K].

Using equation (A.13) and the root-sum-square approach the uncertainty in the ratio of heat capacity rates is calculated as follows.

$$U_{C^*} = \left(\left(\frac{U_{C_{DES}}}{C_{AIR}}\right)^2 + \left(\frac{C_{DES}}{C_{AIR}^2} U_{C_{AIR}}\right)^2\right)^{1/2} \tag{A.29}$$

where, U_{C^*} = the uncertainty in the ratio of heat capacity rates.

A.3 EFFECTIVENESS AND UNCERTAINTIES

To evaluate the performance of the RAMEE nine effectiveness values are calculated. These effectiveness values are the supply air sensible, latent, and total effectiveness, the exhaust air sensible, latent, and total effectiveness, and the overall RAMEE system sensible, latent, and total effectiveness. The method used for calculating these effectiveness values is outlined in ANSI-ASHRAE Standard 84 (1991) and is similar to that used by Bennett (1992), Johnson et al (1998), and Erb (2009) to evaluate the performance of air-to-air energy exchangers. There are two mass flow rate measurements taken one on each side of the exchanger. Therefore, an average of the two measurements is taken to obtain a more accurate measurement of the mass flow rate through each

exchanger. This average is used when calculating the effectiveness values. The average, taken between the inlet and outlet mass flow rate measurements, is calculated using equation (A.30).

$$\dot{m}_{avg} = \frac{\left(\dot{m}_i + \dot{m}_o\right)}{2} \tag{A.30}$$

where, $\dot{m}_{avg}$ = the average mass flow rate [kg/s],

$\dot{m}_i$ = the inlet mass flow rate [kg/s],

$\dot{m}_o$ = the outlet mass flow rate [kg/s].

The uncertainty in the average is less than the uncertainty in the individual mass flow rates because more information is used and is given by equation (A.31).

$$U_{\dot{m}_{avg}} = \frac{\left(\left(U_{\dot{m}_i}\right)^2 + \left(U_{\dot{m}_o}\right)^2\right)^{1/2}}{2} \tag{A.31}$$

where, $U_{\dot{m}_{avg}}$ = the uncertainty in the average mass flow rate [kg/s],

$U_{\dot{m}_i}$ = the uncertainty in the inlet mass flow rate [kg/s],

$U_{\dot{m}_o}$ = the uncertainty in the outlet mass flow rate [kg/s].

To evaluate the performance of the RAMEE the supply effectiveness values were calculated. To calculate the supply effectiveness values equation (A.32) (ASHRAE std 84, 1991) was used.

$$\varepsilon = \frac{\dot{m}_s\left(X_{s,o} - X_{s,i}\right)}{\dot{m}_{\min}\left(X_{s,i} - X_{e,i}\right)} \tag{A.32}$$

where, $\dot{m}_s$ = the average mass flow rate of air measured on the supply side [kg/s],

$\dot{m}_{\min}$ = the minimum of the supply and exhaust average mass flow rates of air [kg/s],

X = T, temperature for sensible effectiveness [K],

= W, humidity ratio for latent effectiveness [kg_W/kg_{DA}],

= h, enthalpy for total effectiveness [J/kg].

Also, the subscripts are given below.

s = the supply air side of the exchanger,

e = the exhaust air side of the exchanger,

i = the inlet to the respective side of the exchanger,

o = the outlet of the respective side of the exchanger.

From equation (A.32) and using a root-sum-square approach, equation (A.33) was obtained to determine the uncertainty in the supply effectiveness values.

$$U_{\varepsilon_s} = \left(\begin{array}{l} \left(\frac{\varepsilon_s}{\dot{m}_s} U_{\dot{m}_s} \right)^2 + \left(\frac{\varepsilon_s}{\dot{m}_{\min}} U_{\dot{m}_{\min}} \right)^2 + \left(\frac{\varepsilon_s}{X_{s,i} - X_{s,o}} U_{X_{s,o}} \right)^2 \\ + \left(\frac{\varepsilon_s}{X_{s,i} - X_{e,i}} U_{X_{s,i}} \right)^2 + \left(\frac{\dot{m}_s X_{e,i}}{\dot{m}_{\min} \left(X_{s,i} - X_{e,i} \right)^2} U_{X_{e,i}} \right)^2 \end{array} \right)^{1/2} \quad \text{(A.33)}$$

where, U_{ε_s} = the uncertainty in the supply effectiveness',

$U_{\dot{m}_s}$ = the uncertainty in the supply mass flow rate [kg/s],

$U_{\dot{m}_{\min}}$ = the uncertainty in minimum mass flow rate [kg/s],

$U_{X_{s,o}}$ = the uncertainty in the measurement of X at the supply outlet,

$U_{X_{s,i}}$ = the uncertainty in the measurement of X at the supply inlet,

$U_{X_{e,i}}$ = the uncertainty in the measurement of X at the exhaust outlet.

To calculate the exhaust effectiveness values an equation very similar to equation (A.32) was used except instead of using the average supply mass flow rate in the numerator, the

average exhaust mass flow rate was used. Equation (A.34) (ASHRAE std 84, 1991) is the equation used to calculate the exhaust effectiveness values.

$$\varepsilon = \frac{\dot{m}_e \left(X_{e,o} - X_{e,i} \right)}{\dot{m}_{\min} \left(X_{e,i} - X_{s,i} \right)} \tag{A.34}$$

where, $\dot{m}_e$ = the average mass flow rate of air on the exhaust side [kg/s],

Again similar to equation (A.33) the exhaust effectiveness values uncertainties were calculated using equation (A.35). The general form of the uncertainties in the latent, sensible, and total effectiveness values are as follows.

$$U_{\varepsilon_e} = \left(\begin{array}{l} \left(\frac{\varepsilon_e}{\dot{m}_e} U_{\dot{m}_s} \right)^2 + \left(\frac{\varepsilon_e}{\dot{m}_{\min}} U_{\dot{m}_{\min}} \right)^2 + \left(\frac{\varepsilon_e}{X_{e,i} - X_{e,o}} U_{X_{e,o}} \right)^2 \\ + \left(\frac{e_e}{X_{e,i} - X_{s,i}} U_{X_{e,i}} \right)^2 + \left(\frac{\dot{m}_e X_{s,i}}{\dot{m}_{\min} \left(X_{e,i} - X_{s,i} \right)^2} U_{X_{s,i}} \right)^2 \end{array} \right)^{1/2} \tag{A.35}$$

where, U_{ε_e} = the uncertainty in the exhaust effectiveness',

$U_{\dot{m}_e}$ = the uncertainty in the exhaust mass flow rate [kg/s],

$U_{X_{e,o}}$ = the uncertainty in the measurement of X at the exhaust outlet.

At steady-state (with no external heat gains or losses), the supply and exhaust side effectiveness values are equal. Therefore, the average of the supply and exhaust effectiveness values are also of interest in evaluating the performance of the RAMEE. The supply and exhaust sensible, latent, and total effectiveness values are averaged as in equation (A.36).

$$\varepsilon_{avg} = \frac{1}{2} \left(\varepsilon_e + \varepsilon_s \right) \tag{A.36}$$

where, ε_{avg} = the average effectiveness,

ε_e = the effectiveness on the supply side of the exchanger,

ε_s = the effectiveness on the exhaust side of the exchanger.

Using a root-sum-square the uncertainty in the average effectiveness was calculated from equation (A.37).

$$U_{\varepsilon_{avg}} = \frac{1}{2}\left(\left(U_{\varepsilon_e}\right)^2 + \left(U_{\varepsilon_s}\right)^2\right)^{1/2} \quad \text{(A.37)}$$

where, $U_{\varepsilon_{avg}}$ = the uncertainty of the average effectiveness,

U_{ε_e} = the uncertainty of the effectiveness on the supply side of the exchanger,

U_{ε_s} = the uncertainty of the effectiveness on the exhaust side of the exchanger.

A.4 CONSERVATION WITHIN UNCERTAINTY CHECKS

For the RAMEETA measurements to be valid, leakage from the system was minimized to help ensure the conservation of mass through the system. To check for the conservation of dry air, the inequality in equation (A.38) (ASHRAE std 84, 1991) was used. If the inequality was not satisfied the system was checked for leaks and the data was discarded.

$$\Delta\dot{m} = \left|\dot{m}_i - \dot{m}_o\right| \le U_{\Delta\dot{m}} \quad \text{(A.38)}$$

where, $\Delta\dot{m}$ = the difference between the measured inlet and outlet mass flow rate of air at the side of interest of the RAMEE (exhaust or supply) [kg_{DA}/s]

$\dot{m}_i$ = the mass flow rate of air measured at the inlet at the side of interest of the exchanger [kg_{DA} /s],

$\dot{m}_o$ = the mass flow rate of air measured at the outlet of the

side of interest of the exchanger [kg_{DA} /s],

$U_{\Delta\dot{m}}$ = the uncertainty in the difference between the mass flow rate in and out of the side of interest of the exchanger [kg_{DA} /s].

The uncertainty in the mass flow rate difference was calculated using a root-sum-square approach and is given in equation (A.39).

$$U_{\Delta\dot{m}} = \left(\left(\frac{\partial \Delta\dot{m}}{\partial \dot{m}_i} U_{\dot{m}_i} \right)^2 + \left(\frac{\partial \Delta\dot{m}}{\partial \dot{m}_o} U_{\dot{m}_o} \right)^2 \right)^{1/2} = \left(\left(U_{\dot{m}_i} \right)^2 + \left(U_{\dot{m}_o} \right)^2 \right)^{1/2} \qquad \text{(A.39)}$$

where, $U_{\dot{m}_i}$ = the uncertainty in the measured inlet air mass flow rate [kg_{DA} /s],

$U_{\dot{m}_o}$ = the uncertainty in the measured outlet air mass flow rate [kg_{DA} /s].

Also required to ensure the validity of the experimental measurements was the conservation of water vapor. The criterion for the conservation of water vapor used is given in equation (A.40) (ASHRAE std 84, 1991).

$$\Delta\dot{m}W = \left| \left(\dot{m}_{s,i} W_{s,i} - \dot{m}_{s,o} W_{s,o} \right) + \left(\dot{m}_{e,i} W_{e,i} - \dot{m}_{e,o} W_{e,o} \right) \right| \leq U_{\Delta\dot{m}W} \qquad \text{(A.40)}$$

where, $\Delta\dot{m}W$ = the net difference between the mass flow rate of water in and out of the exchanger [kg_W/s],

$U_{\Delta\dot{m}W}$ = the uncertainty in the net difference between the mass flow rate of water in and out of the exchanger [kg_W/s],

$\dot{m}$ = the mass flow rate of air [kg_{DA} /s],

W = the humidity ratio [kg_W/kg_{DA}],

The uncertainty in the net difference between the mass flow rate in, and out of the exchanger was calculated using equation (A.41).

$$U_{\Delta\dot{m}W} = \left(\begin{array}{l} \left(W_{s,i} U_{\dot{m}_{s,i}} \right)^2 + \left(\dot{m}_{s,i} U_{W_{s,i}} \right)^2 + \left(W_{s,o} U_{\dot{m}_{s,o}} \right)^2 + \left(\dot{m}_{s,o} U_{W_{s,o}} \right)^2 \\ + \left(W_{e,i} U_{\dot{m}_{e,i}} \right)^2 + \left(\dot{m}_{e,i} U_{W_{e,i}} \right)^2 + \left(W_{e,o} U_{\dot{m}_{e,o}} \right)^2 + \left(\dot{m}_{e,o} U_{W_{e,o}} \right)^2 \end{array} \right)^{1/2} \qquad \text{(A.41)}$$

where, $U_{\dot{m}}$ = the uncertainty in the mass flow rate of air [kg_{DA} /s],

U_W = the uncertainty in the humidity ratio [kg_W/kg_{DA}].

Another conservation principle which was checked to ensure the validity of the measurements, was the conservation of energy. Equation (A.42) (ASHRAE std 84, 1991) was used to check that energy is conserved through the system.

$$\Delta\dot{m}h = \left|\left(\dot{m}_{s,i}h_{s,i} - \dot{m}_{s,o}h_{s,o}\right) + \left(\dot{m}_{e,i}h_{e,i} - \dot{m}_{e,o}h_{e,o}\right)\right| \le U_{\Delta\dot{m}h} \qquad \text{(A.42)}$$

where, $\Delta\dot{m}h$ = the net difference between the energy in and out of the exchanger [W],

$U_{\Delta\dot{m}h}$ = the uncertainty in the net difference between the energy in and out of the exchanger [W],

$\dot{m}$ = the mass flow rate of air [kg_{DA} /s],

h = the enthalpy [J/kg_{DA}].

The uncertainty in the net difference between the mass flow rates in and out of the exchanger was calculated using equation (A.43).

$$U_{\Delta\dot{m}h} = \left(\begin{array}{l}\left(h_{s,i}U_{\dot{m}_{s,i}}\right)^2 + \left(\dot{m}_{s,i}U_{h_{s,i}}\right)^2 + \left(h_{s,o}U_{\dot{m}_{s,o}}\right)^2 + \left(\dot{m}_{s,o}U_{h_{s,o}}\right)^2 \\ + \left(h_{e,i}U_{\dot{m}_{e,i}}\right)^2 + \left(\dot{m}_{e,i}U_{h_{e,i}}\right)^2 + \left(h_{e,o}U_{\dot{m}_{e,o}}\right)^2 + \left(\dot{m}_{e,o}U_{h_{e,o}}\right)^2\end{array}\right)^{1/2} \qquad \text{(A.43)}$$

where, $U_{\dot{m}}$ = the uncertainty in the mass flow rate of air [kg_{DA} /s],

U_h = the uncertainty in the enthalpy [J/kg_{DA}].

The effectiveness values must agree within the uncertainty in the difference. Equations (A.44), (A.45), and (A.46) are the inequalities used to check for consistency in the supply and exhaust effectiveness values.

$$\Delta\varepsilon_s = \left|\varepsilon_{s,s} - \varepsilon_{s,e}\right| \le U_{\Delta\varepsilon_s}\text{,} \qquad \text{(A.44)}$$

$$\Delta\varepsilon_l = \left|\varepsilon_{l,s} - \varepsilon_{l,e}\right| \le U_{\Delta\varepsilon_l}\text{,} \tag{A.45}$$

$$\Delta\varepsilon_t = \left|\varepsilon_{t,s} - \varepsilon_{t,e}\right| \le U_{\Delta\varepsilon_t}\text{,} \tag{A.46}$$

where, $\Delta\varepsilon_s$ = the difference in the sensible effectiveness on the supply and exhaust sides of the heat exchanger,

$\Delta\varepsilon_l$ = the difference in the latent effectiveness on the supply and exhaust sides of the exchanger,

$\Delta\varepsilon_t$ = the difference in the total effectiveness on the supply and exhaust sides of the exchanger,

$U_{\Delta\varepsilon_s}$ = the uncertainty in the difference between the supply sensible effectiveness and the exhaust sensible effectiveness values,

$U_{\Delta\varepsilon_l}$ = the uncertainty in the difference between the supply latent effectiveness and the exhaust latent effectiveness values,

$U_{\Delta\varepsilon_t}$ = the uncertainty in the difference between the supply total effectiveness and the exhaust total effectiveness values.

The uncertainty in the differences between the exhaust effectiveness values and the supply effectiveness values were calculated using equations (A.47), (A.48), and (A.49).

$$U_{\Delta\varepsilon_s} = \left(\left(U_{\varepsilon_{S,s}}\right)^2 + \left(U_{\varepsilon_{S,e}}\right)^2\right)^{1/2}\text{,} \tag{A.47}$$

$$U_{\Delta\varepsilon_l} = \left(\left(U_{\varepsilon_{l,s}}\right)^2 + \left(U_{\varepsilon_{l,e}}\right)^2\right)^{1/2}\text{,} \tag{A.48}$$

$$U_{\Delta\varepsilon_t} = \left(\left(U_{\varepsilon_{t,s}}\right)^2 + \left(U_{\varepsilon_{t,e}}\right)^2\right)^{1/2}\text{.} \tag{A.49}$$

For the test to claim conformance to ANSI-ASHRAE Standard 84 (1991) the experimental uncertainties must be sufficiently small so that inequalities (A.50) to (A.54) are satisfied. Equation (A.50) is a criterion used to check for the conservation of air through the system. If the inequality is not satisfied the experimental uncertainties are too large and/or the system has significant leakage.

$$\frac{\left|\dot{m}_1 - \dot{m}_2 + \dot{m}_3 - \dot{m}_4\right|}{\frac{1}{4}\left(\dot{m}_1 + \dot{m}_2 + \dot{m}_3 + \dot{m}_4\right)} < 0.01 * Const_1 \qquad \text{(A.50)}$$

where, $\dot{m}_1$ = the mass flow rate measured at the supply inlet [kg/s],

$\dot{m}_2$ = the mass flow rate measured at the supply outlet [kg/s],

$\dot{m}_3$ = the mass flow rate measured at the exhaust inlet [kg/s],

$\dot{m}_4$ = the mass flow rate measured at the exhaust outlet [kg/s],

$Const_1$ = 1 for field tests and 2 for laboratory testing.

Equation (A.51) (ASHRAE std 84, 1991) was used to check for the conservation of air on the supply side of the exchanger.

$$\frac{\left|\dot{m}_1 - \dot{m}_2\right|}{\frac{1}{2}\left(\dot{m}_1 + \dot{m}_2\right)} < 0.008 * Const_1 \qquad \text{(A.51)}$$

Similarly, to check for the conservation of air on the exhaust side of the exchanger the inequality in equation (A.52) (ASHRAE std 84, 1991) was used.

$$\frac{\left|\dot{m}_3 - \dot{m}_4\right|}{\frac{1}{2}\left(\dot{m}_3 + \dot{m}_4\right)} < 0.008 * Const_1 \qquad \text{(A.52)}$$

An additional check was done to ensure that water vapour was conserved within experimental uncertainty. The criteria used to ensure the conservation of water vapor within experimental uncertainty is given in equation (A.53) (ASHRAE std 84, 1991).

$$\frac{\left|\dot{m}_1 W_1 - \dot{m}_2 W_2 + \dot{m}_3 W_3 - \dot{m}_4 W_4\right|}{\left|\dot{m}_1 W_1 - \dot{m}_3 W_3\right|} < 0.06 * Const_1 \qquad \text{(A.53)}$$

where, W_1 = the humidity at the supply air inlet [kg/kg],

W_2 = the humidity at the supply air outlet [kg/kg],

W_3 = the humidity at the exhaust air inlet [kg/kg],

W_4 = the humidity at the exhaust air outlet [kg/kg].

To check that energy is conserved within experimental uncertainty, equation (A.54) (ASHRAE std 84, 1991) was used.

$$\frac{\left|\dot{m}_1 h_1 - \dot{m}_2 h_2 + \dot{m}_3 h_3 - \dot{m}_4 h_4\right|}{\left|\dot{m}_1 h_1 - \dot{m}_3 h_3\right|} < 0.05 * Const_1 \qquad \text{(A.54)}$$

where, h_1 = the enthalpy at the supply air inlet [kJ/kg],

h_2 = the humidity at the supply air outlet [kJ/kg],

h_3 = the humidity at the exhaust air inlet [kJ/kg],

h_4 = the humidity at the exhaust air outlet [kJ/kg].

APPENDIX B

PERMATRAN MEASUREMENT ANALYSIS

Prior to measuring the membranes, the cell calibration WVTR is measured in order to determine the calibration VDR. The calibration VDR includes the nitrogen boundary layer VDR, the desiccant boundary layer VDR, and the guard membrane VDR. Therefore, by installing the test membrane the total VDR is equal to the calibration VDR plus the membrane VDR is series. All of the measured WVTR are normalized to a 100% RH concentration gradient. Therefore, when equating the total resistance to the membrane resistance in series with the calibration resistance the concentration gradient cancels leaving only the mass fluxes as shown in equation (B.1).

$$R_T = R_{CAL} + R_M \Rightarrow \frac{\Delta C}{\dot{m}''_T} = \frac{\Delta C}{\dot{m}''_{CAL}} + \frac{\Delta C}{\dot{m}''_M}$$

$$\dot{m}''_T = \left(\frac{1}{\dot{m}''_M} + \frac{1}{\dot{m}''_{CAL}} \right)^{-1} \tag{B.1}$$

where, R_Y = the total VDR in the Permatran [s/m],

R_{CAL} = the calibration VDR [s/m],

R_M = the membrane VDR [s/m],

$\dot{m}''_{TOT}$ = the total WVTR [g/m^{2}day],

$\dot{m}''_{CAL}$ = the calibration WVTR [g/m^{2}day],

$\dot{m}''_M$ = the theoretical membrane WVTR [g/m^{2}day].

B.1 Conversion from WVTR to VDR

To convert the WVTR output by the Permatran to VDR, the outlet vapour concentration needed to be known. However, the WVTR were calculated by the Permatran based on the outlet vapour concentration. Therefore, equation (B.2) (Gibson, 2000) was used to back calculate the outlet concentration.

$$\frac{\dot{m}}{A} = \dot{m}'' = \frac{Q(C_2 - C_1)}{A} \tag{B.2}$$

where, $\dot{m}$ = vapour mass flow rate through the sample [kg/s],

$\dot{m}''$ = vapour transmission rate through the sample [kg/m^{2}s],

Q = the volume flow rate of nitrogen at the test temperature [m^3/s],

C_2 = the outlet nitrogen vapour concentration [kg/m^3],

C_1 = the inlet nitrogen vapour concentration [kg/m^3],

A = the transfer area [m^2].

The WVTR, the inlet nitrogen vapour concentration (C_1=0 kg/m^3, dry), and the volume flow of nitrogen were output by the Permatran. Therefore, rearranging equation (B.2) and canceling the inlet nitrogen vapour concentration yields the outlet vapour concentration.

$$C_2 = \frac{\dot{m}'' A}{Q} \tag{B.3}$$

The volume flow rate of nitrogen was output by the Permatran software in units of SCCM (standard cubic centimeters per minute). Using the ideal gas law, the standard volume flow rate can be substituted for the actual flow rate yielding equation (B.4).

$$C_2 = \frac{\dot{m}'' A \rho}{Q_S \rho_S} \tag{B.4}$$

where, ρ = nitrogen density at the test temperature (23°C) [1.1919 kg/m^3],

ρ_S = nitrogen density at the standard temp. (0°C) [1.2922 kg/m^3],

Q_S = nitrogen volume flow rate at the standard temp. (0°C) [m^3/s].

The outlet vapour concentration was then combined with the vapour transmission rate to calculate the VDR as shown in equation (B.5) (Gibson, 2000).

$$R = \frac{\Delta\overline{C}}{\dot{m}''} \tag{B.5}$$

where, R = the vapour diffusion resistance between the reservoir and the nitrogen stream [s/m],

$\Delta\overline{C}$ = log mean concentration gradient between the water reservoir and the nitrogen stream throughout the test cells [kg/m^3].

The log mean concentration gradient is the average vapour concentration to which the membrane is exposed which creates the driving potential for the flow of vapour through the membrane. To calculate the log mean concentration gradient equation (B.6) was used (Gibson, 2000).

$$\Delta\overline{C} = \frac{\Delta C_a - \Delta C_b}{\ln\left(\frac{\Delta C_a}{\Delta C_b}\right)} \tag{B.6}$$

where, ΔC_a = the vapour concentration difference between the reservoir and the nitrogen stream at the inlet of the test cell [kg/m^3].

ΔC_b = the vapour concentration difference between the reservoir and the nitrogen stream at the outlet of the test cell [kg/m^3].

The inlet and outlet concentration gradients are defined in equations (B.7) and (B.8). The subscripts refer to the locations 1 through 4 shown on Figure 2.5. The vapour

concentration in the reservoir is maintained at the saturation vapour concentration of water in air at the test temperature (23°C).

$$\Delta C_a = C_3 - C_1 \tag{B.7}$$

$$\Delta C_b = C_4 - C_2 \tag{B.8}$$

The nitrogen inlet concentration (C_1) is zero and the outlet concentration (C_2) is as calculated using equation (B.4). Substituting equations (B.7) and (B.8) into (B.6) yields the log mean concentration gradient.

$$\Delta\overline{C} = \frac{C_3 - (C_3 - C_2)}{\ln\left(\frac{C_3}{C_3 - C_2}\right)} = \frac{C_2}{\ln\left(\frac{C_3}{C_3 - C_2}\right)} \tag{B.9}$$

Substituting equation (B.9) into (B.5), and solving for the VDR, yields equation (B.10).

$$R = \frac{C_2}{\ln\left(\frac{C_3}{C_3 - C_2}\right)\dot{m}''} \tag{B.10}$$

B.2 Interpreting the WVTR Measurements

From equation (B.4), the outlet vapour concentration during calibration could be calculated from equation (B.11).

$$(C_2)_{CAL} = \frac{\dot{m}''_{CAL}\, A\rho}{Q_S \rho_S} \tag{B.11}$$

where, $(C_2)_{CAL}$ = the calibration outlet nitrogen vapour concentration [kg/m^3].

However, using equation (B.11) yielded calibration outlet vapour concentrations higher than the maximum attainable (C_3). This was because the WVTR were normalized to a 100% RH gradient. Therefore, the actual WVTR had to be calculated from the normalized

values. According to Mocon, the normalized WVTR are calculated as shown in equation (B.12).

$$m''_N = \frac{100\% - 0\%}{100\% - \%RH} m''_A \tag{B.12}$$

where, m''_N = the normalized WVTR output by the Permatran [g_W/m^2day].

m''_A = the actual WVTR observed in the Permatran [g_W/m^2day].

Therefore, substituting in the definition of RH and solving for the outlet vapour concentration yielded equation (B.13).

$$\dot{m}''_N = \dot{m}''_{Act}\left(\frac{1}{1 - C_2/C_3}\right)$$

$$C_2 = \left(1 - \frac{\dot{m}''_{Act}}{\dot{m}''_N}\right)C_3 \tag{B.13}$$

Substituting equation (B.4) for the actual WVTR into equation (B.13) yielded equation (B.14).

$$C_2 = \left(\frac{Q_S \rho_S}{\dot{m}''_N A\rho} + \frac{1}{C_3}\right)^{-1} \tag{B.14}$$

Using equation (B.14) the calibration outlet vapour concentrations (C_2) were now close to the 60% RH. Substituting the calibration outlet nitrogen concentration and calibration WVTR into equation (B.10) yielded equation (B.15).

$$R_{CAL} = \frac{(C_2)_{CAL}}{\ln\left(\frac{(C_2)_{CAL}}{C_3 - (C_2)_{CAL}}\right)\dot{m}_{CAL}} \tag{B.15}$$

Finally, by substituting the calibration resistances obtained using equation (B.15) and the total resistance obtained using equation (B.10), the test membrane resistance was calculated using equation (B.16).

$$R_M = R_T - R_{CAL} \tag{B.16}$$

APPENDIX C

UNCERTAINTY IN THE MODULUS OF ELASTICITY

The uncertainty in the modulus of elasticity is dependent on the uncertainty in the deflection measurements and the uncertainty in the pressure measurements. These uncertainties are dependent on the calibration process. As such, the methods used to calibrate these instruments and to determine the associated uncertainties are outlined in this Appendix. How these uncertainties were propagated into the modulus results is also outlined in this Appendix.

C.1 Calibration Uncertainty

The linearly variable displacement transducer (LVDT) and pressure transducer were calibrated, a precision uncertainty is introduced from calibration. Typical calibration curves for the pressure transducer and the LVDT are shown in Figures (C.1) and (C.2) respectively. Figure C.1 was obtained by stepping the pressure up using a Druck as the reference standard (uncertainty of 6.9 Pa (0.001 psi)) and recording the voltage output by the pressure transducer. Similarly, Figure C.2 was obtained by stepping through positions using a linear caliper as the reference standard (associated uncertainty of 0.02mm) and recording the voltage output of the LVDT.

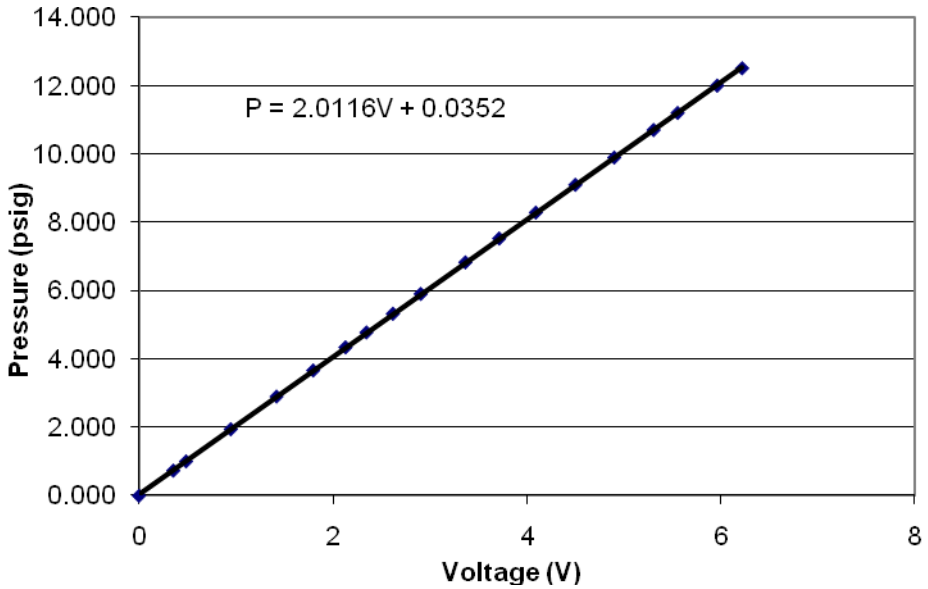

Figure C.1. Typical pressure transducer calibration curve with best fit equation shown.

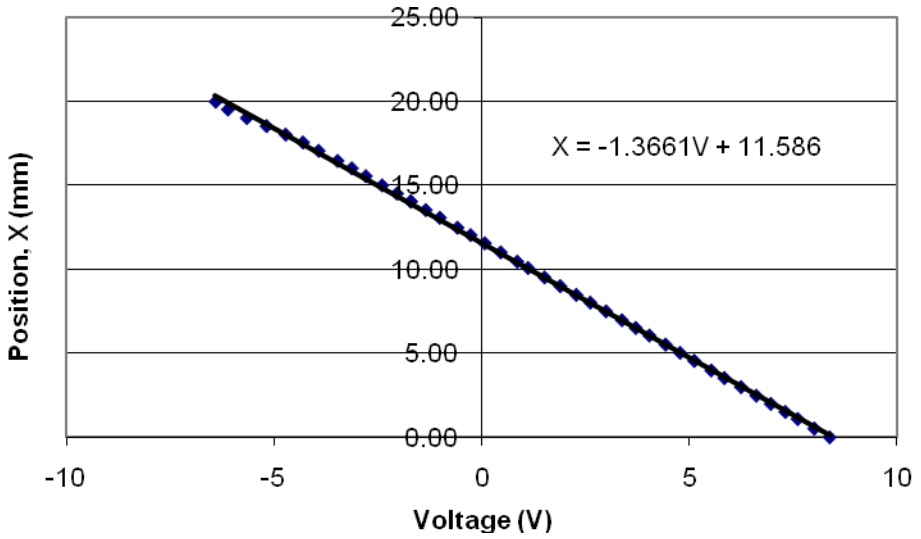

Figure C.2. Typical LVDT calibration curve with best fit equation shown.

A regression analysis, as outlined by ASME PTC 19.1, was used to determine the precision uncertainty introduced by using the best fit equations shown in Figures C.1 and C.2. The standard error of estimate (SEE) was calculated as shown in equation (C.1). By

multiplying the SEE by the appropriate t-student distribution value, the precision uncertainty in the measurement is calculated as in equation (C.2).

$$SEE = \left[\frac{\sum_{k=1}^{n} \left(y_{BF,k} - y_{RS,k} \right)^2}{N - C} \right]^{1/2} \tag{C.1}$$

where, SEE = the standard error of estimate introduced by using a best fit,

$y_{BF,K}$ = the value obtained using the best fit equation at the calibration point k,

$y_{RS,K}$ = the reference standard measurement at calibration point k,

N = the number of calibration points,

C = the number of constants in the calibration curve (2 for linear).

$$P_{BF} = SEE \cdot t \tag{C.2}$$

where, P_{BF} = the best fit precision uncertainty in the calibrated measurement,

t = the t-student distribution value at 95% confidence and N-1 degrees of freedom.

The total measurement uncertainty was obtained using a root sum square with the calibration device uncertainty. However, the total measurement uncertainty was always dominated by the best fit precision uncertainty due to the relatively high accuracy and high precision of the reference standards.

C.2 Determining the Uncertainty in the Modulus of Elasticity

The uncertainty in the modulus of elasticity caused by the pressure and displacement measurement uncertainties is calculated using the propagation of error as outlined by ASME PTC 19.1 (1998). The stress and strain in the membrane are calculated

using equations (3.1) and (3.2) respectively. The uncertainty in the stresses and strains depend on the uncertainties in the pressure and displacement measurements as shown in equations (C.3) and (C.4) respectively.

$$U_\sigma = \left[\left(\frac{a^2}{4h\Delta z} U_P \right)^2 + \left(\frac{Pa}{2h\Delta z} U_a \right)^2 + \left(\frac{Pa^2}{4h^2\Delta z} U_h \right)^2 + \left(\frac{Pa^2}{4h\Delta z^2} U_{\Delta z} \right)^2 \right]^{1/2}$$

(C.3)

where, U_σ = the uncertainty in the tensile stress induced on the membrane in the θ-r plane [Pa],

U_P = the uncertainty in the liquid pressure below the membrane [Pa],

U_a = the uncertainty in the radius of the bulge test cell [mm],

U_h = the uncertainty in the membrane deflections [mm],

$U_{\Delta z}$ = the uncertainty in the membrane thickness [mm].

$$U_{\varepsilon_\theta} = \left[\left(\frac{4h}{3a^2} U_h \right)^2 + \left(\frac{4h^2}{3a^3} U_a \right)^2 \right]^{1/2} \quad \text{(C.4)}$$

where, U_{ε_θ} = the uncertainty in the θ component of the membrane strains [mm/mm].

After offsetting the zero for the pre-strain in the membranes the first point higher than the 0.1 strain is used to determine the modulus of elasticity. The modulus is calculated using equation (C.5) and thus the uncertainty in this modulus is calculated from equation (C.6).

$$E = \frac{\sigma}{\varepsilon_\theta} \quad \text{(C.5)}$$

$$U_E = \left[\left(\frac{U_\sigma}{\varepsilon_\theta} \right)^2 + \left(\frac{\sigma}{\varepsilon_\theta^2} U_{\varepsilon_\theta} \right)^2 \right]^{1/2} \quad \text{(C.6)}$$

where, E = the modulus of elasticity [MPa],

U_E = the uncertainty in the modulus of elasticity [MPa].

For each membrane four sets of data were taken to reduce the statistical uncertainty in the modulus of elasticity. Therefore, the total uncertainty in the modulus of elasticity is calculated using equation (A.14) with a sample size of 4.

C.3 Determining the Uncertainty in the Air Flow Rate

Using the root sum square method outlined by ASME PTC 19.1 (1998), the uncertainty in the air volume flow rate, calculated using equation (4.1), is calculated using equation (C.7). This equation assumes no uncertainty in the discharge coefficient.

$$U_q = 17.52 \cdot C_d \left[\left(\frac{2q}{D_2} U_{D_2} \right)^2 + \left(\frac{q}{2\Delta P} U_{\Delta P} \right)^2 + \left(\frac{q}{2\rho} U_\rho \right)^2 + \left(\frac{2qd^3}{(1-d^4)} U_d \right)^2 \right] \quad \text{(C.7)}$$

where, Uq = the uncertainty in the air flow rate [m^3/s],

U_{D_2} = the uncertainty in the orifice plate diameter [0.0001 m],

U_{D_1} = the uncertainty in the pipe diameter [0.0001 m],

$U_{\Delta P}$ = the uncertainty in the pressure transducer measurement [0.04 in. H_2O],

U_ρ = the uncertainty in the air density [kg/m^3].

U_d = $\left[\left(\frac{U_{D_2}}{D_1} \right)^2 + \left(\frac{D_2}{D_1^2} U_{D_1} \right)^2 \right]^{1/2}$ = [0.002 mm].

APPENDIX D

MASS FLOW METER, TEMPERATURE, AND RELATIVE HUMIDTY, CALIBRATION PROCEDURES

The mass flow rates of the desiccant within the energy exchanger test facility are measured using mass flow metres. In addition, there are many relative humidity and temperature measurements taken within the energy exchanger test facility. Therefore, all of these sensors required calibration. In this Appendix, the processes used to calibrate these sensors and determine their associated measurement uncertainties are outlined.

D.1 Calibration of the Mass Flow Meter

To generate the calibration curve for the mass flow meters five desiccant flow rates were used. The flows were generated using a pump from the energy exchanger test facility and varying the position of the control valve. A stopwatch was started and the flow was diverted into a bucket. Once the bucket was near full the flow was removed and the time was stopped. By weighing the bucket and measuring the desiccant density using the densitometer the flow rate was calculated. During the test the voltage was recorded more than 30 times and an average was determined. The resulting calibration curve is shown in Figure D.1 with the best fit equation.

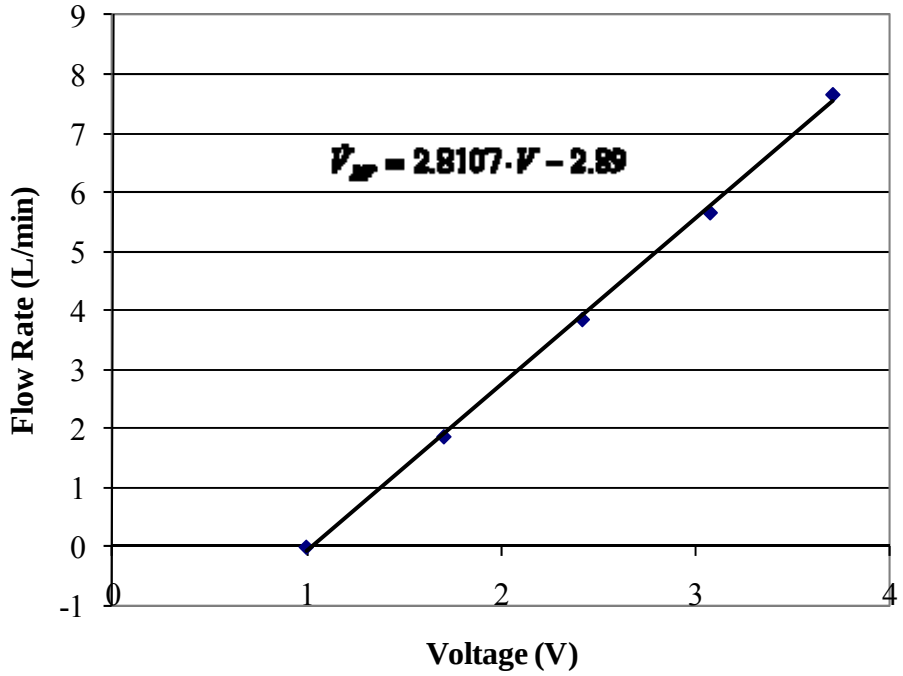

Figure D.1. The calibration curve obtained for a desiccant mass flow meter.

Using the regression analysis method outlined in Appendix C.1, the measurement uncertainty for the flow meter was obtained to be 0.3 L/min.

D.2 Temperature Measurement Device Calibration

The first step in calibrating the temperature devices was to decide on the appropriate range of measurement. A dry block with a programmable temperature profile (±0.01°C) was used to generate the reference standard test trajectory as shown in Figure D.2. The temperature measurements obtained for the calibration test trajectory is also plotted in Figure D.2.

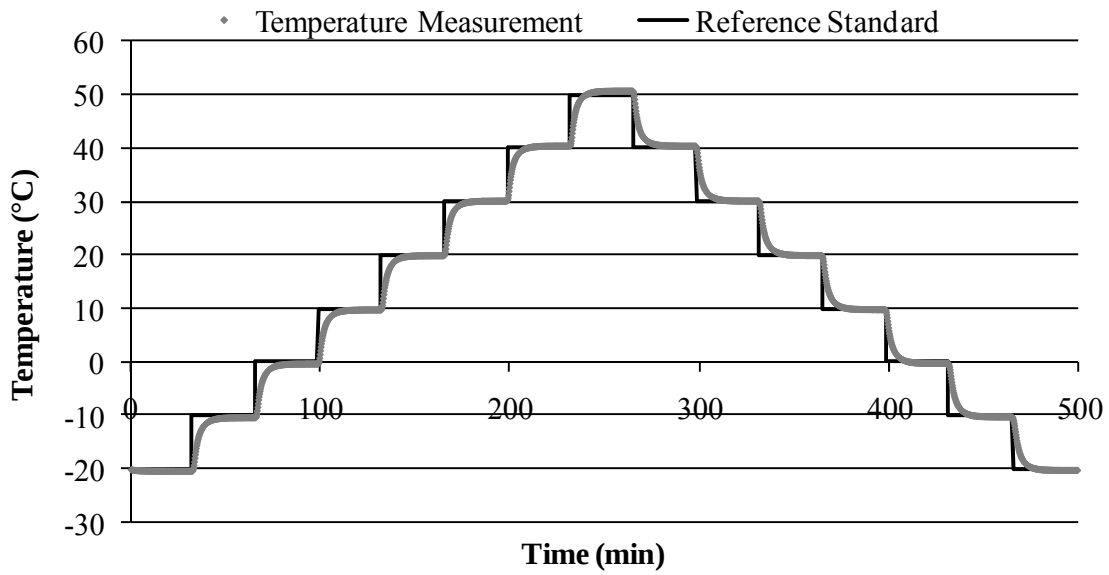

Figure D.2. Typical temperature response for the temperature/RH sensor to the reference standard temperature profile.

The temperature/RH sensors are relatively large, unlike thermocouples, requiring a few minutes to react to a change in the reference temperature. The steady state temperature measurements at each of the calibration temperatures were used to obtain averages for each reference temperature. These averages were then plotted against the reference temperatures to obtain a calibration curve as shown in Figure D.3.

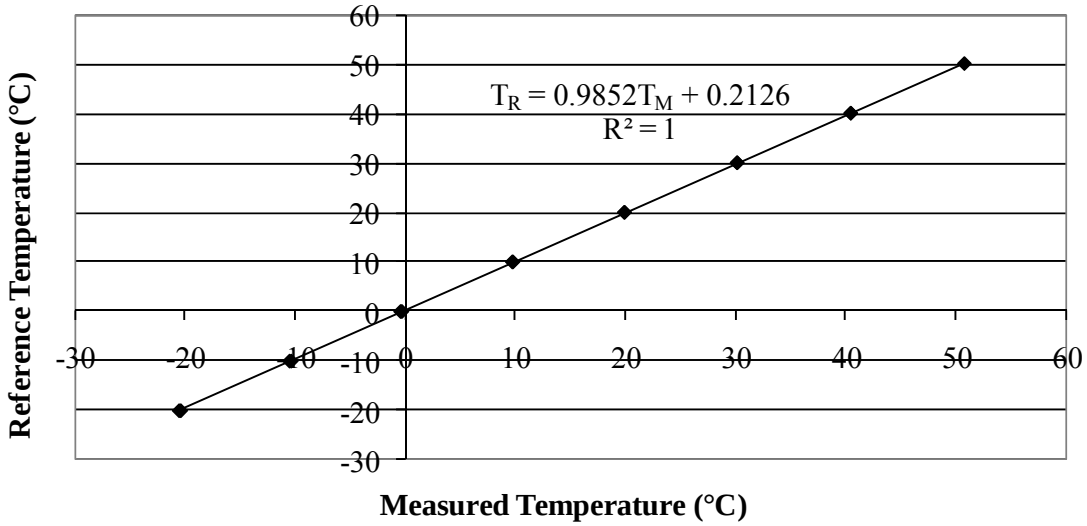

Figure D.3. Average of the steady temperature measurements plotted against the reference standard temperature.

Using the calibration curve presented in Figure D.3 and the regression analysis of Appendix C.1, the sensor measurement uncertainty is obtained.

D.3 Relative Humidity Measurement Device Calibration

The calibration process for the relative humidity sensors is analogous to the temperature sensors. However, instead of using a dry block to generate reference temperature, a relative humidity chamber is used. Similar to the temperature calibration process, a sample of the calibration data obtained for the relative humidity calibration test trajectory is shown in Figure D.4. Again, by obtaining a mean of the steady state relative humidity measurements at each of the calibration set points the calibration curve for the sensor is generated as shown in Figure D.5. Lastly, using the regression analysis outlined in Appendix C.1, the uncertainty in the relative humidity measurement is obtained.

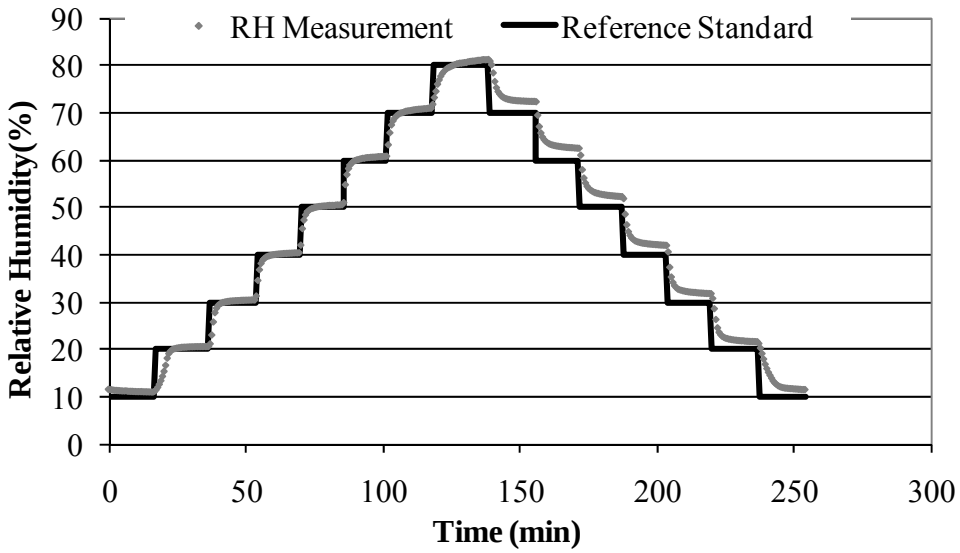

Figure D.4. Typical relative humidity response for the temperature/RH sensor to the reference standard relative humidity profile.

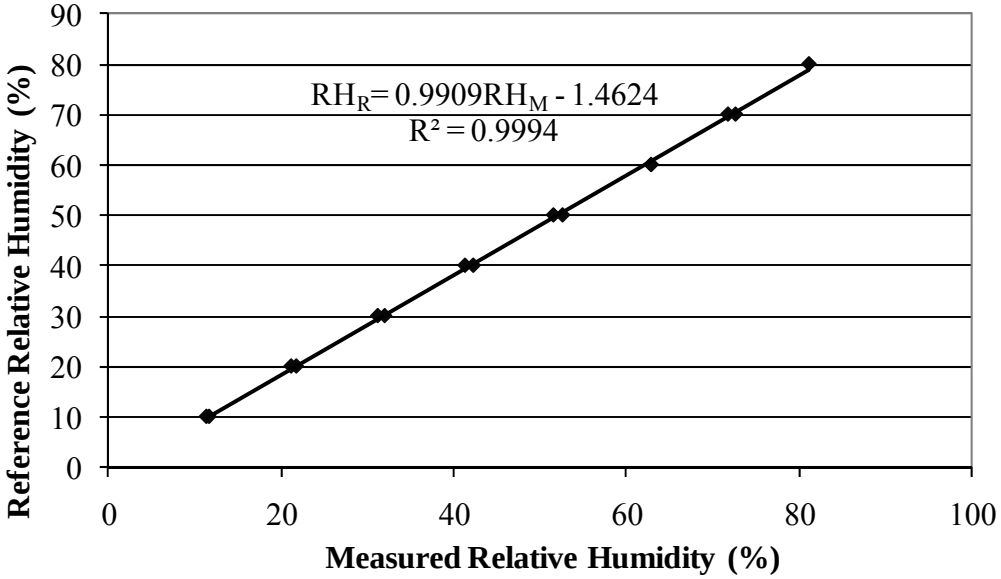

Figure D.5. Average of the steady relative humidity measurements plotted against the reference standard relative humidity.

APPENDIX E

RAMEE PROTOTYPE 4 CONSTRUCTION DRAWINGS

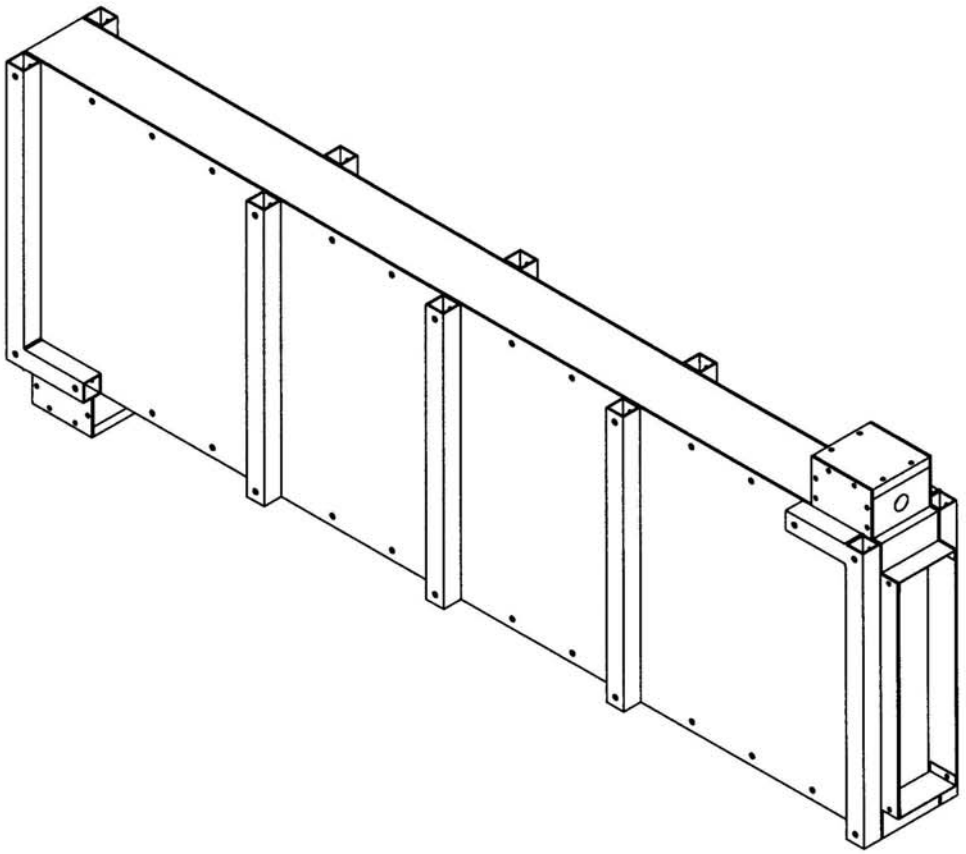

UNLESS OTHERWISE SPECIFIED:		NAME	DATE
DIMENSIONS ARE IN INCHES TOLERANCES: FRACTIONAL ± ANGULAR: MACH ± BEND ± TWO PLACE DECIMAL ± THREE PLACE DECIMAL ±	DRAWN	DB	09/09/07
	CHECKED		
	ENG APPR.		
	MFG APPR.		
INTERPRET GEOMETRIC TOLERANCING PER:	Q.A.		
MATERIAL N/A	Number of Duplicates: **N/A**		
FINISH See Drawing			
DO NOT SCALE DRAWING			

TITLE: Exchanger

SIZE	DWG. NO.	REV
A	1	1

SCALE: 1:7 | SHEET 1 OF 11

5 4 3 2 1

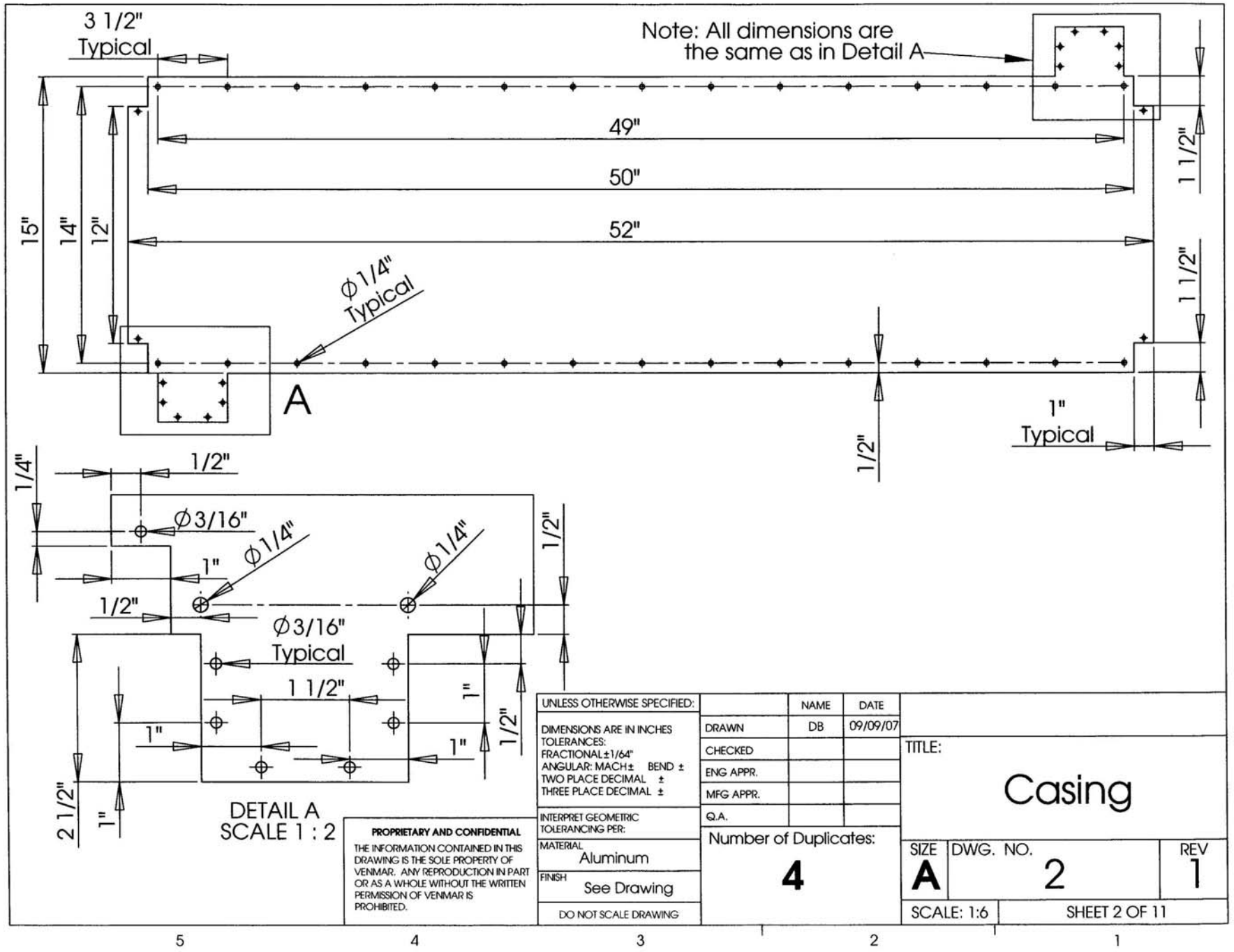
3 1/2"
Typical
Note: All dimensions are
the same as in Detail A
49"
50"
52"
15"
14"
12"
1 1/2"
1 1/2"
Ø1/4"
Typical
A
1/2"
1"
Typical
1/4"
1/2"
Ø3/16"
Ø1/4"
Ø1/4"
1"
1/2"
1/2"
Ø3/16"
Typical
1 1/2"
1"
1"
1"
1/2"
2 1/2"
1"
DETAIL A
SCALE 1 : 2
PROPRIETARY AND CONFIDENTIAL
THE INFORMATION CONTAINED IN THIS DRAWING IS THE SOLE PROPERTY OF VENMAR. ANY REPRODUCTION IN PART OR AS A WHOLE WITHOUT THE WRITTEN PERMISSION OF VENMAR IS PROHIBITED.
UNLESS OTHERWISE SPECIFIED:
DIMENSIONS ARE IN INCHES
TOLERANCES:
FRACTIONAL ±1/64"
ANGULAR: MACH ± BEND ±
TWO PLACE DECIMAL ±
THREE PLACE DECIMAL ±
INTERPRET GEOMETRIC TOLERANCING PER:
MATERIAL
Aluminum
FINISH
See Drawing
DO NOT SCALE DRAWING
NAME
DATE
DRAWN
DB
09/09/07
CHECKED
ENG APPR.
MFG APPR.
Q.A.
Number of Duplicates:
4
TITLE:
Casing
SIZE
A
DWG. NO.
2
REV
1
SCALE: 1:6
SHEET 2 OF 11
5
4
3
2
1

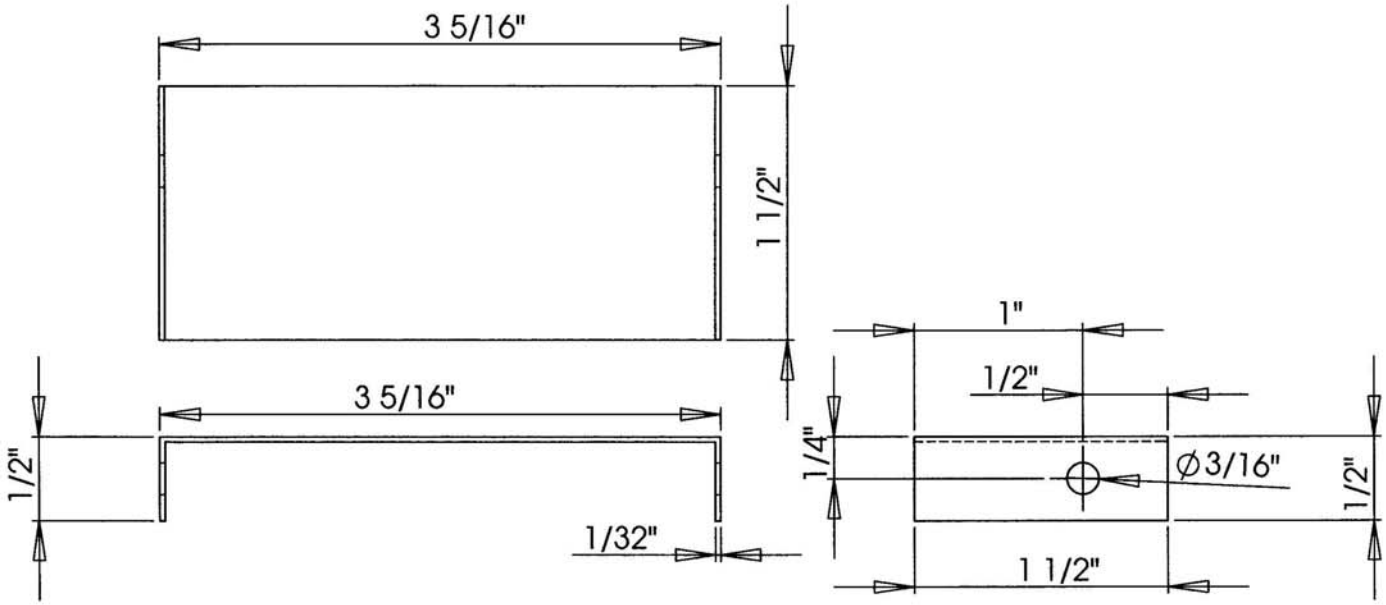

Note: Constructed from 4 5/16" x 1 1/2" x 1/32" Plate Aluminium

UNLESS OTHERWISE SPECIFIED:		NAME	DATE
DIMENSIONS ARE IN INCHES TOLERANCES: FRACTIONAL ±1/32" ANGULAR: MACH ± BEND ± TWO PLACE DECIMAL ± THREE PLACE DECIMAL ±	DRAWN	DB	21/06/07
	CHECKED		
	ENG APPR.		
	MFG APPR.		
INTERPRET GEOMETRIC TOLERANCING PER:	Q.A.		
MATERIAL: Aluminum	Number of Duplicates: 8		
FINISH: See Drawing			
DO NOT SCALE DRAWING			

TITLE: Duct Attachment

SIZE	DWG. NO.	REV
A	3	1

SCALE: 1:1 | SHEET 3 OF 11

5 4 3 2 1

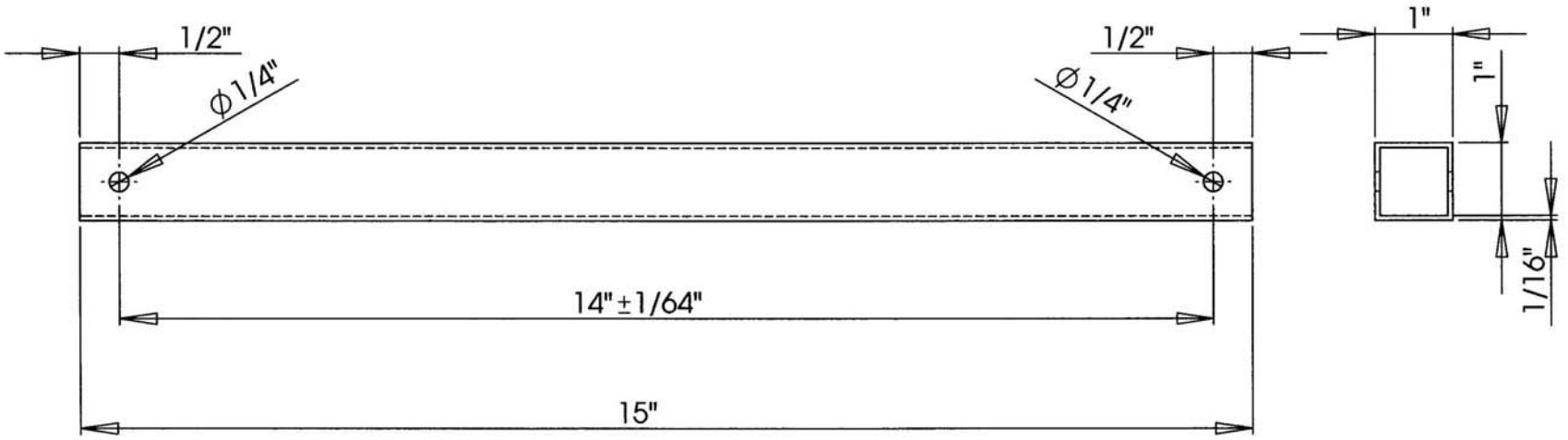

Note: Constructed from 1"x1"x1/16" square tubing

		NAME	DATE
UNLESS OTHERWISE SPECIFIED:			
DIMENSIONS ARE IN INCHES TOLERANCES: FRACTIONAL ±1/32" ANGULAR: MACH ± BEND ± TWO PLACE DECIMAL ± THREE PLACE DECIMAL ±	DRAWN	DB	21/06/07
	CHECKED		
	ENG APPR.		
	MFG APPR.		
	Q.A.		
INTERPRET GEOMETRIC TOLERANCING PER:			
MATERIAL Aluminum			
FINISH See Drawing			
DO NOT SCALE DRAWING			

Number of Duplicates: **12**

TITLE: Supports

SIZE	DWG. NO.	REV
A	4	1

SCALE: 1:2 | SHEET 4 OF 11

5 4 3 2 1

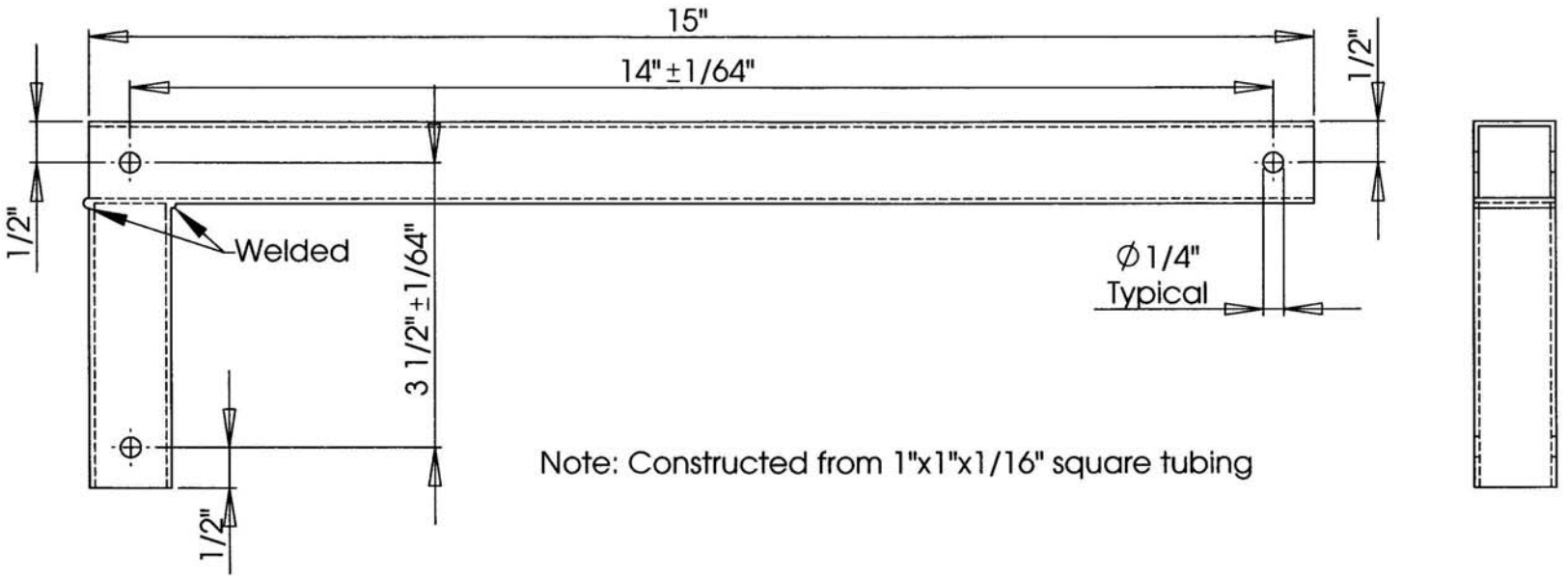

Note: Constructed from 1"x1"x1/16" square tubing

UNLESS OTHERWISE SPECIFIED:		NAME	DATE
DIMENSIONS ARE IN INCHES TOLERANCES: FRACTIONAL ±1/32" ANGULAR: MACH ± BEND ± TWO PLACE DECIMAL ± THREE PLACE DECIMAL ±	DRAWN	DB	21/06/07
	CHECKED		
	ENG APPR.		
	MFG APPR.		
INTERPRET GEOMETRIC TOLERANCING PER:	Q.A.		
MATERIAL: Aluminum	Number of Duplicates: 8		
FINISH: See Drawing			
DO NOT SCALE DRAWING			

TITLE: Supports 1

SIZE	DWG. NO.	REV
A	5	1

SCALE: 1:2 | SHEET 5 OF 11

5 4 3 2 1

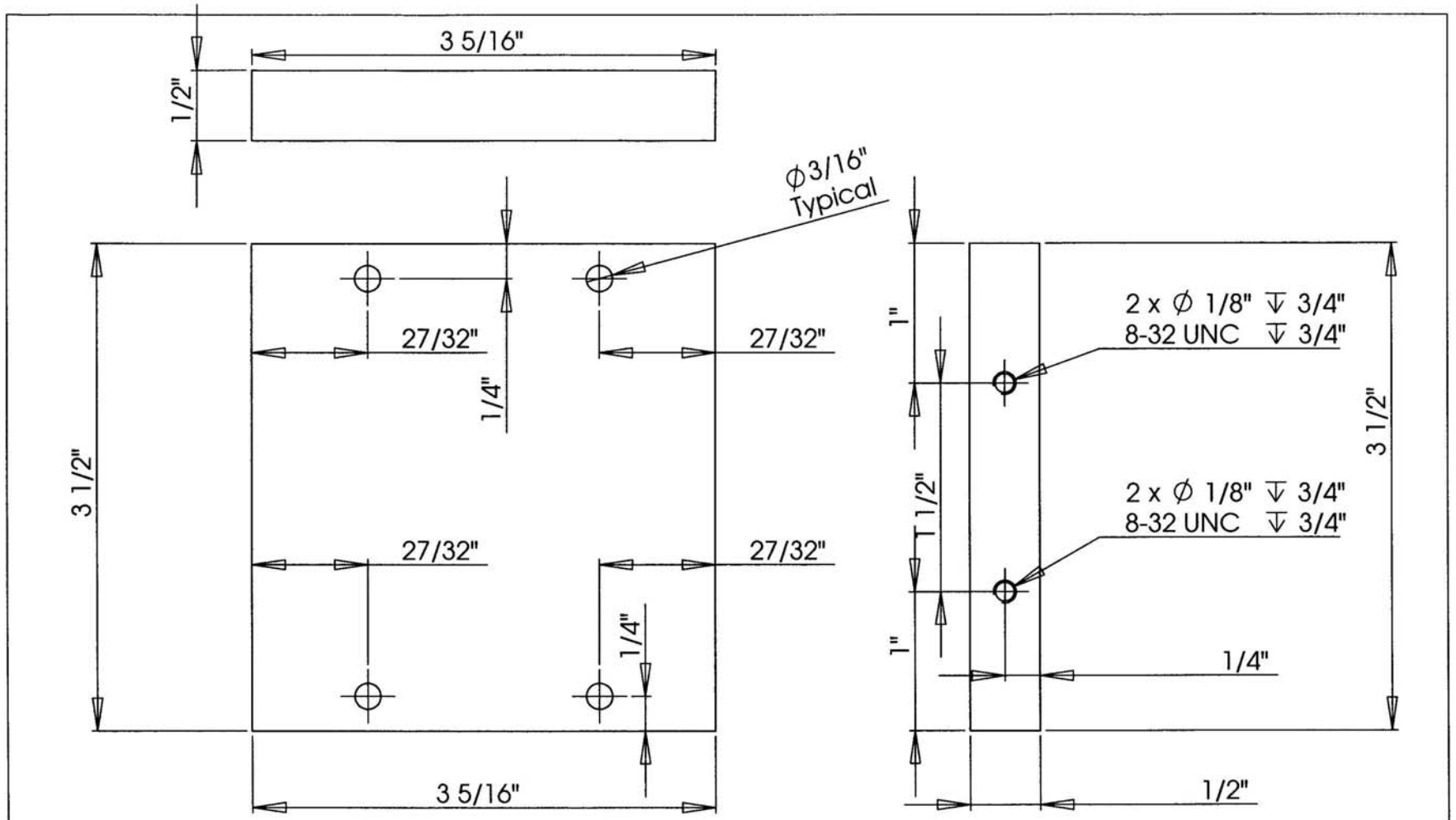

UNLESS OTHERWISE SPECIFIED:		NAME	DATE
DIMENSIONS ARE IN INCHES TOLERANCES: FRACTIONAL ±1/32" ANGULAR: MACH ± BEND ± TWO PLACE DECIMAL ± THREE PLACE DECIMAL ±	DRAWN	DB	21/06/07
	CHECKED		
	ENG APPR.		
	MFG APPR.		
	Q.A.		
INTERPRET GEOMETRIC TOLERANCING PER:	Number of Duplicates: 4		
MATERIAL: Delrin			
FINISH: See Drawing			
DO NOT SCALE DRAWING			

PROPRIETARY AND CONFIDENTIAL

THE INFORMATION CONTAINED IN THIS DRAWING IS THE SOLE PROPERTY OF VENMAR. ANY REPRODUCTION IN PART OR AS A WHOLE WITHOUT THE WRITTEN PERMISSION OF VENMAR IS PROHIBITED.

TITLE: Header Top

SIZE	DWG. NO.	REV
A	6	1

SCALE: 1:1 | SHEET 6 OF 11

5 4 3 2 1

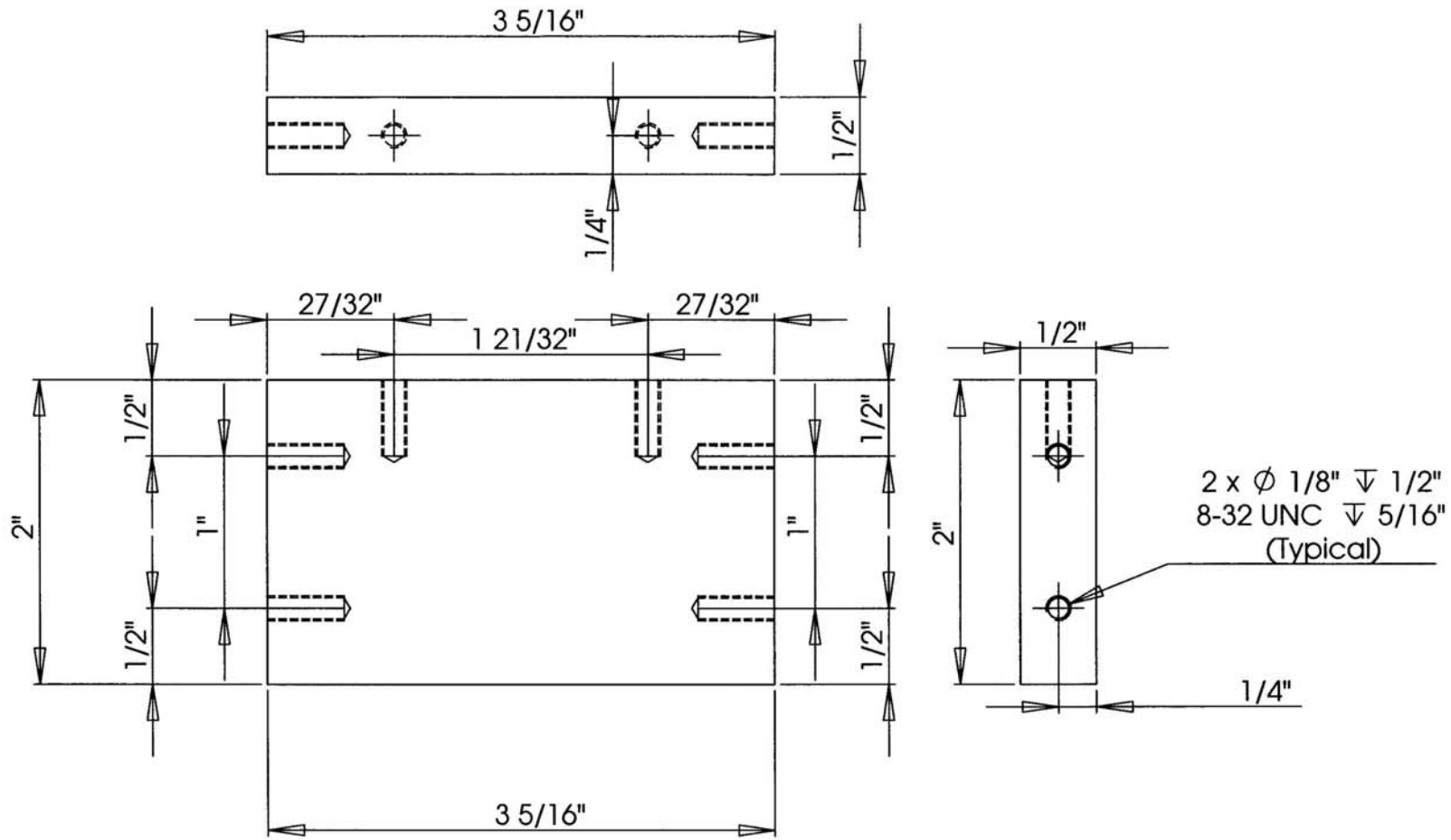

UNLESS OTHERWISE SPECIFIED:		NAME	DATE
DIMENSIONS ARE IN INCHES TOLERANCES: FRACTIONAL ±1/32" ANGULAR: MACH ± BEND ± TWO PLACE DECIMAL ± THREE PLACE DECIMAL ±	DRAWN	DB	21/06/07
	CHECKED		
	ENG APPR.		
	MFG APPR.		
INTERPRET GEOMETRIC TOLERANCING PER:	Q.A.		
MATERIAL: Delrin	Number of Duplicates: 4		
FINISH: See Drawing			
DO NOT SCALE DRAWING			

TITLE: **Header Back**

SIZE	DWG. NO.	REV
A	7	1

SCALE: 1:1 | SHEET 7 OF 11

5 4 3 2 1

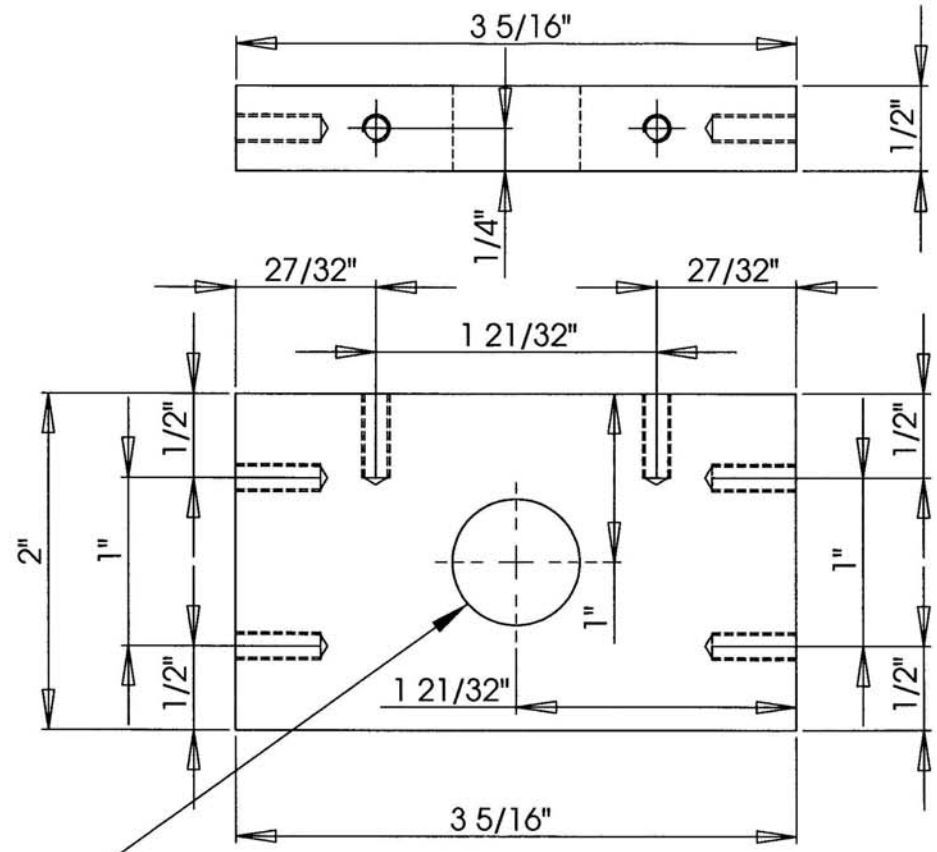

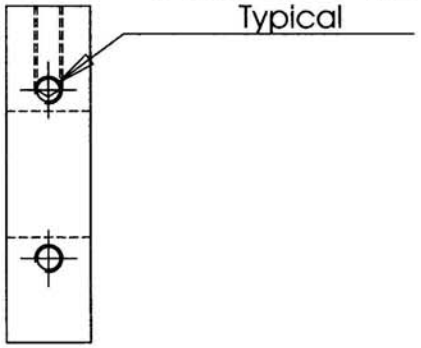

Standard 3/4" Garden Hose
Taperred Threading

UNLESS OTHERWISE SPECIFIED:		NAME	DATE
DIMENSIONS ARE IN INCHES TOLERANCES: FRACTIONAL ±1/32" ANGULAR: MACH ± BEND ± TWO PLACE DECIMAL ± THREE PLACE DECIMAL ±	DRAWN	DB	21/06/07
	CHECKED		
	ENG APPR.		
	MFG APPR.		
INTERPRET GEOMETRIC TOLERANCING PER:	Q.A.		
MATERIAL: Delrin	Number of Duplicates: 4		
FINISH: See Drawing			
DO NOT SCALE DRAWING			

TITLE: Header Front

SIZE	DWG. NO.	REV
A	8	1

SCALE: 1:1 | SHEET 8 OF 11

5 4 3 2 1

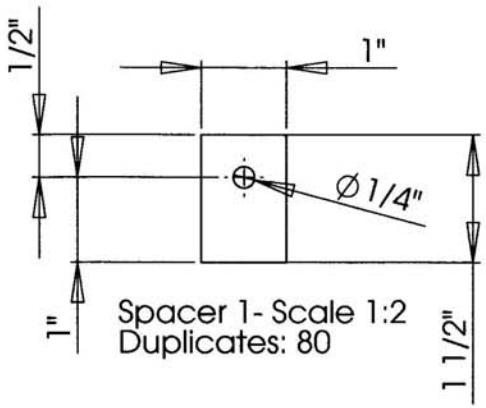

Spacer 1- Scale 1:2
Duplicates: 80

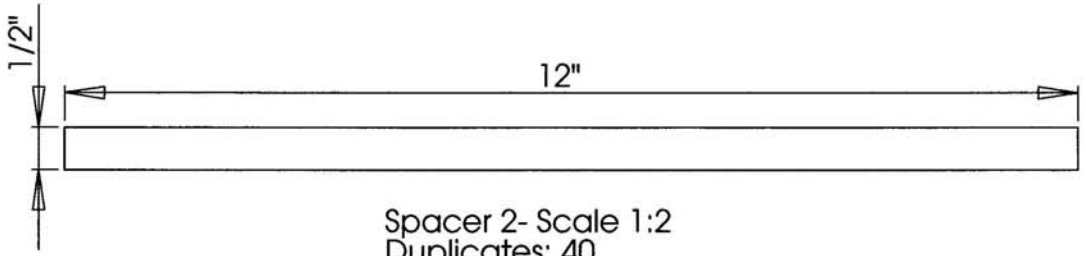

Spacer 2- Scale 1:2
Duplicates: 40

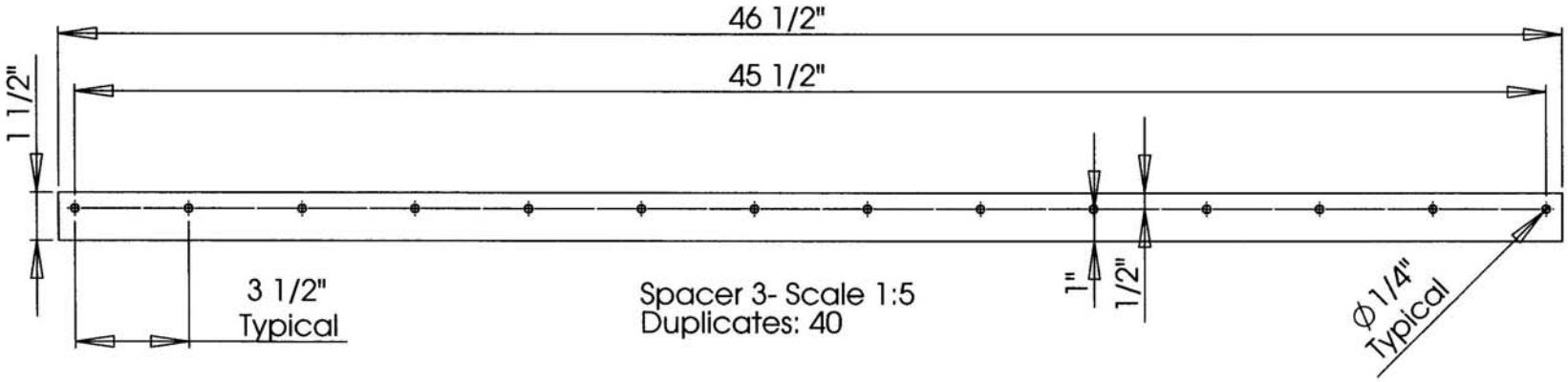

Spacer 3- Scale 1:5
Duplicates: 40

Note: There are three different parts on this drawing. The construction material is 1/16" plate Delrin for all three.

UNLESS OTHERWISE SPECIFIED:		NAME	DATE
DIMENSIONS ARE IN INCHES TOLERANCES: FRACTIONAL ±1/32" ANGULAR: MACH ± BEND ± TWO PLACE DECIMAL ± THREE PLACE DECIMAL ±	DRAWN	DB	21/06/07
	CHECKED		
	ENG APPR.		
	MFG APPR.		
INTERPRET GEOMETRIC TOLERANCING PER:	Q.A.		
MATERIAL: Delrin	Number of Duplicates:		
FINISH: See Drawing			
DO NOT SCALE DRAWING			

TITLE: Inner Components

SIZE	DWG. NO.	REV
A	9	1
SCALE:	SHEET 9 OF 11	

5 4 3 2 1

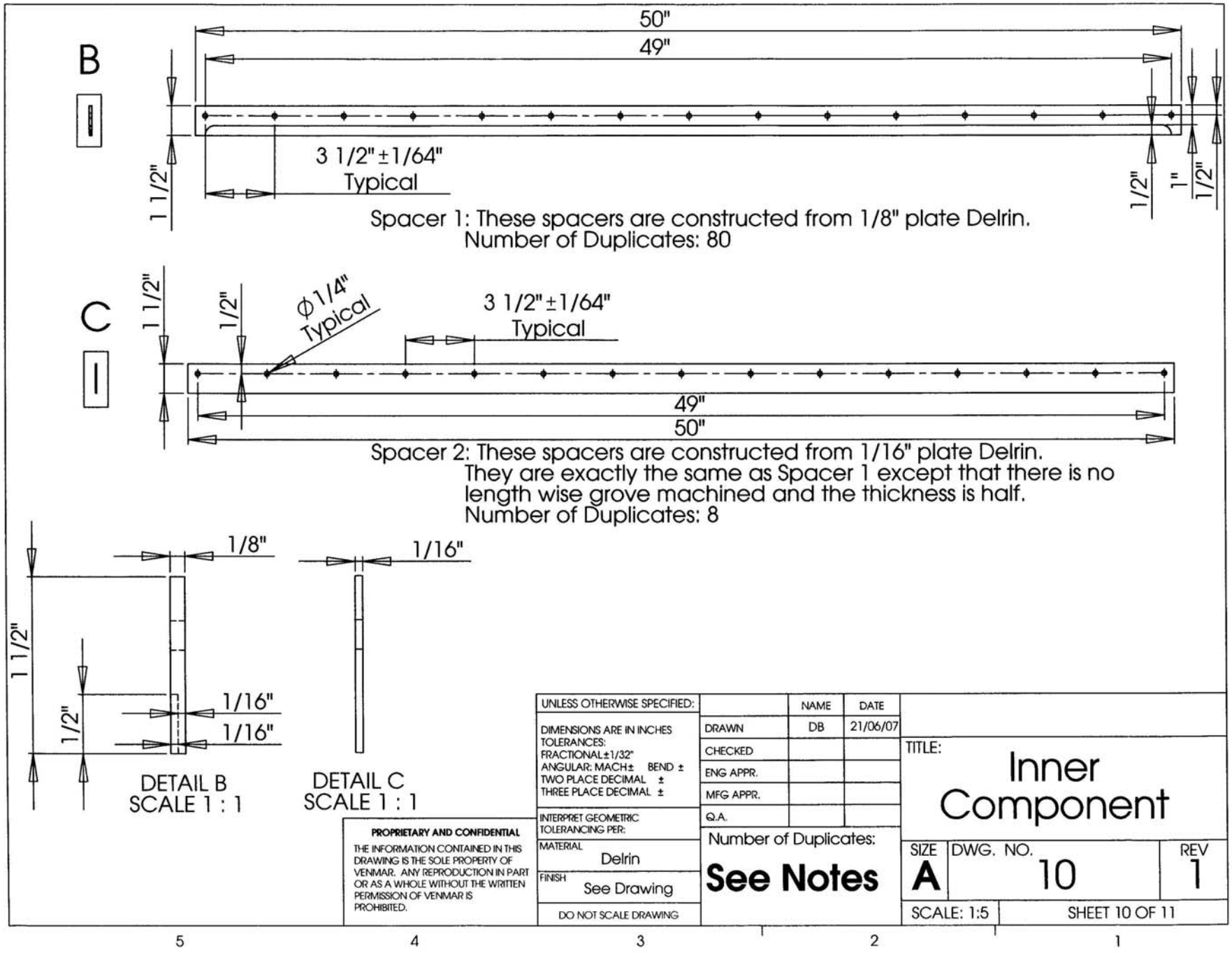
B
50"
49"
3 1/2" ±1/64"
Typical
1 1/2"
1/2"
1"
1/2"
Spacer 1: These spacers are constructed from 1/8" plate Delrin.
Number of Duplicates: 80
C
1 1/2"
1/2"
Φ1/4"
Typical
3 1/2" ±1/64"
Typical
49"
50"
Spacer 2: These spacers are constructed from 1/16" plate Delrin.
They are exactly the same as Spacer 1 except that there is no
length wise grove machined and the thickness is half.
Number of Duplicates: 8
1/8"
1/16"
1 1/2"
1/2"
1/16"
1/16"
DETAIL B
SCALE 1 : 1
DETAIL C
SCALE 1 : 1
UNLESS OTHERWISE SPECIFIED:
DIMENSIONS ARE IN INCHES
TOLERANCES:
FRACTIONAL ±1/32"
ANGULAR: MACH ± BEND ±
TWO PLACE DECIMAL ±
THREE PLACE DECIMAL ±
INTERPRET GEOMETRIC TOLERANCING PER:
MATERIAL
Delrin
FINISH
See Drawing
DO NOT SCALE DRAWING
NAME
DATE
DRAWN
DB
21/06/07
CHECKED
ENG APPR.
MFG APPR.
Q.A.
Number of Duplicates:
See Notes
PROPRIETARY AND CONFIDENTIAL
THE INFORMATION CONTAINED IN THIS DRAWING IS THE SOLE PROPERTY OF VENMAR. ANY REPRODUCTION IN PART OR AS A WHOLE WITHOUT THE WRITTEN PERMISSION OF VENMAR IS PROHIBITED.
TITLE:
Inner Component
SIZE
A
DWG. NO.
10
REV
1
SCALE: 1:5
SHEET 10 OF 11
5
4
3
2
1

General Notes:

Also needed for construction are the following items.
-62x 6"x1/4" corse threaded bolts with nuts.
-50 1/4" ID x 3/4" OD washeers.
-82x1/2" long # 8-32 UNC bolts.
-18x# 8-32 UNC nuts.

UNLESS OTHERWISE SPECIFIED:		NAME	DATE
DIMENSIONS ARE IN INCHES TOLERANCES: FRACTIONAL ±1/32" ANGULAR: MACH ± BEND ± TWO PLACE DECIMAL ± THREE PLACE DECIMAL ±	DRAWN	DB	21/06/07
	CHECKED		
	ENG APPR.		
	MFG APPR.		
INTERPRET GEOMETRIC TOLERANCING PER:	Q.A.		
MATERIAL: Medium Carbon Steel	Number of Duplicates: **60**		
FINISH: See Drawing			
DO NOT SCALE DRAWING			

TITLE: Materials

SIZE	DWG. NO.	REV
A	11	1

SCALE: 1:3 | SHEET 11 OF 11

5 4 3 2 1

APPENDIX F

RAMEE PROTOTYPE 4 SPECIFICATION

The specifications for the membrane used to construct RAMEE prototype 4 are given in Table F.1. All other materials used in the construction of RAMEE prototype 4 are given in Table F.2. The components listed in Table F.2 were built as shown in Appendix E and assembled as shown in Chapter 4.

Table F.1. Specifications for the membrane used in RAMEE prototype 4.

Manufacturer:	AY Technology
Product name:	Laminated PTFE Polytetrafluoroethylene bonded to polyethylene terephthalate
Construction material:	Nonwoven support sub-straight
Characteristic:	Hydrophobic
Cost:	\$35.20/m^2 [\$3.27/ft^2]
Modulus of Rigidity:	(387±32) MPa [(56±5) kPsi]
Vapour Diffusion Resistance:	(97±11) s/m
Permeability:	(6.63±0.8) x 10^{-6} kg/ms
Liquid Penetration Pressure:	>82 kPa [12 Psi], Guaranteed > 34 kPa [5 Psi] by manufacturer
Thickness:	(540±16) µm [(0.0213±0.0006) in.]
Pore size:	0.3 µm [0.00001 in.](Micro-porous)

Table F.2. All other materials used to construct RAMEE prototype 4.

Side Wall Support:	material	6061 Al rectangular tubing
	size	1”x1”x1/16”
	spacing (on center)	14”
	bolts	¼” SAE Grade 1
Side Walls:	material	6061 plate Al
	thickness	3/32”
	bolts	¼” SAE Grade 1
	bolt spacing (on center)	3.5”
Header:	material	Acrylic
	bolts	#8-32 SAE Grade 1
	bolt spacing (on center)	2”
Modules:	Air Spacer	Delrin
	opening spacer	1/16” Core-plast
	glue/sealant	RTV 1000
Inner Screen:	Material	Heavy Felt
	Cost	$\$8.00/m^2$
Outer Screen:	Material	1/2"x1/2" Hardware Cloth
	Cost	$\$16.50/m^2$
Desiccant:	Salt	$MgCl_2$

APPENDIX G

PRESSURE TESING APPARATUS DRAWINGS

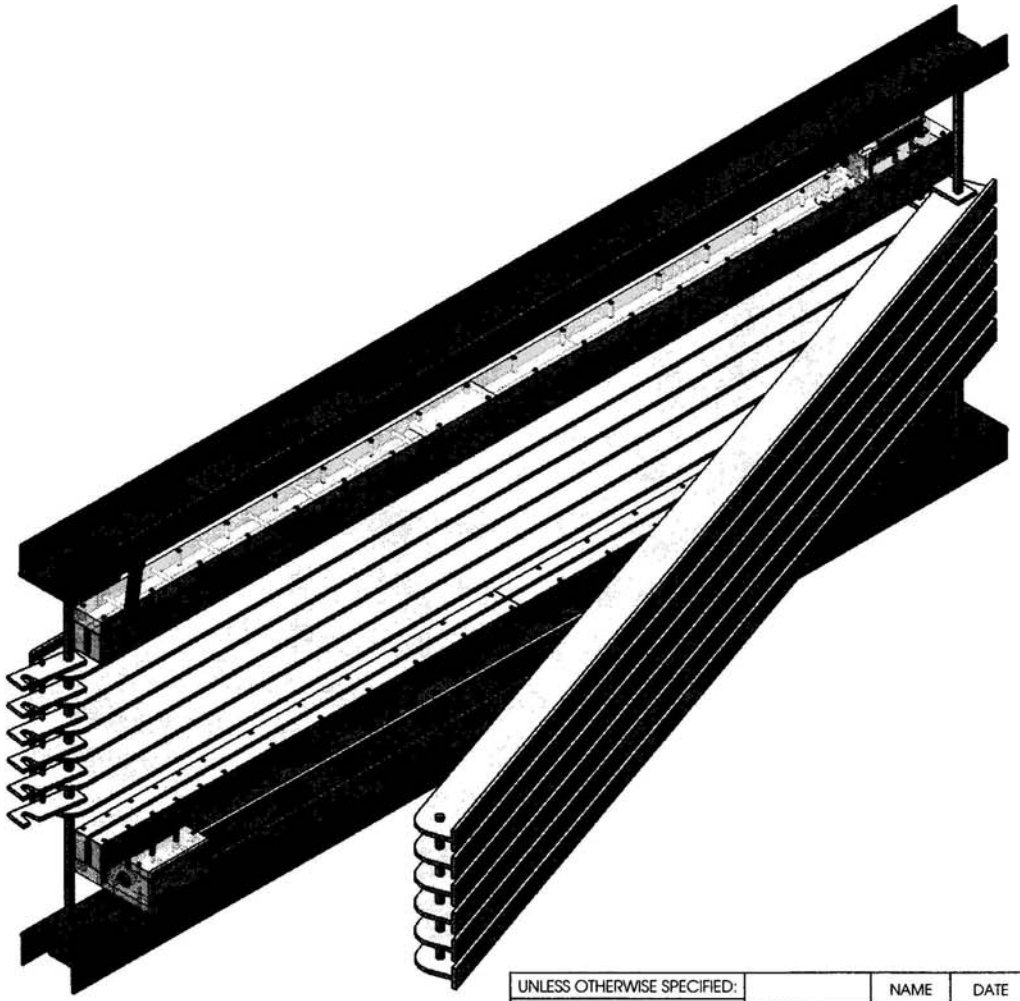

UNLESS OTHERWISE SPECIFIED:		NAME	DATE
DIMENSIONS ARE IN INCHES TOLERANCES: FRACTIONAL ± ANGULAR: MACH ± BEND ± TWO PLACE DECIMAL ± THREE PLACE DECIMAL ±	DRAWN	DB	21/06/07
	CHECKED		
	ENG APPR.		
	MFG APPR.		
	Q.A.		

TITLE: Apparatus

INTERPRET GEOMETRIC TOLERANCING PER:	Number of Duplicates: N/A
MATERIAL N/A	
FINISH See Drawing	
DO NOT SCALE DRAWING	

SIZE	DWG. NO.	REV
A	1	1
SCALE: 1:8	SHEET 1 OF 19	

5 4 3 2 1

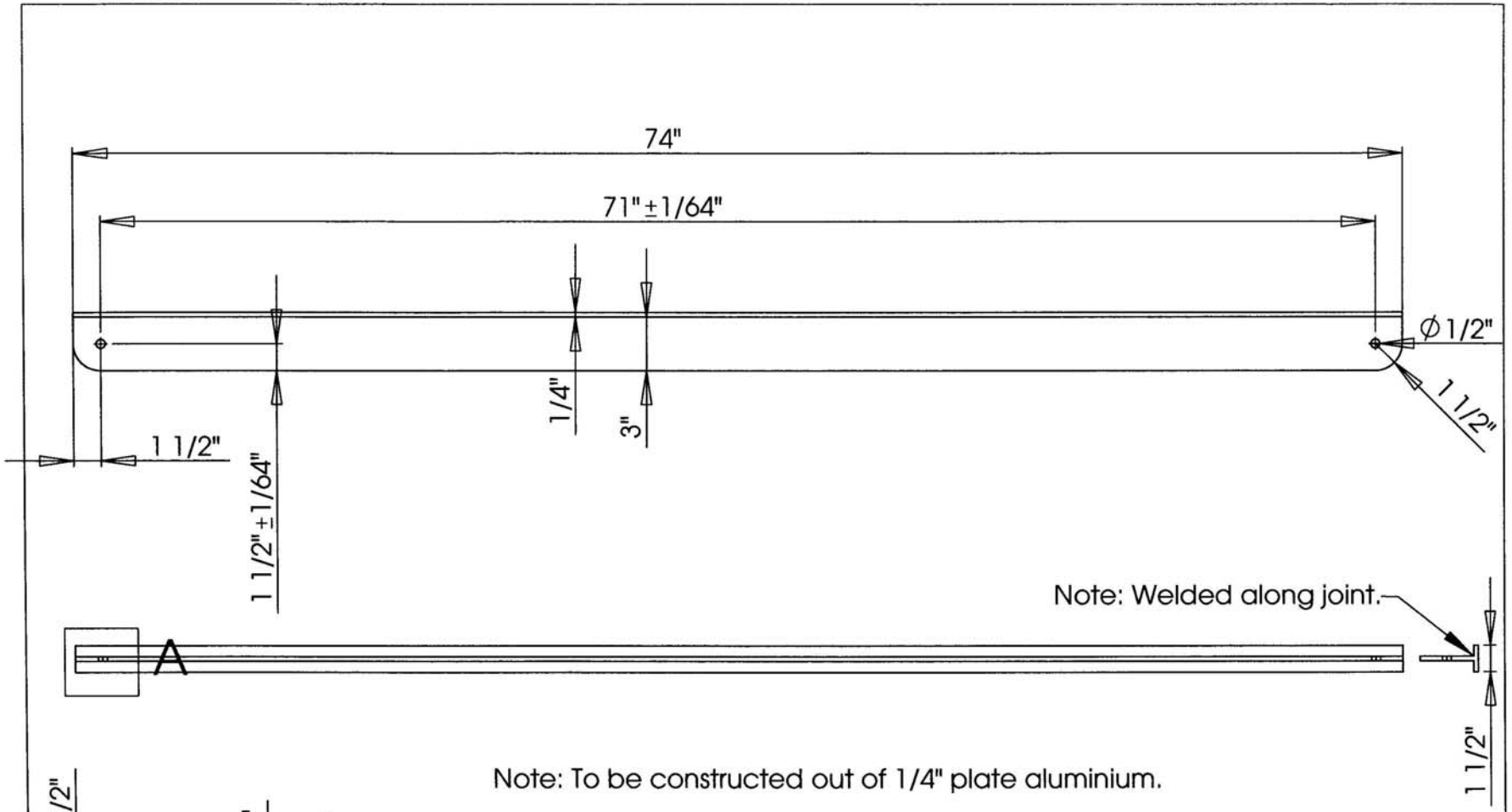

		NAME	DATE
UNLESS OTHERWISE SPECIFIED:	DRAWN	DB	21/06/07
DIMENSIONS ARE IN INCHES TOLERANCES: FRACTIONAL ±1/32" ANGULAR: MACH ± BEND ± TWO PLACE DECIMAL ± THREE PLACE DECIMAL ±	CHECKED		
	ENG APPR.		
	MFG APPR.		
INTERPRET GEOMETRIC TOLERANCING PER:	Q.A.		
MATERIAL 6061 Aluminium	Number of Duplicates: 12		
FINISH See Drawing			
DO NOT SCALE DRAWING			

PROPRIETARY AND CONFIDENTIAL

THE INFORMATION CONTAINED IN THIS DRAWING IS THE SOLE PROPERTY OF VENMAR. ANY REPRODUCTION IN PART OR AS A WHOLE WITHOUT THE WRITTEN PERMISSION OF VENMAR IS PROHIBITED.

TITLE: **Supports**

SIZE	DWG. NO.	REV
A	2	1
SCALE: 1:8	SHEET 2 OF 19	

5 4 3 2 1

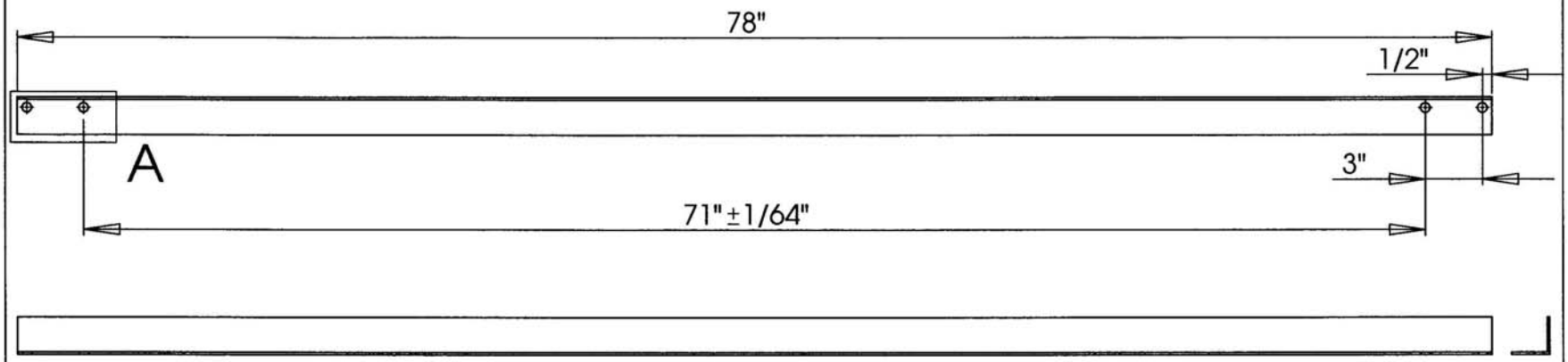

Note: 2"x2"x1/8" Angle Aluminium

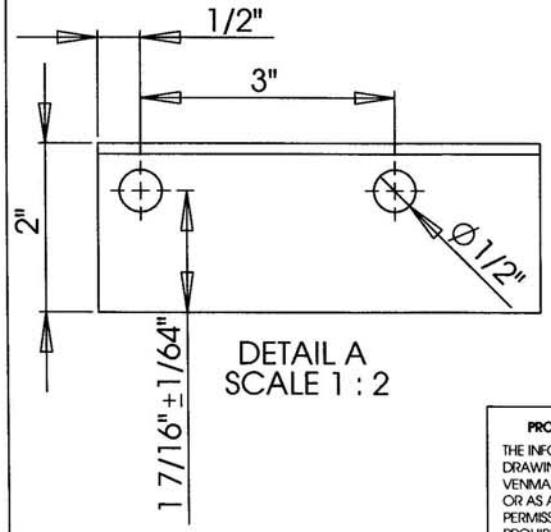

DETAIL A
SCALE 1 : 2

UNLESS OTHERWISE SPECIFIED:		NAME	DATE
DIMENSIONS ARE IN INCHES TOLERANCES: FRACTIONAL ±1/32" ANGULAR: MACH ± BEND ± TWO PLACE DECIMAL ± THREE PLACE DECIMAL ±	DRAWN	DB	21/06/07
	CHECKED		
	ENG APPR.		
	MFG APPR.		
INTERPRET GEOMETRIC TOLERANCING PER:	Q.A.		
MATERIAL 6061 Aluminium	Number of Duplicates: 4		
FINISH See Drawing			
DO NOT SCALE DRAWING			

PROPRIETARY AND CONFIDENTIAL
THE INFORMATION CONTAINED IN THIS DRAWING IS THE SOLE PROPERTY OF VENMAR. ANY REPRODUCTION IN PART OR AS A WHOLE WITHOUT THE WRITTEN PERMISSION OF VENMAR IS PROHIBITED.

TITLE: Header Supports

SIZE	DWG. NO.	REV
A	3	1

SCALE: 1:8 | SHEET 3 OF 19

5 4 3 2 1

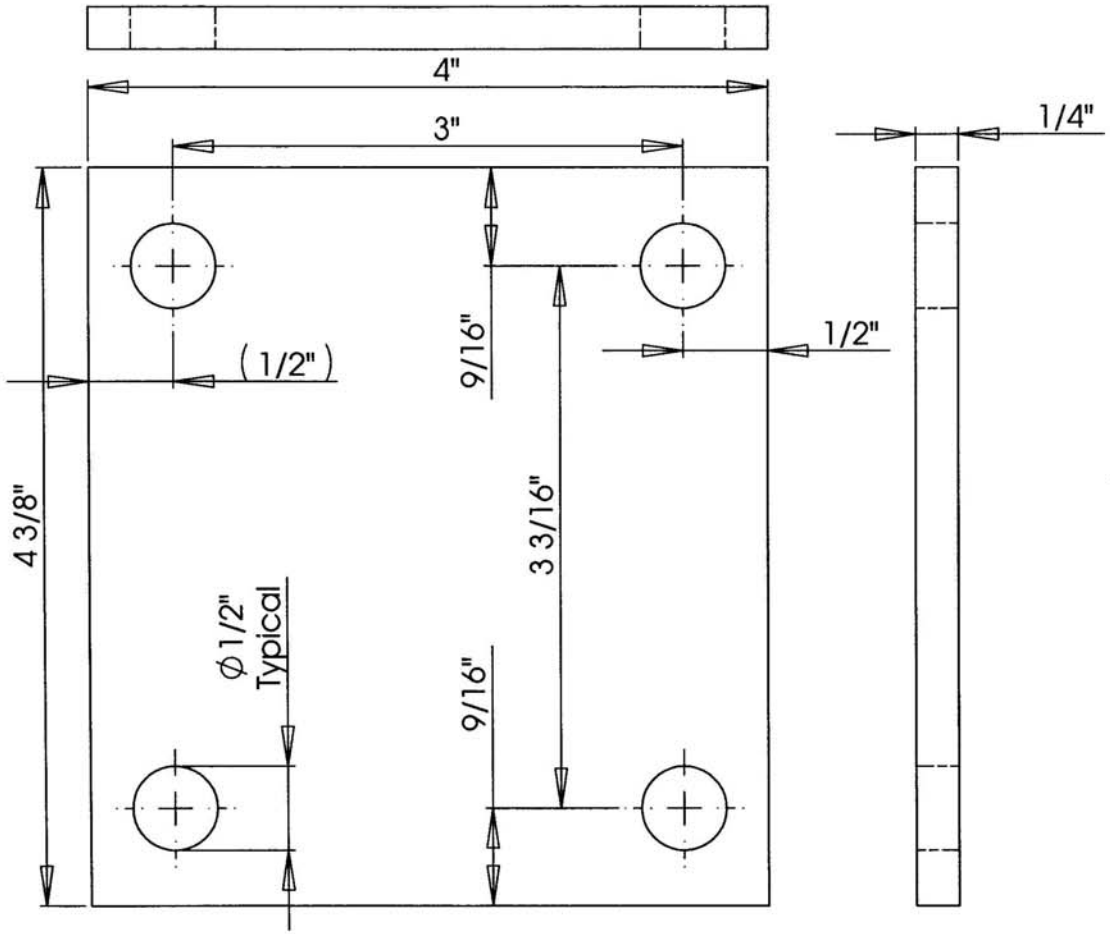

Note: Constructed from 1/4" plate aluiminium.
Number of Duplicates: 4
SCALE: 1:1

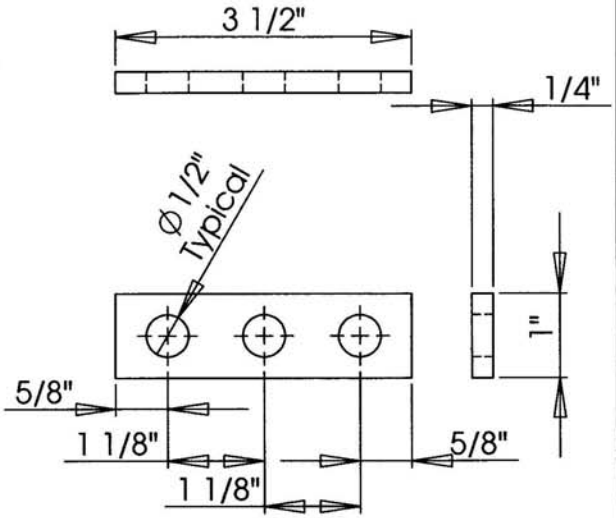

Note: Constructed from 1/4"
plate Aluminium.
Number of Duplicates: 2
SCALE: 1:2

UNLESS OTHERWISE SPECIFIED:		NAME	DATE
DIMENSIONS ARE IN INCHES TOLERANCES: FRACTIONAL ±1/32" ANGULAR: MACH ± BEND ± TWO PLACE DECIMAL ± THREE PLACE DECIMAL ±	DRAWN	DB	21/06/07
	CHECKED		
	ENG APPR.		
	MFG APPR.		
INTERPRET GEOMETRIC TOLERANCING PER:	Q.A.		
MATERIAL 6061 Aluminium	Number of Duplicates: See Drawing		
FINISH See Drawing			
DO NOT SCALE DRAWING			

TITLE: Plates

SIZE	DWG. NO.	REV
A	4	1

SCALE: S.D. | SHEET 4 OF 19

5 4 3 2 1

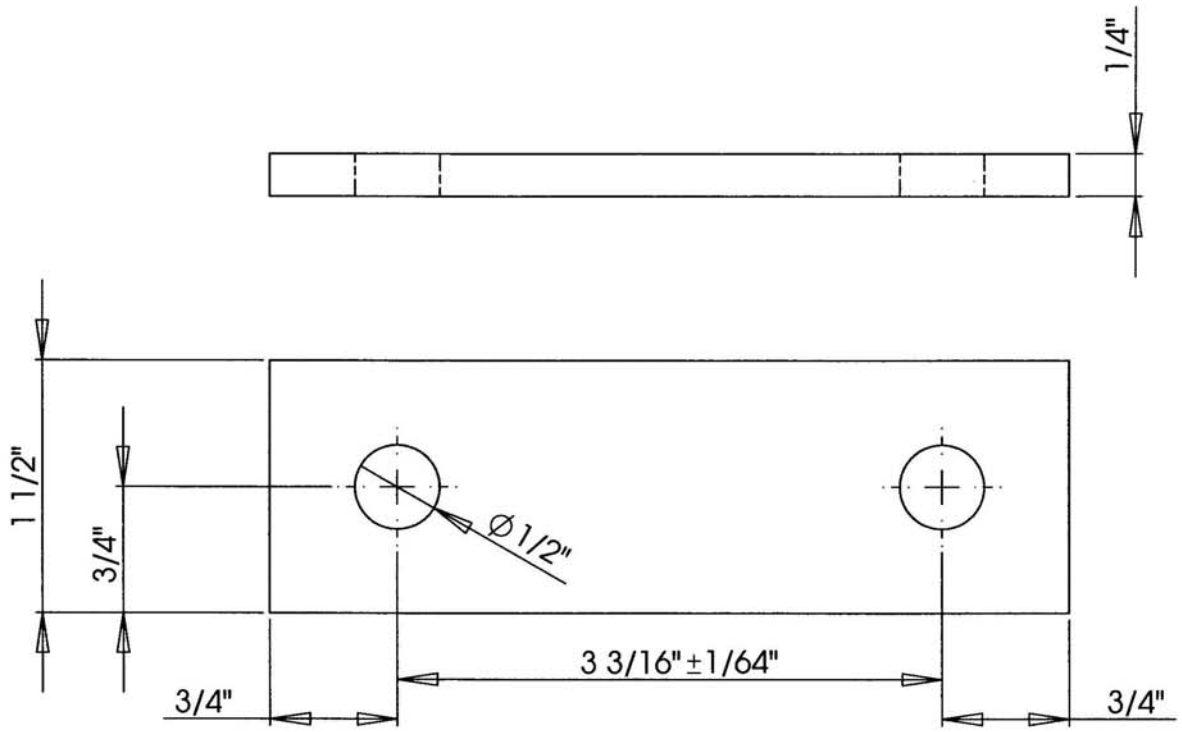

Note: 1/4" plate aluiminium is to be used.

UNLESS OTHERWISE SPECIFIED:		NAME	DATE
DIMENSIONS ARE IN INCHES TOLERANCES: FRACTIONAL ±1/32" ANGULAR: MACH ± BEND ± TWO PLACE DECIMAL ± THREE PLACE DECIMAL ±	DRAWN	DB	21/06/07
	CHECKED		
	ENG APPR.		
	MFG APPR.		
INTERPRET GEOMETRIC TOLERANCING PER:	Q.A.		
MATERIAL 6061 Aluminium	Number of Duplicates: 12		
FINISH See Drawing			
DO NOT SCALE DRAWING			

TITLE: Spacer

SIZE	DWG. NO.	REV
A	5	1

SCALE: 1:1 | SHEET 5 OF 19

5 4 3 2 1

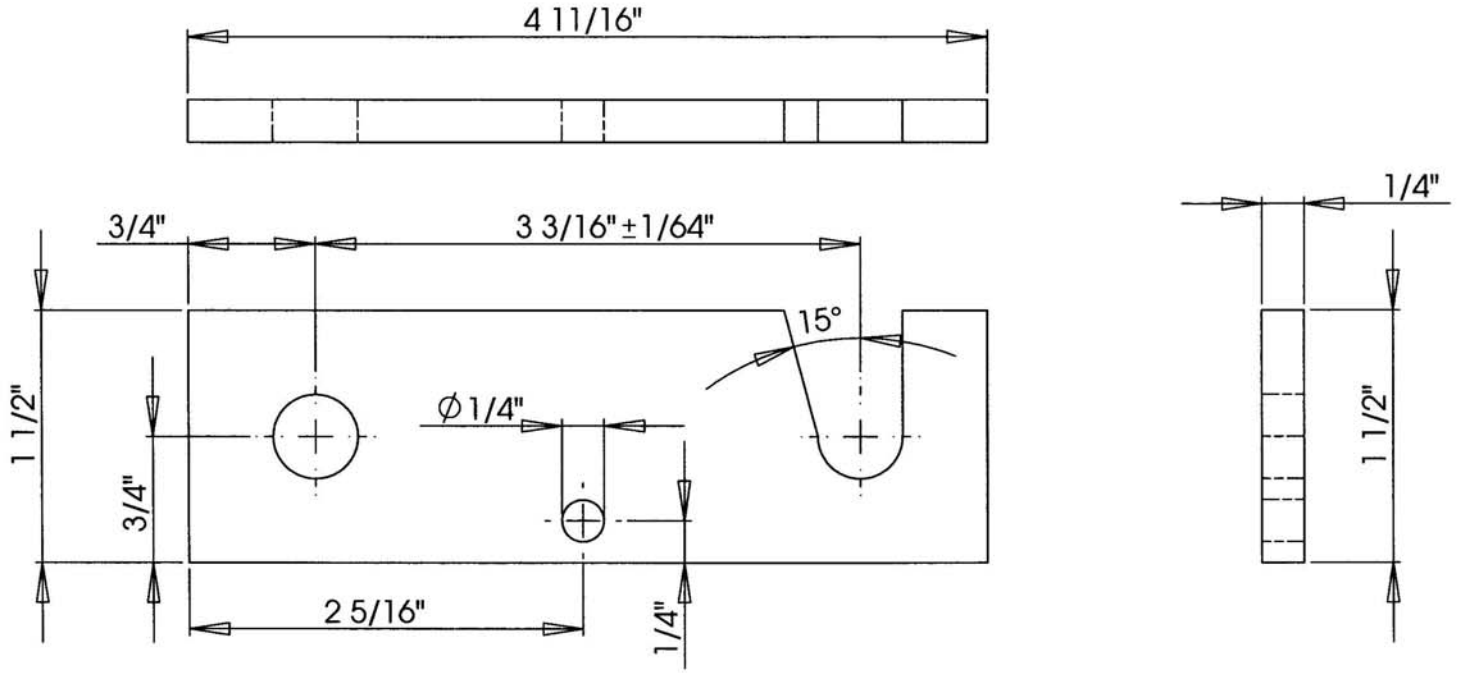

Note: 1/4" plate aluminium is to be used.

UNLESS OTHERWISE SPECIFIED:		NAME	DATE
DIMENSIONS ARE IN INCHES TOLERANCES: FRACTIONAL ±1/32" ANGULAR: MACH ± BEND ± TWO PLACE DECIMAL ± THREE PLACE DECIMAL ±	DRAWN	DB	21/06/07
	CHECKED		
	ENG APPR.		
	MFG APPR.		
INTERPRET GEOMETRIC TOLERANCING PER:	Q.A.		
MATERIAL 6061 Aluminium	Number of Duplicates: 12		
FINISH See Drawing			
DO NOT SCALE DRAWING			

TITLE: Spacer 1

SIZE	DWG. NO.	REV
A	6	1

SCALE: 1:1 | SHEET 6 OF 19

5 4 3 2 1

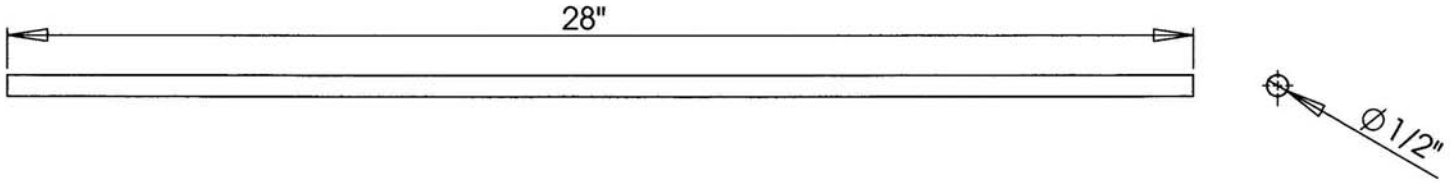

Note: Entire Length Threaded with 1/2" Standard Threading
Number of Duplicates: 4

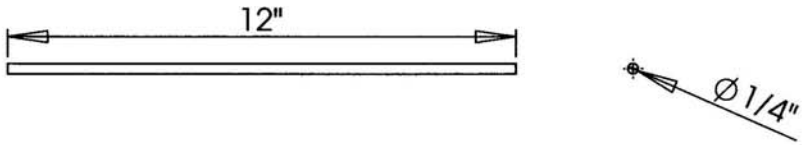

Note: Entire Length Threaded with 1/4" Standard Threading
Number of Duplicates: 1

UNLESS OTHERWISE SPECIFIED:		NAME	DATE
DIMENSIONS ARE IN INCHES TOLERANCES: FRACTIONAL ±1/32" ANGULAR: MACH ± BEND ± TWO PLACE DECIMAL ± THREE PLACE DECIMAL ±	DRAWN	DB	21/06/07
	CHECKED		
	ENG APPR.		
	MFG APPR.		
	Q.A.		
INTERPRET GEOMETRIC TOLERANCING PER:	Number of Duplicates: See Drawing		
MATERIAL: Medium Carbon Steel			
FINISH: See Drawing			
DO NOT SCALE DRAWING			

TITLE: Rods

SIZE	DWG. NO.	REV
A	7	1

SCALE: 1:4 | SHEET 7 OF 19

5 4 3 2 1

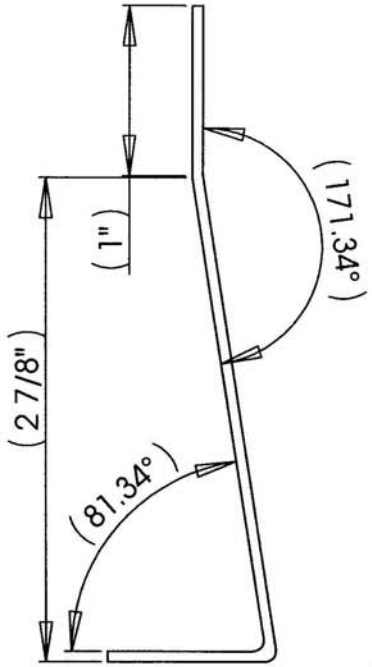

Note: To be constructed out of 1"x5"x1/16" plate aluminium.

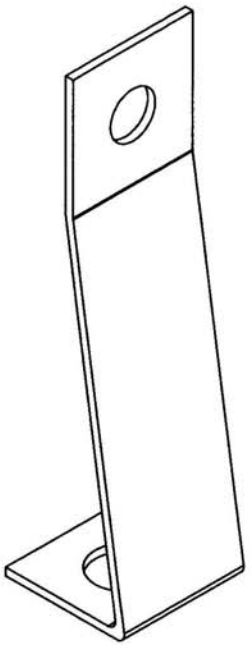

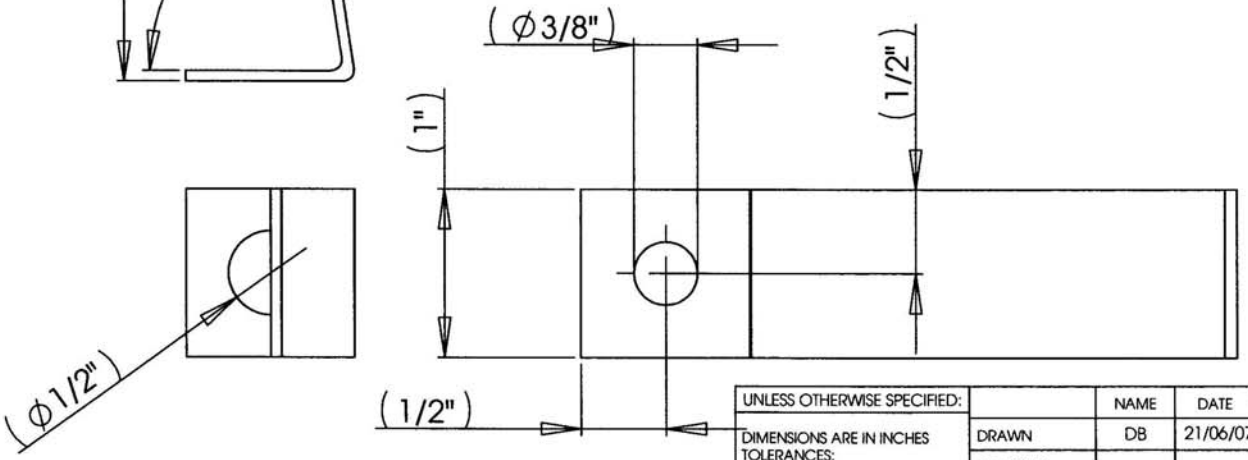

UNLESS OTHERWISE SPECIFIED:		NAME	DATE
DIMENSIONS ARE IN INCHES TOLERANCES: FRACTIONAL ±1/32" ANGULAR: MACH ± BEND ± TWO PLACE DECIMAL ± THREE PLACE DECIMAL ±	DRAWN	DB	21/06/07
	CHECKED		
	ENG APPR.		
	MFG APPR.		
	Q.A.		
INTERPRET GEOMETRIC TOLERANCING PER:			
MATERIAL: 6061 Aluminum	Number of Duplicates: 4		
FINISH: See Drawing			
DO NOT SCALE DRAWING			

TITLE: Additional Header Supports

SIZE	DWG. NO.	REV
A	8	1

SCALE: 1:1 | SHEET 8 OF 19

5 4 3 2 1

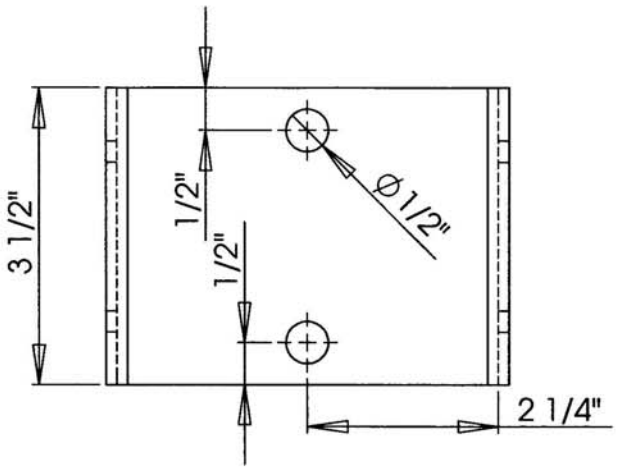

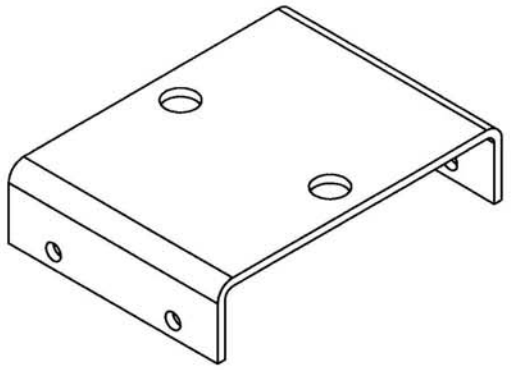

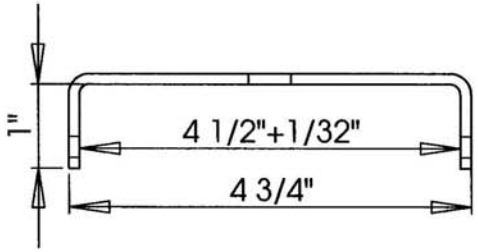

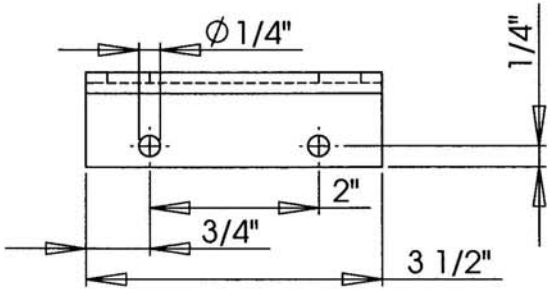

Note: Formed from 1/8" plate Aluminium.

		NAME	DATE
UNLESS OTHERWISE SPECIFIED:			
DIMENSIONS ARE IN INCHES TOLERANCES: FRACTIONAL ±1/32" ANGULAR: MACH ± BEND ± TWO PLACE DECIMAL ± THREE PLACE DECIMAL ±	DRAWN	DB	21/06/07
	CHECKED		
	ENG APPR.		
	MFG APPR.		
	Q.A.		
INTERPRET GEOMETRIC TOLERANCING PER:			
MATERIAL 6061 Aluminium	Number of Duplicates: 2		
FINISH See Drawing			
DO NOT SCALE DRAWING			

TITLE: Attachment Bracket

SIZE	DWG. NO.	REV
A	9	1

SCALE: 1:1 | SHEET 9 OF 19

5 4 3 2 1

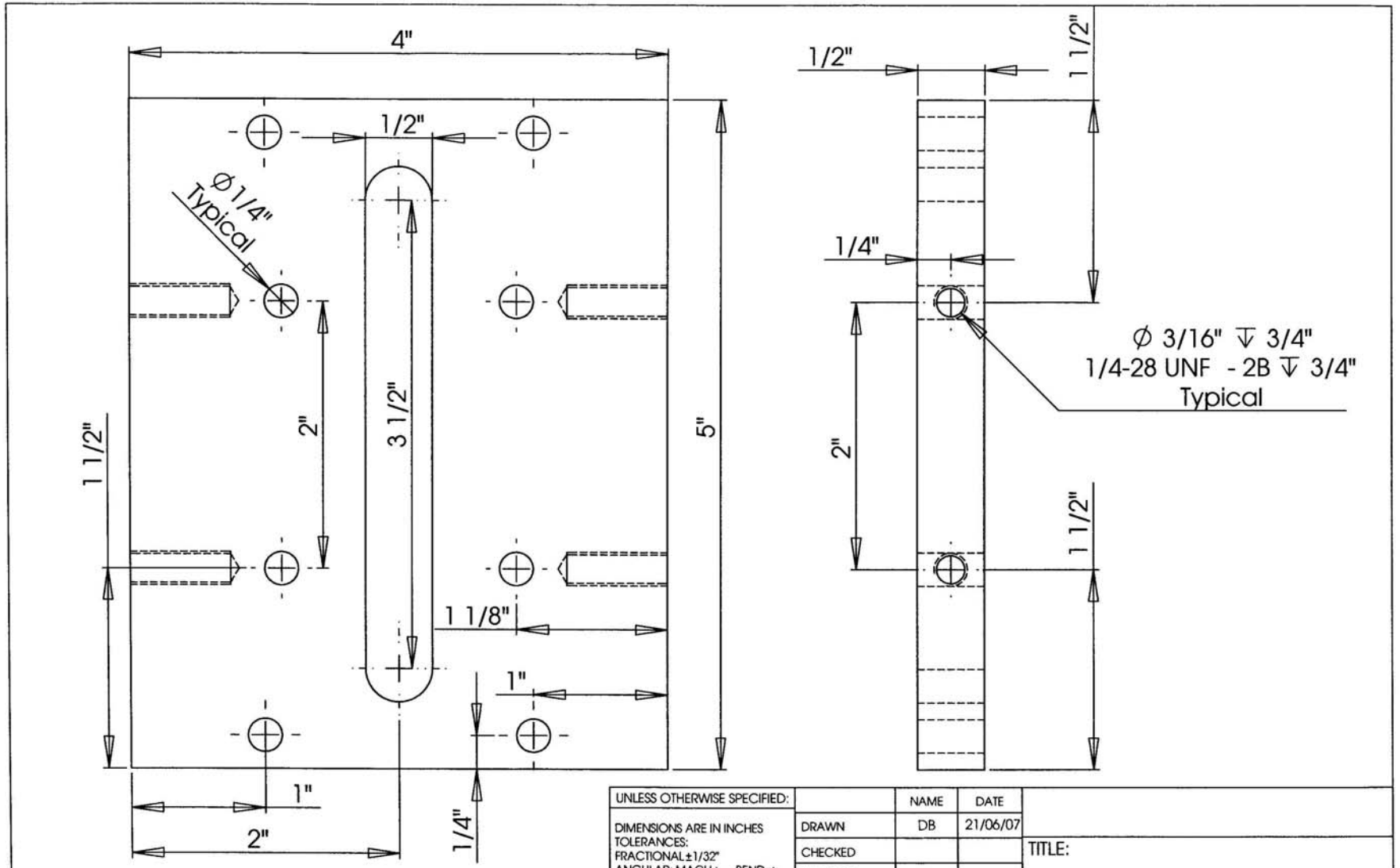

		NAME	DATE
UNLESS OTHERWISE SPECIFIED:			
DIMENSIONS ARE IN INCHES TOLERANCES: FRACTIONAL ±1/32" ANGULAR: MACH ± BEND ± TWO PLACE DECIMAL ± THREE PLACE DECIMAL ±	DRAWN	DB	21/06/07
	CHECKED		
	ENG APPR.		
	MFG APPR.		
INTERPRET GEOMETRIC TOLERANCING PER:	Q.A.		
MATERIAL: Acrylic	Number of Duplicates: 2		
FINISH: See Drawing			
DO NOT SCALE DRAWING			

TITLE: Bottom

SIZE	DWG. NO.	REV
A	10	1

SCALE: 1:1 | SHEET 10 OF 19

5 4 3 2 1

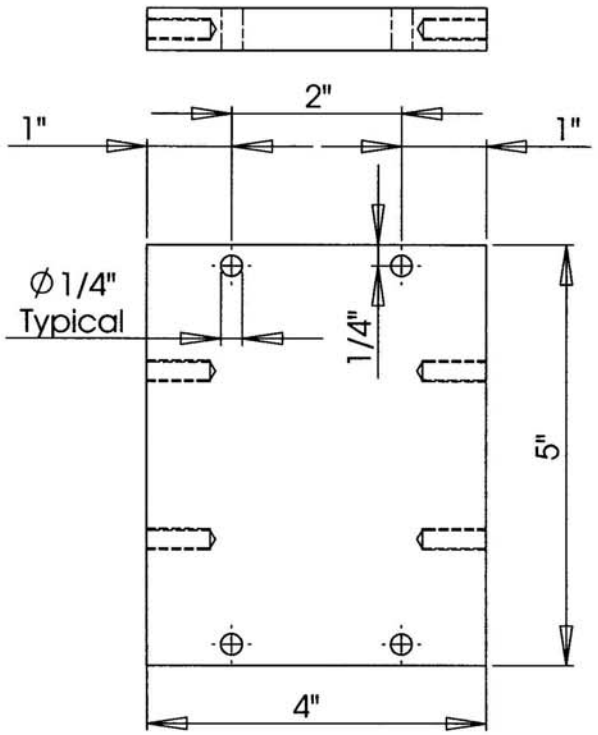

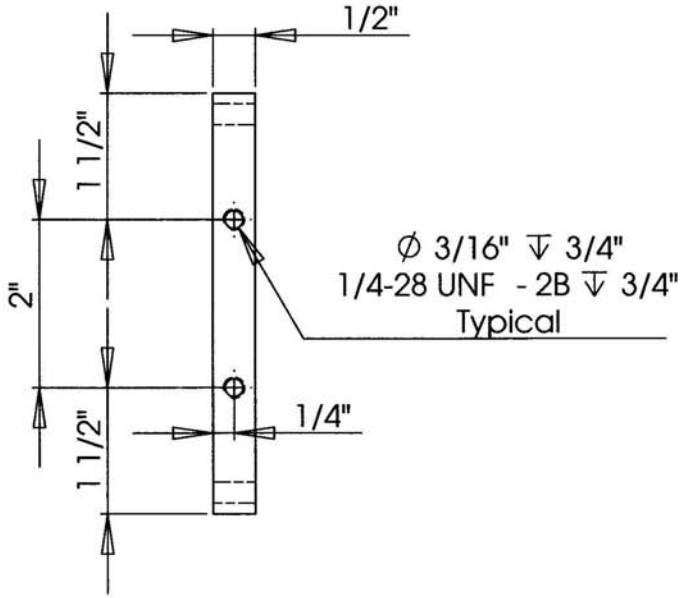

UNLESS OTHERWISE SPECIFIED:		NAME	DATE
DIMENSIONS ARE IN INCHES TOLERANCES: FRACTIONAL ±1/32" ANGULAR: MACH ± BEND ± TWO PLACE DECIMAL ± THREE PLACE DECIMAL ±	DRAWN	DB	21/06/07
	CHECKED		
	ENG APPR.		
	MFG APPR.		
INTERPRET GEOMETRIC TOLERANCING PER:	Q.A.		
MATERIAL: Acrylic	Number of Duplicates: 2		
FINISH: See Drawing			
DO NOT SCALE DRAWING			

TITLE: Top

SIZE	DWG. NO.	REV
A	11	1

SCALE: 1:2 | SHEET 11 OF 19

5 4 3 2 1

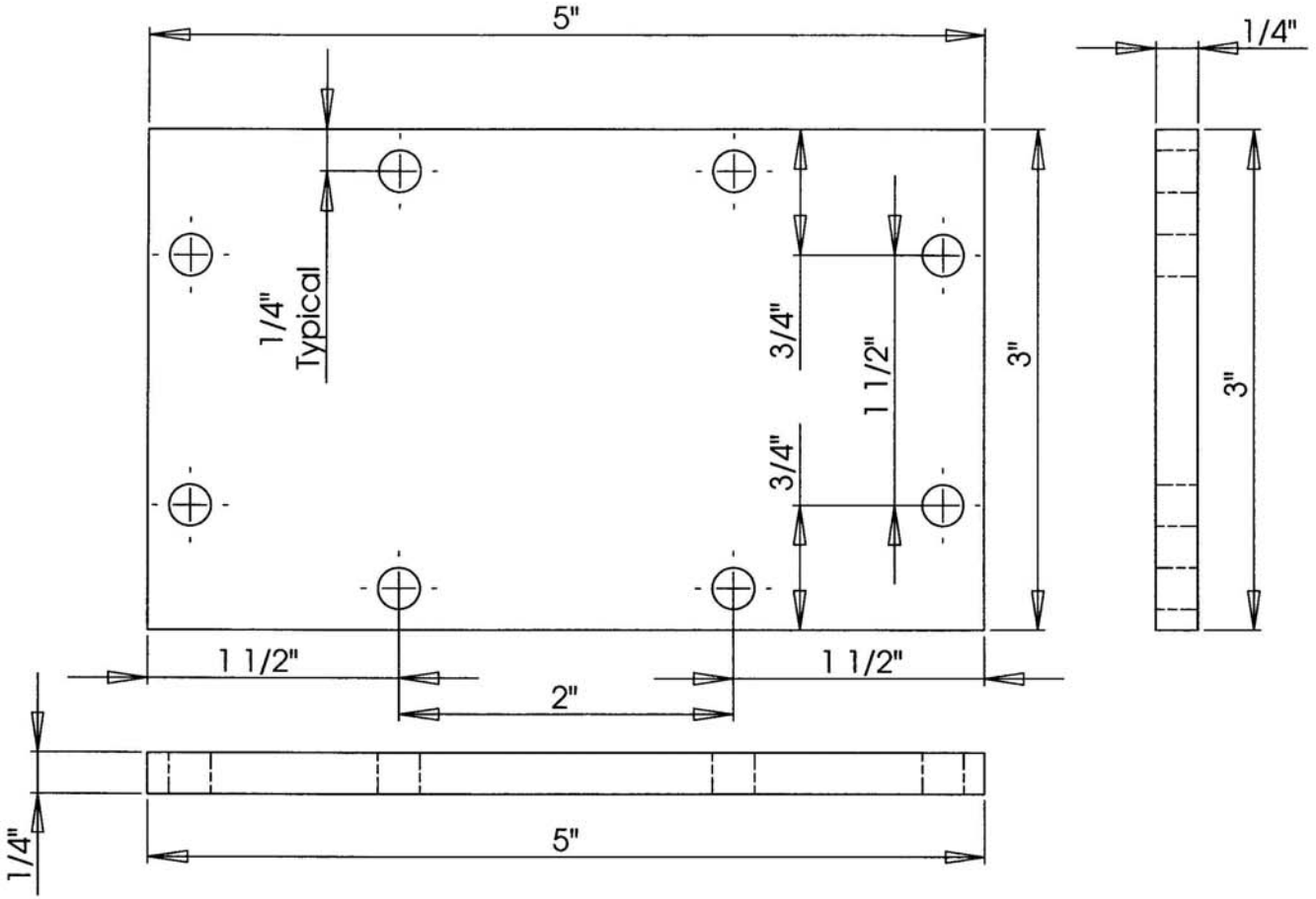

UNLESS OTHERWISE SPECIFIED:		NAME	DATE
DIMENSIONS ARE IN INCHES TOLERANCES: FRACTIONAL ±1/32" ANGULAR: MACH ± BEND ± TWO PLACE DECIMAL ± THREE PLACE DECIMAL ±	DRAWN	DB	21/06/07
	CHECKED		
	ENG APPR.		
	MFG APPR.		
	Q.A.		
INTERPRET GEOMETRIC TOLERANCING PER:	Number of Duplicates: **4**		
MATERIAL: Acrylic			
FINISH: See Drawing			
DO NOT SCALE DRAWING			

TITLE: **Front/Back**

SIZE	DWG. NO.	REV
A	12	1

SCALE: 1:1 | SHEET 12 OF 19

5 4 3 2 1

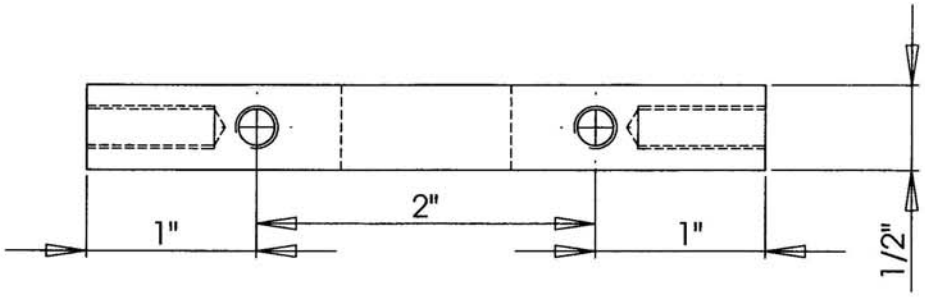

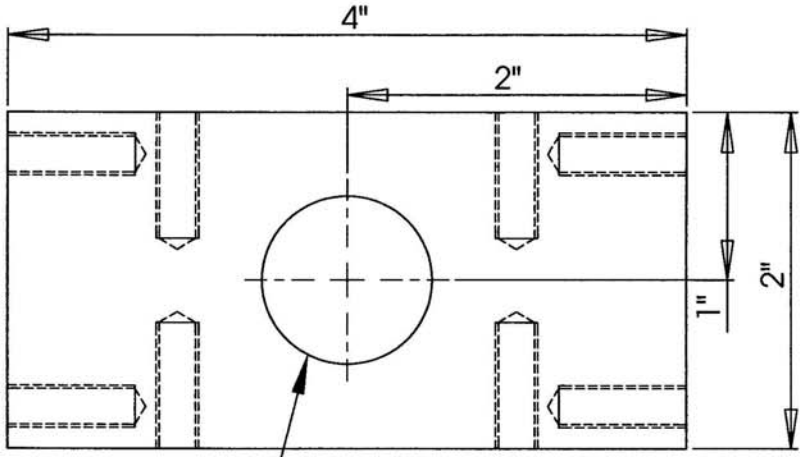

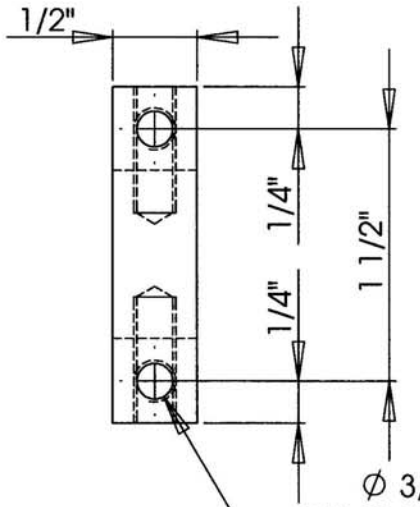

Note: Standard 3/4" Taperred Garden Hose Threading

Ø 3/16" ↧ 3/4"
1/4-28 UNF - 2B ↧ 3/4"
Typical

UNLESS OTHERWISE SPECIFIED:		NAME	DATE
DIMENSIONS ARE IN INCHES TOLERANCES: FRACTIONAL ±1/32" ANGULAR: MACH ± BEND ± TWO PLACE DECIMAL ± THREE PLACE DECIMAL ±	DRAWN	DB	21/06/07
	CHECKED		
	ENG APPR.		
	MFG APPR.		
	Q.A.		
INTERPRET GEOMETRIC TOLERANCING PER:			
MATERIAL: Acrylic			
FINISH: See Drawing			
DO NOT SCALE DRAWING			

TITLE: Sides

Number of Duplicates: 4

SIZE	DWG. NO.	REV
A	13	1

SCALE: 1:1 | SHEET 13 OF 19

5 4 3 2 1

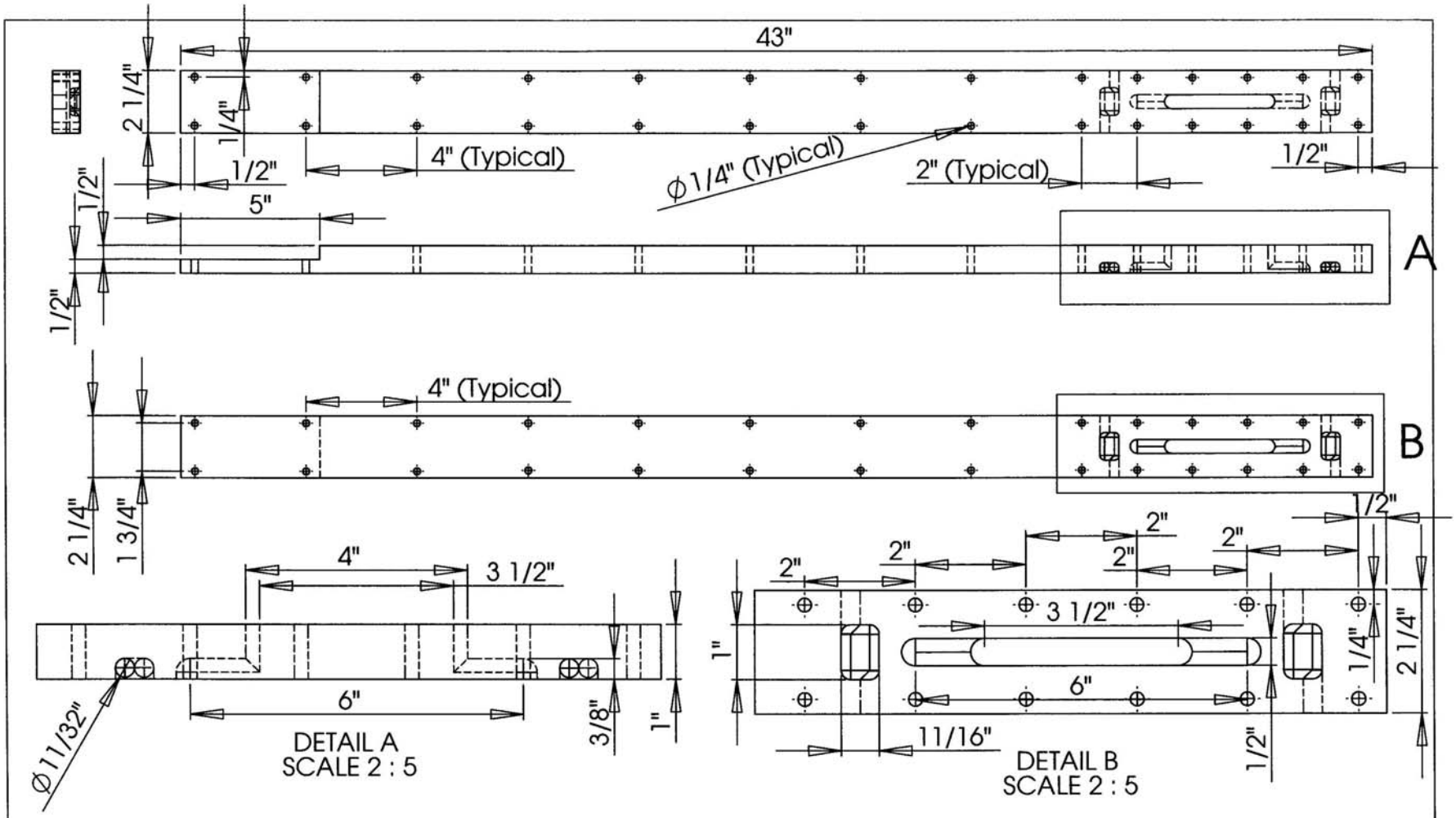

UNLESS OTHERWISE SPECIFIED:		NAME	DATE
DIMENSIONS ARE IN INCHES TOLERANCES: FRACTIONAL ±1/32" ANGULAR: MACH ± BEND ± TWO PLACE DECIMAL ± THREE PLACE DECIMAL ±	DRAWN	DB	21/06/07
	CHECKED		
	ENG APPR.		
	MFG APPR.		
	Q.A.		
INTERPRET GEOMETRIC TOLERANCING PER:	Number of Duplicates:		
MATERIAL: Acrylic	**2**		
FINISH: See Drawing			
DO NOT SCALE DRAWING			

TITLE: **Header 1 Revision**

SIZE	DWG. NO.	REV
A	14	2
SCALE: 1:5	SHEET 14 OF 19	

5 4 3 2 1

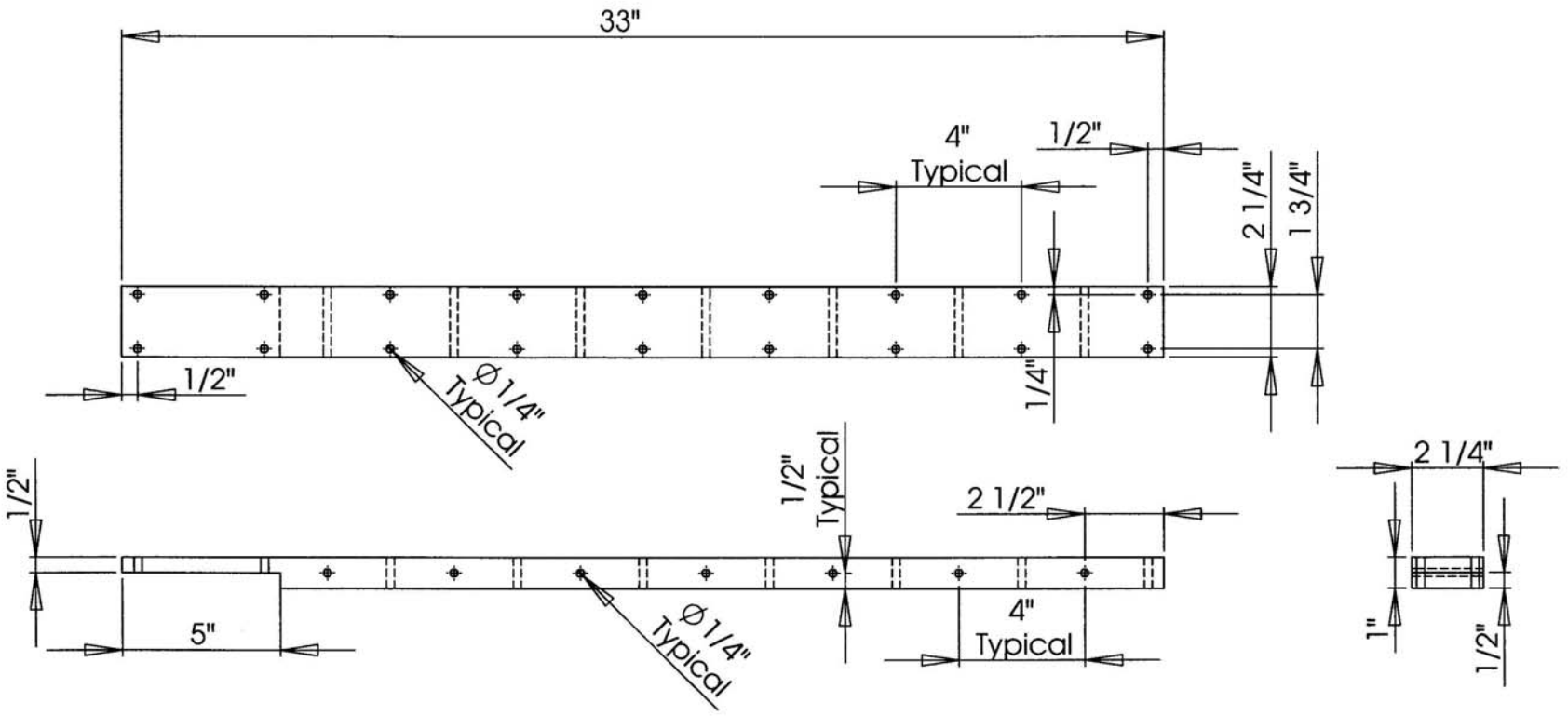

UNLESS OTHERWISE SPECIFIED:		NAME	DATE
DIMENSIONS ARE IN INCHES TOLERANCES: FRACTIONAL ±1/32" ANGULAR: MACH ± BEND ± TWO PLACE DECIMAL ± THREE PLACE DECIMAL ±	DRAWN	DB	21/06/07
	CHECKED		
	ENG APPR.		
	MFG APPR.		
INTERPRET GEOMETRIC TOLERANCING PER:	Q.A.		
MATERIAL: Acrylic	Number of Duplicates: **2**		
FINISH: See Drawing			
DO NOT SCALE DRAWING			

TITLE: **Header 2**

SIZE	DWG. NO.	REV
A	15	1

SCALE: 1:5 | SHEET 15 OF 19

5 4 3 2 1

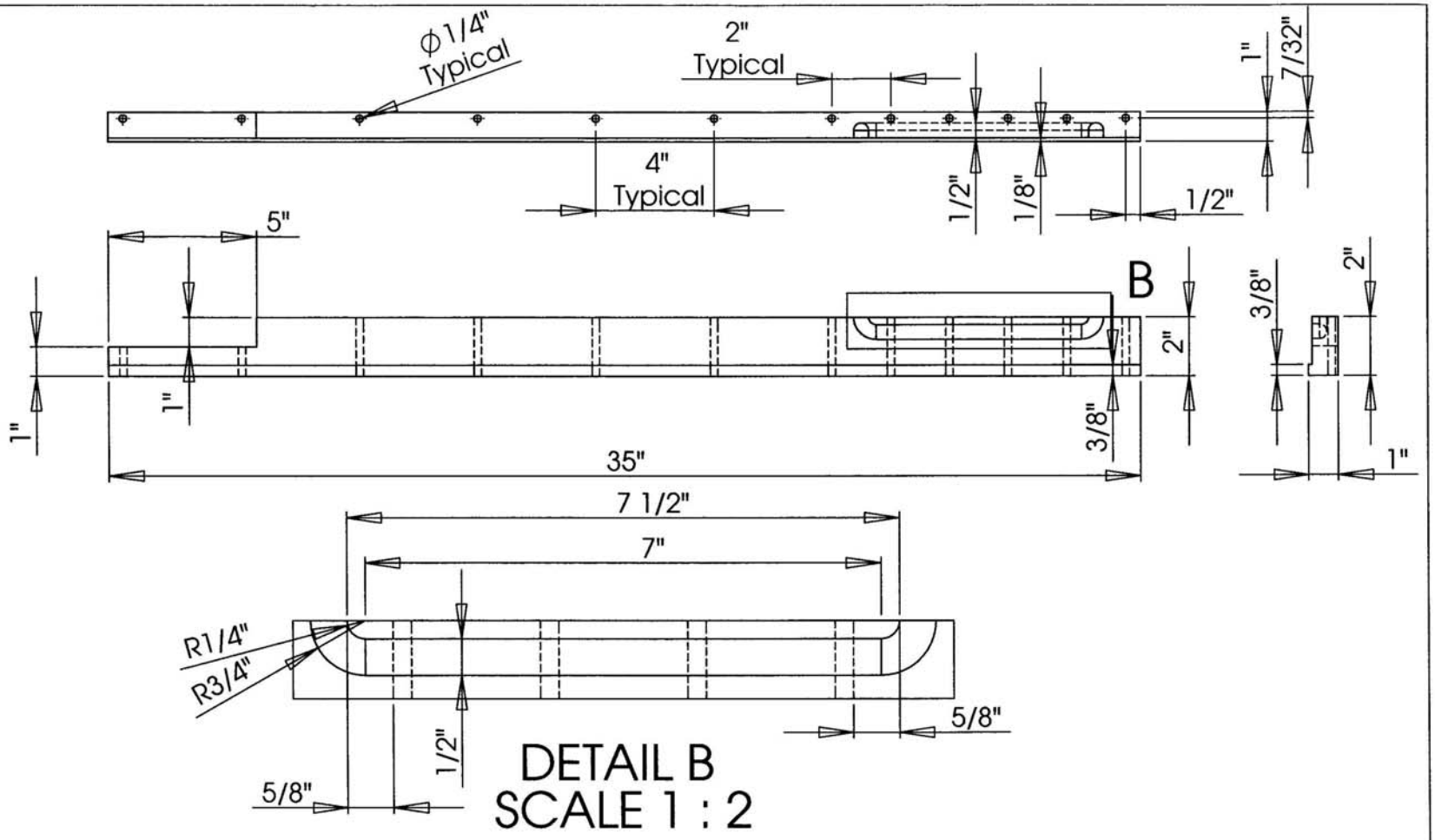

DETAIL B
SCALE 1 : 2

		NAME	DATE
UNLESS OTHERWISE SPECIFIED:	DRAWN	DB	21/06/07
DIMENSIONS ARE IN INCHES TOLERANCES: FRACTIONAL ±1/32" ANGULAR: MACH ± BEND ± TWO PLACE DECIMAL ± THREE PLACE DECIMAL ±	CHECKED		
	ENG APPR.		
	MFG APPR.		
INTERPRET GEOMETRIC TOLERANCING PER:	Q.A.		
MATERIAL: Acrylic	Number of Duplicates: 2		
FINISH: See Drawing			
DO NOT SCALE DRAWING			

TITLE: Runner 1

SIZE	DWG. NO.	REV
A	16	1

SCALE: 1:5 | SHEET 16 OF 19

5 4 3 2 1

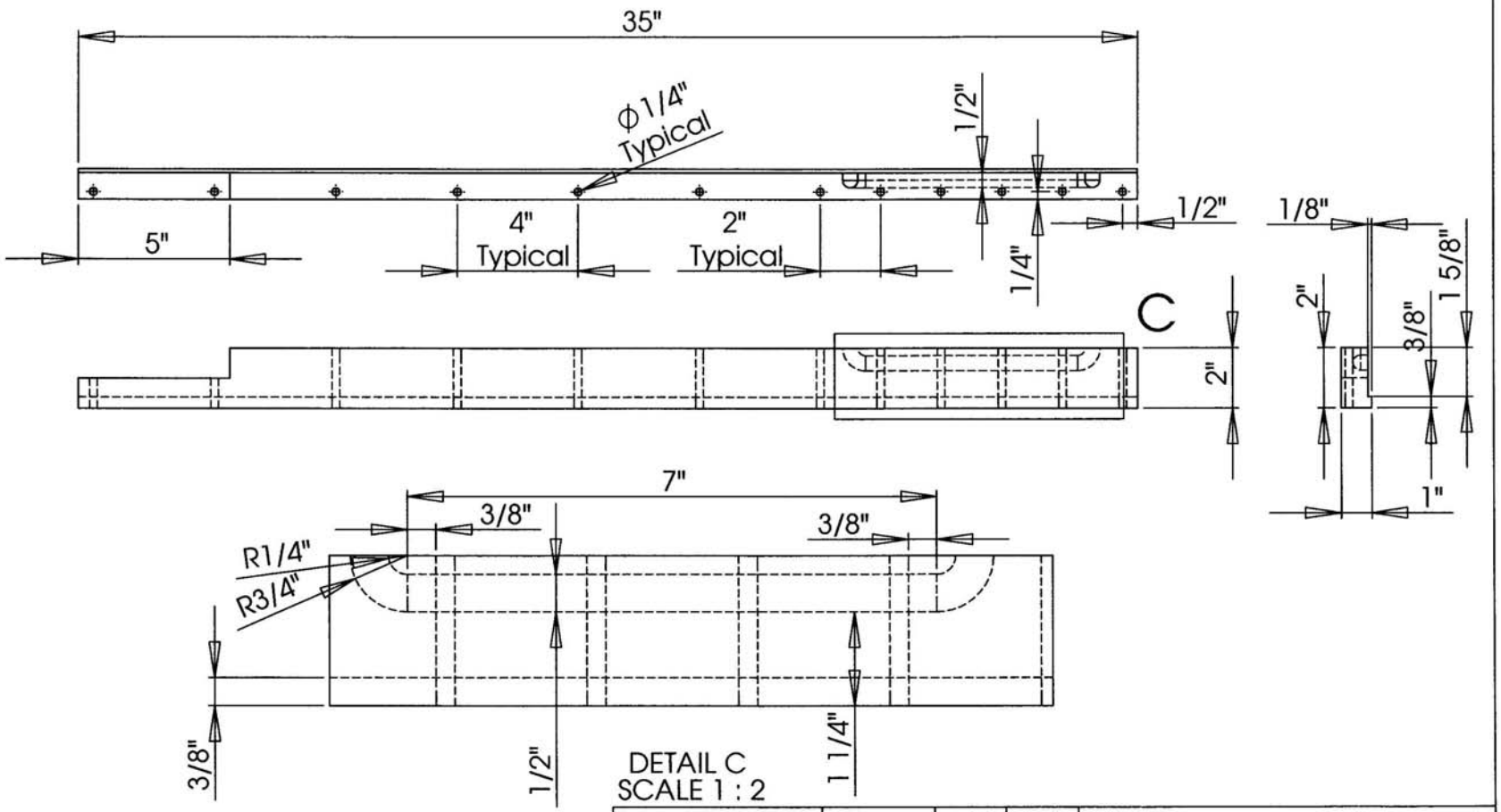

DETAIL C
SCALE 1 : 2

UNLESS OTHERWISE SPECIFIED:		NAME	DATE
DIMENSIONS ARE IN INCHES TOLERANCES: FRACTIONAL ±1/32" ANGULAR: MACH ± BEND ± TWO PLACE DECIMAL ± THREE PLACE DECIMAL ±	DRAWN	DB	21/06/07
	CHECKED		
	ENG APPR.		
	MFG APPR.		
	Q.A.		
INTERPRET GEOMETRIC TOLERANCING PER:			
MATERIAL: Acrylic			
FINISH: See Drawing			
DO NOT SCALE DRAWING			

Number of Duplicates: **2**

TITLE: **Runner 1-1**

SIZE	DWG. NO.	REV
A	17	1

SCALE: 1:5 | SHEET 17 OF 19

5 4 3 2 1

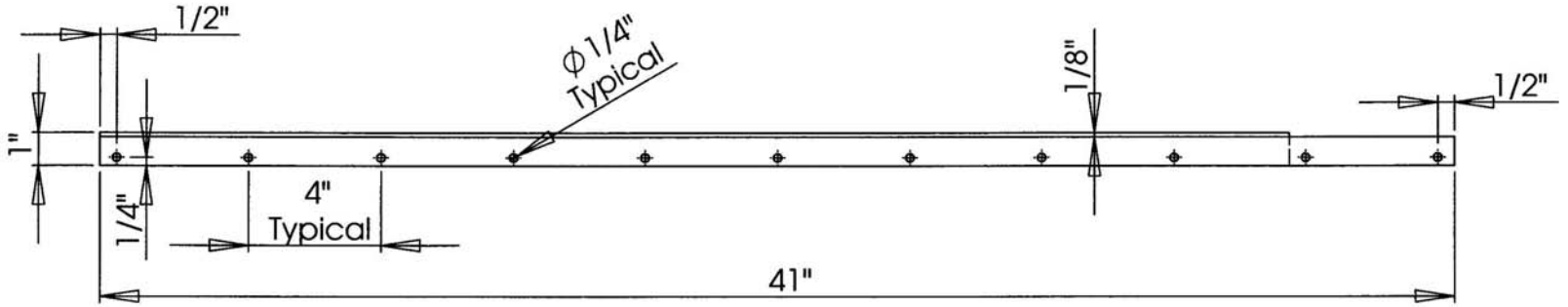

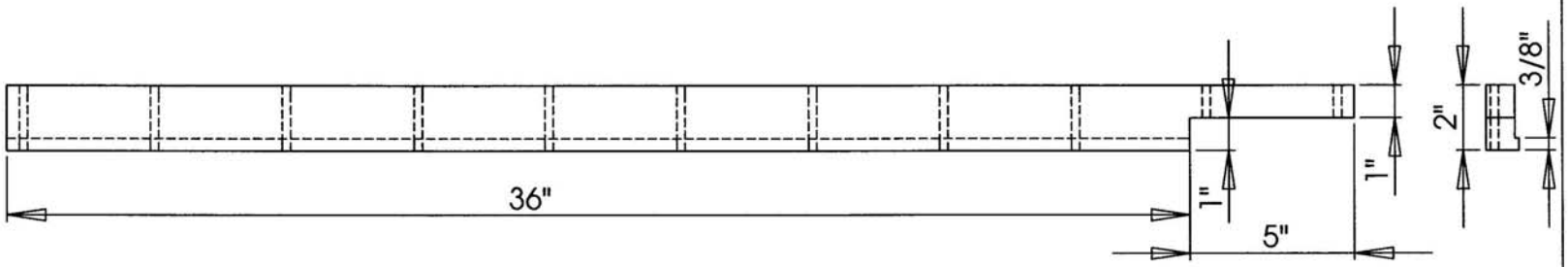

UNLESS OTHERWISE SPECIFIED:		NAME	DATE
DIMENSIONS ARE IN INCHES TOLERANCES: FRACTIONAL ±1/32" ANGULAR: MACH ± BEND ± TWO PLACE DECIMAL ± THREE PLACE DECIMAL ±	DRAWN	DB	21/06/07
	CHECKED		
	ENG APPR.		
	MFG APPR.		
	Q.A.		
INTERPRET GEOMETRIC TOLERANCING PER:			
MATERIAL: Acrylic			
FINISH: See Drawing			
DO NOT SCALE DRAWING			

Number of Duplicates: **2**

TITLE: **Runner 2**

SIZE	DWG. NO.	REV
A	18	1

SCALE: 1:5 | SHEET 18 OF 19

5 4 3 2 1

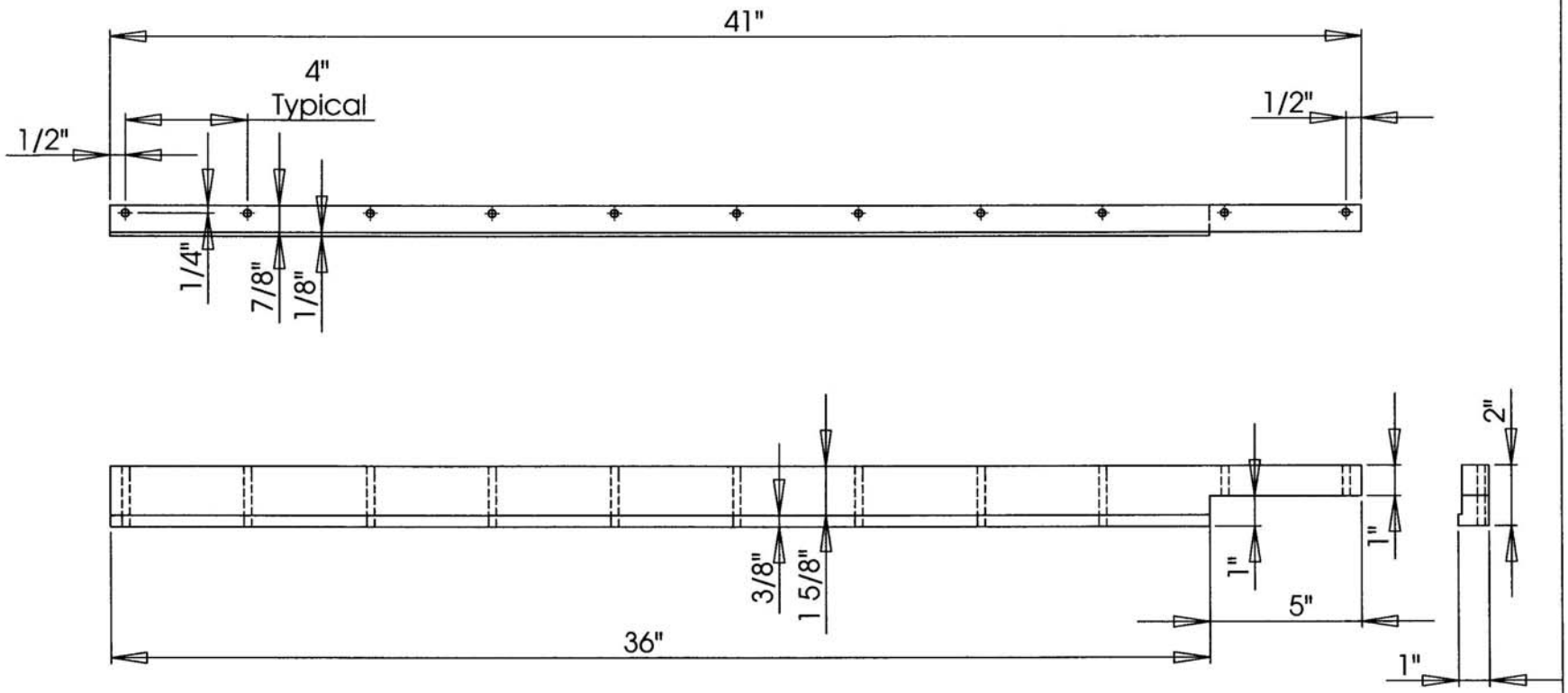

UNLESS OTHERWISE SPECIFIED:		NAME	DATE
DIMENSIONS ARE IN INCHES TOLERANCES: FRACTIONAL ±1/32" ANGULAR: MACH ± BEND ± TWO PLACE DECIMAL ± THREE PLACE DECIMAL ±	DRAWN	DB	21/06/07
	CHECKED		
	ENG APPR.		
	MFG APPR.		
INTERPRET GEOMETRIC TOLERANCING PER:	Q.A.		
MATERIAL: Acrylic	Number of Duplicates: **2**		
FINISH: See Drawing			
DO NOT SCALE DRAWING			

TITLE: **Runner 2-1**

SIZE	DWG. NO.	REV
A	19	1

SCALE: 1:5 | SHEET 19 OF 19

5 4 3 2 1